ZfP
Lehrstuhl für
Zerstörungsfreie Prüfung

Technische Universität München

Optimization of a Reverse Engineering and Part Scanning Workflow by Means of Computed Tomography

Fabian Bauer, B.Sc.

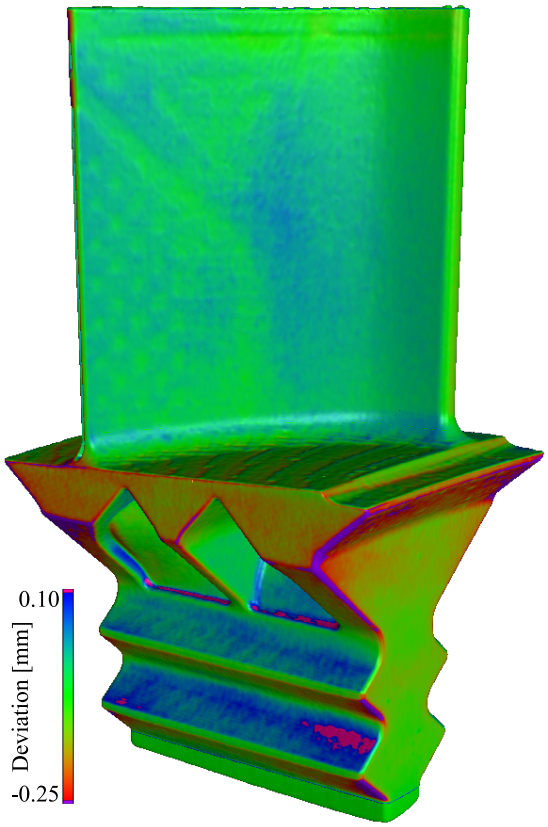

Masterarbeit

Fakultät für Maschinenwesen

Studiengang: Medizintechnik

16.10.2017

Betreuer:	Dr. rer. nat. Michael Schrapp
Betreuer:	Dipl.-Ing. Philipp Jatzlau
Prüfer:	Prof. Dr.-Ing. habil. Christian Große

SIEMENS

TECHNISCHE UNIVERSITÄT MÜNCHEN – Lehrstuhl für Zerstörungsfreie Prüfung

Prof. Dr.-Ing. habil. Christian Große

Baumbachstr. 7 · 81245 München · Tel.+49-89-289-27221 · www.zfp.tum.de

ZfP
Lehrstuhl für
Zerstörungsfreie Prüfung

SIEMENS

Technische Universität München
Lehrstuhl für Zerstörungsfreie Prüfung
Baumbachstr. 7
81245 München
Prof. Dr.-Ing. habil. Christian Große

Siemens AG – Corporate Technology
Otto-Hahn-Ring 6
81739 München, Deutschland
Ansprechpartner: Dr. Michael Schrapp
Telefon: +49 (0) 172 6676579
E-Mail: michael.schrapp@siemens.com

1. Juni 2017

Vertiefung Fakultät MW

Aufgabenstellung der Masterarbeit

Titel: Optimization of a reverse engineering and part scanning workflow by means of computed tomography.

Betreuer: Dr. Michael Schrapp (Siemens)
Tel.: 089-636-634285
michael.schrapp@siemens.com

Dipl.-Ing. Philipp Jatzlau (TUM)
089-289-27226
philipp.jatzlau@tum.de

Ausgangssituation und Motivation:

Die industrielle Röntgen Computertomographie (CT) stellt ein häufig verwendetes und sehr vielfältiges Hilfsmittel für die Zerstörungsfreie Prüfung dar. Die CT bietet dabei die einzigartige Möglichkeit, ein vollständiges 3D Volumen eines vorhandenen Bauteils zu liefern. Dieses Volumen kann durch geeignete Methoden in ein entsprechendes CAD Modell umgewandelt werden und mithilfe der additiven Fertigungstechnik (3D-Druck) können damit schnell Nachbildungen bzw. Replikate des ursprünglich vorhandenen Bauteils hergestellt werden.

Dieses Reverse Engineering Verfahren liefert jedoch nur bei sehr gutmütigen Bauteilen (hinsichtlich Durchstrahlbarkeit, Streuung, Materialen, Genauigkeit etc.) hinreichend gute Ergebnisse. Bei funktionskritischen Bauteilen wie z.B. Turbinenschaufeln spielen hohe Genauigkeitsanforderungen eine entscheidende Rolle und auftretende Messunsicherheiten in jedem der verschiedenen Reverse Engineering Teilschritte (Aufnahme, Übertragung in ein CAD Modell, Druck) wurden bisher nur unzureichend und nicht zusammenhängend analysiert.

Aufgabenstellung & Zielsetzung:

Im Rahmen dieser Masterarbeit soll der Gesamte Workflow des Reverse Engineering exemplarisch an ausgewählten Objekten demonstriert werden. Schwerpunktmäßig soll dabei die Optimierung der CT Aufnahmeparameter (Spannung, Detektor, etc.) sowie der Auswertealgorithmen (Rekonstruktion, Oberflächenfindung, etc.) durchgeführt werden.

Eine detaillierte Analyse der Messabweichungen bzw. Messgenauigkeit zwischen Soll- (aufgenommenes und repliziertes Bauteil) und Istwert (urspr. Bauteil bzw. CAD Modell) ist zudem ein zentraler Bestandteil dieser Masterarbeit.

Schwerpunkte der Masterarbeit:

- Einarbeitung in die Thematik, Literaturrecherche.
- Einarbeitung in die Computertomographie.

- Erstellung eines Messplans unter Berücksichtigung aller organisatorischen Aspekte.
  - Einarbeitung in die Messgeräte und Aufbau der Messeinrichtung.
  - CT Messungen an ausgewählten Proben.
- Bildgebung und Auswertung der Daten.
  - Weiterentwicklung bestehender Auswertealgorithmen
  - Fehlerrechnung, Analyse, Vergleich und Interpretation der Ergebnisse.
  - Bewertung der Daten im Hinblick auf Messgenauigkeit, etc.
- Anfertigung der schriftlichen Ausarbeitung in Englisch unter Berücksichtigung des Layouts des Lehrstuhls.
- Vorstellung der Ergebnisse und Abgabe aller Schriftstücke und Daten in elektronischer Form.

Voraussetzung:

- Selbstständige und strukturierte Arbeitsweise.
- Motivation und Begeisterung für wissenschaftliches Arbeiten.
- Grundkenntnisse im Bereich der Computertomographie und bei CAD Programmen.
- Programmierkenntnisse (MATLAB) sind wünschenswert.

Die Durchführung der Masterarbeit erfolgt in Kooperation mit einem Industriepartner, was eine Präsenz u.a. am Firmensitz der Siemens AG in München erfordert.

Die Bewertungskriterien für die Masterarbeit liegen vor und sind dem Masteranden bekannt. Die Vorstellung der Ergebnisse erfolgt in einem etwa 30-minütigen Vortrag am Lehrstuhl, an den sich die Notenfindung anschließt. Zu diesem Zeitpunkt liegt die korrigierte Endversion der Masterarbeit den Prüfern vor.

Beginn der Masterarbeit:	01.06.2017
Voraussichtliche Dauer:	6 Monate

Datum, Unterschrift des betreuenden Professors:

Datum, Unterschrift des Betreuers:

Datum, Unterschrift des Studenten:

Selbstständigkeitserklärung

Fabian Bauer
[redacted]
[redacted]

Matrikelnummer: [redacted]

Hiermit erkläre ich, die vorliegende Masterarbeit selbstständig verfasst zu haben. Es wurden keine anderen als die in der Arbeit angegebenen Quellen und Hilfsmittel benutzt. Die wörtlichen oder sinngemäß übernommenen Zitate habe ich als solche kenntlich gemacht.

Die vorliegende Masterarbeit entstand unter wissenschaftlicher und inhaltlicher Anleitung durch meinen Betreuer. Zentrale Ideen und Konzepte wurden gemeinschaftlich mit ihm erarbeitet.

München, den 16.10.2017

Fabian Bauer

Danksagung

An dieser Stelle möchte ich allen danken, die zum Gelingen vorliegender Arbeit durch ihre Hilfe, Motivation und vielfältigen fachlichen Rat beigetragen haben.

Zuerst und ganz besonders gilt dieser Dank meinem Betreuer Herrn Dr. Michael Schrapp (*Siemens AG*) für sein außerordentliches Engagement und die zahlreichen hilfreichen Diskussionen. Er ermöglichte es mir die Fragestellungen so frei und selbstständig wie nur möglich zu bearbeiten und war jederzeit selbst unter erschwerten Umständen für Rückfragen erreichbar.

Weiter gilt mein Dank allen Mitarbeitern, Kollegen, Studenten und Doktoranden der Gruppe für die vielseitige Unterstützung und die angenehme Arbeitsatmosphäre. Besonderen Dank verdient hier Herr Christian Watzl für seine unermüdliche Unterstützung bei allen Fragen und Problemen welche die CT-Anlage und damit verbundene Schwierigkeiten betreffen. Ohne ihn wäre ein stabiles Vakuum kaum denkbar gewesen. Ebenso danken möchte ich Herrn Dr. Matthias Goldammer und Herrn Dr. Karsten Schörner für die Betreuung der Arbeit in den ersten Monaten, die mir einen zügigen und direkten Einstieg in das Thema ermöglichten. Auch dannach standen sie häufig bei zahlreichen Fragestellungen mit fachlichem Rat und Expertise zur Verfügung. Ebenso vielen Dank an Herrn Jan-Carl Grager (*TU München, Siemens AG*) für organisatorische Unterstützung sowie Hilfe bei der formalen Gestaltung der Arbeit.

Vielen Dank auch an meine Leidensgenossen Herrn Marek Listl und Herrn Jakob Gamper für unzählige fachliche und anderweitige Diskussionen, Kaffeepausen und Anregungen. Ohne sie wäre die Arbeit sicher deutlich weniger entspannt und motivierend verlaufen.

Vielen Dank auch an Herrn Dr. Kiener (*Siemens AG*) für die Bereitstellung der Exponate. Weiter danke ich Herrn Philipp Jatzlau (*TU München*) für die Übernahme der Betreuung und Organisation. Zuletzt möchte ich auch Herrn Prof. Dr.-Ing. habil. Dipl.-Geophys. Christian Große für die lehrstuhlseitige Unterstützung recht herzlich danken.

Abstract

Reverse Engineering – the systematic approach of analyzing a workpiece with the primary intention of deriving its relevant geometric features – provides new prospects to recover or replace valuable broken components. Related methods could pose a prospective remedy for lost or inaccessible schemes for turbine blade replacement parts, which can turn overhauls into arduous and time-consuming issues, since previous studies have already shown the feasibility in principle [Bagci 2009].

Within the last decade, the application of X-ray Computed Tomography (CT) as a metrologic instrument has increasingly gained attention, with its global market being predicted to reach almost 600 million US-dollars in 2017 [De Chiffre et al. 2014]. At present, no other imaging technology is able to provide complete insight into non-superficial structures for measurement without destroying the object of investigation, which renders industrial CT an ideal choice for the Reverse Engineering and metrology of workpieces, if only limited *a priori* information is available. Unfortunately, application scenarios are restricted to such parts that offer suitable properties by means of X-ray penetrability, geometry and demands for precision.

Simultaneously, metal-processing Additive Manufacturing methods have achieved a stage of development that permits their productive use for the fabrication of load-bearing and functional components. Nevertheless, critical machine parts require meticulous control of production tolerances, so that accurate blueprints and exhaustive quality controls are obligatory.

Combining these two counterparts, the scope of this thesis aims to provide a Reverse Engineering framework that is capable of accurately determining the geometry of a given workpiece by utilizing CT as well as optical scans and manufacturing a functional replica thereof by use of Selective Laser Melting or alternative Additive Manufacturing technologies. For this purpose, two methods to overcome restrictions and drawbacks of conventional CT are suggested, which are related to resolution and X-ray penetrability; these comprise a multi-energy-CT method as well as a destructive approach to diminishing the photon path length in the object. The entire replication workflow is also examined, with a focus on emerging production aberrations, measurement errors, and their interplay for a turbine blade with highly complex internal and external structures as well as further test pieces. Depending on the considered region of the blade, a replication accuracy between $18\,\mu m \pm 87\,\mu m$ and $95\,\mu m \pm 54\,\mu m$ was achievable.

Keywords: Turbine Blade, Reverse Engineering, Additive Manufacturing, Metrology, Computed Tomography, Radiography, Non-destructive Testing.

Schlagwörter: Turbinenschaufel, Reverse Engineeering, Additive Fertigungsverfahren, Metrologie, Computertomographie, Radiographie, Zerstörungsfreie Prüfung.

Kurzfassung

Reverse Engineering – das systematische Vorgehen zur Analyse eines Bauteiles mit der Absicht die wichtigsten geometrischen Merkmale zu identifizieren und zu extrahieren – stellt neue Möglichkeiten bei der Wiederherstellung und Reparatur von hochpreisigen Maschinenkomponenten in Aussicht. Beispielsweise können geeignete Verfahren es ermöglichen, verlorene oder unzugängliche Modelle für Ersatzteile von Turbinenschaufeln zu erstellen, welche bislang bei Instandsetzungsarbeiten häufig nicht verfügbar sind, was die Wartung maßgeblich erschwert. Hierfür wurde die prinzipielle Machbarkeit bereits durch Studien nachgewiesen [Bagci 2009].
Im letzten Jahrzehnt hat die Verwendung von Computertomographie (CT) als Werkzeug für die Vermessungstechnik zunehmend an Bedeutung gewonnen, wobei der Weltmarkt 2017 voraussichtlich einen Umfang von etwa 600 Millionen US-Dollar erreichen wird [De Chiffre et al. 2014]. Zum gegenwärtigen Zeitpunkt steht kein anderes bildgebendes Verfahren zur Verfügung, welches in der Lage ist die Innenstruktur eines Objektes vollständig und zerstörungsfrei abzubilden. Daher bietet sich die industrielle CT als ideale Methode für das Reverse Engineering und die dimensionelle Vermessung von Bauteilen an, für die nur geringes Vorwissen vorliegt. Nachteilig ist hingegen, dass entsprechende Verfahren lediglich sehr beschränkt hinsichtlich der Durchstrahlbarkeit und Geometrie der Bauteile und den Anforderungen an die Genauigkeit anwendbar sind. Etwa zeitgleich haben generative Fertigungsverfahren einen Entwicklungsstand erreicht, der ihren Produktiveinsatz bei der Erzeugung von Metallbauteilen in lasttragenden und funktionserfüllenden Komponenten zulässt. Nichtsdestotrotz sind kritische Bauteile auf eine akribische Überprüfung der Fertigungstoleranzen angewiesen, sodass detaillierte Blaupausen und flächendeckende Qualitätskontrollen zwingend erforderlich sind.
Die vorliegende Masterthesis zielt darauf ab, diese beiden Prozesse zu kombinieren und hierdurch ein Framework zu schaffen, welches es ermöglicht die Geometrie eines Werkstücks durch den Einsatz von CT und optischen Scans präzise zu erfassen und mittels Selektivem Laserstrahlschmelzen oder anderen generativen Fertigungsverfahren ein funktionsfähiges Duplikat zu fertigen. Um dieses Ziel zu erreichen, werden zwei verschiedene Methoden empfohlen, die in der Lage sind bisher bestehende Einschränkungen und Schwächen der konventionellen CT in Bezug auf Auflösung und Durchstrahlbarkeit zu reduzieren. Diese basieren auf der Multi-Energie-Computertomographie sowie einem zerstörenden Ansatz zur Reduktion der Durchstrahlungsweglänge im Bauteil. Ebenso untersucht wird der vollständige Arbeitsablauf zur Erstellung der Replik eines komplexen Turbinenschaufelblatts sowie weiteren Testbauteilen. Besonderes Augenmerk liegt hierbei auf entstehenden Produktionsabweichungen, Messungenauigkeiten sowie deren Wechselwirkungen. Abhängig vom betrachteten Bauteilabschnitt ist es gegenwärtig möglich eine Fertigungsgenauigkeit für die Replik zwischen $18\,\mu m \pm 87\,\mu m$ und $95\,\mu m \pm 54\,\mu m$ im Vergleich zum Originalbauteil zu erreichen.

Table Of Contents

1. Introduction **1**

2. Fundamentals **4**

2.1. Turbines and Turbine Blades 4

2.2. Basic Principles of Computed Tomography 7

2.2.1. Applications of Ionizing Radiation 8

2.2.2. X-ray Generation 9

2.2.3. X-ray Spectrum 11

2.2.4. Interaction of X-rays with Matter 13

2.2.5. X-ray Detection 16

2.2.6. Image Reconstruction 17

2.2.7. Artifacts in Computed Tomography 20

2.3. Reverse Engineering 23

2.3.1. Contact and Optical Based Data Acquisition 24

2.3.2. Surface Determination and Meshing of CT Data 26

2.3.3. Errors in Reverse Engineering 28

2.4. Additive Manufacturing Methods for Metals 31

3. Preliminary Work **34**

3.1. Medicine 34

3.2. Commercial 3D-Printers 36

4. Retrieval of Imaging Data **38**

4.1. Turbine Blades for Investigation 38

4.2. Set-Up for Low Energy Computed Tomography 39

4.3. High and Medium Energy Computed Tomographies 41

4.4. Optical Scan 42

5. Initial Comparison of Imaging Methods **43**

5.1. Definition of Regions of Interest 43

5.2. Generation of Scan Meshes 45

5.3. Determination of Ground Truth 45

5.4. Suitability Comparison of Computed Tomography Scans 48

5.5. Assessment of Inner Feature Imaging Accuracy 52

5.5.1. Comparison to CAD Geometry 53

5.5.2. Error Estimation 54

5.5.3. Comparison of Features 55
5.6. Loss of Accuracy due to Meshing 57

6. Assessment of Production Accuracy **60**

7. Approach Based on Dual Energy Computed Tomography **66**
7.1. Previous Approaches 66
7.2. Methods and Results of Dual Energy Scan 67
7.3. Robustness of Algorithm 71

8. Destructive Testing **73**

9. Entire Replication Workflow for the Considered Turbine Blade **77**
9.1. General Procedure for Reverse Engineering and Analysis 77
9.2. Error Considerations for Entire Replication Chain 78
9.3. Quantitative Analysis of the Error Chain for the Turbine Blade 79

10. Additional Test Cases and Examples **88**
10.1. Test Pieces and Reverse Engineering Process 88
10.2. Example 1: Flow Swirler 90
10.3. Example 2: Burner Tip 93

11. Discussion **96**
11.1. Summary of Work 96
11.2. Future Prospects 97

Bibliography **103**

List of Figures **117**

List of Tables **121**

List of Symbols **123**

List of Acronyms **125**

Appendix A. Data Preparation and Correction **128**
A.1. Correction for Systematic Errors of the Foil Section 128
A.2. Correction for Support Structure and Filling in FDM Test Pieces 130

Appendix B. Material Information for EOS NickelAlloy HX **133**
B.1. Material Attenuation Coefficients for EOS NickelAlloy HX 133

B.2. Material Data Sheet for EOS NickelAlloy HX 134

Appendix C. Calibration Protocol for Optic Scanner ATOS III Triple Scan 139

Appendix D. VGStudio Workflows and Macros 144

D.1. Segmentation and Mesh Generation from Raw Data 144

D.2. Segmentation and Mesh Generation via Dual Energy Approach 144

1. Introduction

Mankind has exploited the forces of nature since centuries. Long before solar panels or the nuclear fission was feasible, windmills and mechanical constructs have been developed to alleviate heavy labor and improve productivity with limited manpower. While the first uses of plain water wheels can be traced back to 150 B.C., further modifications have been made in the successive epochs; mostly they are geared to optimize the fitness for work and to maximize the output [Usher 1929, p. 121]. Nowadays these devices are obsolete, since we can rely on more efficient prime movers to set a shaft into motion. Nonetheless, modern turbines still rely on the basic principle of a moving fluid that is vigorously pressed through its maw, but while their early precursors are mostly based on water, more sophisticated installations are able to work with other fuels, like gas or steam.

As such, a modern representative is the gas turbine, which was first proposed in 1791 by John Barber but turned into a practical device only in 1905 [Giampaolo 2006, p. 1f]. This particular configuration features a slew of principle advantages. First of all, the device is capable of producing a great amount of power with relatively compact measurements and weight. For operation, no additional cooling system is usually necessary since the inflow of air as coolant is sufficient to maintain acceptable temperatures. Due to the use of only rotational parts, the maintenance costs are relatively low compared to, for instance, large combustion engines. Also, a multitude of different fuels can be used and full-load operation conditions can be reached within minutes after start [Langston and Opdyke 1997]. These advantages have attracted great interest and led to further developments of the technology. Driven by metallurgical improvements as well as advances in aerodynamic and thermodynamic understanding and the application of more powerful computers, more efficient and capable devices have been constructed. While the first gas turbine was able to deliver 900 kW, modern systems can provide more than 450 MW and reach simple cycle efficiencies of around 50 %, compared to only 18 % in 1939 [Langston and Opdyke 1997; Siemens AG 2017]. To accomplish such remarkable performances, pressure ratios and temperatures had to surpass familiar working conditions, resulting nowadays in over 40:1 (compared to only 2.5:1 in 1900) and 1500 °C [Gameros et al. 2015; Giampaolo 2006, p. 7]. Only the most durable construction materials are able to withstand the environment within a turbine in use; therefore highly complex cooling mechanisms have been developed as well as new high tech materials, culminating in the availability of turbine blades manufactured from single-crystal superalloys nowadays [Giamei 2013].

In order to construct even more capable systems, generative production processes – commonly known as 3D-printing – have drawn attention in recent years. *Boeing Corp.* already manufactures annually more than 20,000 pieces of 300 part types in 10 commercially available aircrafts that have been produced through manufacturing technology. Printed engine nozzles of *CFM*

International have been reported to be 20 % lighter and more durable than those produced via conventional processes [Magerramova et al. 2016]. Also, the *Siemens AG* started to repair and upgrade burner components via Additive Manufacturing and reports up to 90 % reduced processing times [Overton 2014]. By now, also Nickel-based superalloys can be processed while still retaining sufficient mechanical properties, rendering novel turbine blade designs feasible [Kanagarajah et al. 2013; Magerramova et al. 2016].

All these measurements have turned turbine blades into very expensive components that need to be preserved whenever possible. For instance in 2005, the costs for maintaining turbines in a typical gas and steam power plant of 400 MW output were almost six million Euros [Panos 2007, p. 237]. Unfortunately, especially for older devices, spare parts can be hard to provide and often even blueprints or type designations are unknown. For the first part of this issue, advanced Additive Manufacturing can be a remedy. Nevertheless, unknown or lost design templates still pose an obstacle that needs to be removed in order to shorten overhaul and downtimes.

In the last decade, the imaging method of Computed Tomography has gained attraction in the field of industrial metrology. This technique does not only have the potential to position itself alongside established methods like tactile or optical scanners, but also allows to assess regions of a workpiece that have not been accessible so far. CT is expected to hold great potential for quality control and might even be able to replace common measurement tools in the future [Kruth et al. 2011].

This thesis aims to provide and optimize a replication workflow with a special focus on small turbine blades. We will reverse-engineer an already existing blade using different methods and reproducing a duplicate thereof that is as accurate as possible and that could serve as a spare part for productive use. For this purpose, we will investigate each part in the workflow and assess production accuracy as well as the limitations and benefits of different Reverse Engineering methodologies with a focus on CT.

The content of this thesis is depicted in fig. 1.1. We aim to deal with these aspects:

- We will start with a summary of the fundamentals in sec. 2 and provide essential physical knowledge as well as a short insight into methods and processes involved in our framework.
- Section 3 presents already existing solutions and preliminary works in industry and medicine that reflect the whole replication task. We will also briefly discuss to what extend they can be transferred to our problem.
- In section 4 we introduce different methods of image acquisition that are available to capture the geometry of our turbine blade.
- We assess the suitability of these and investigate advantages and drawbacks for each method in detail in section 5.

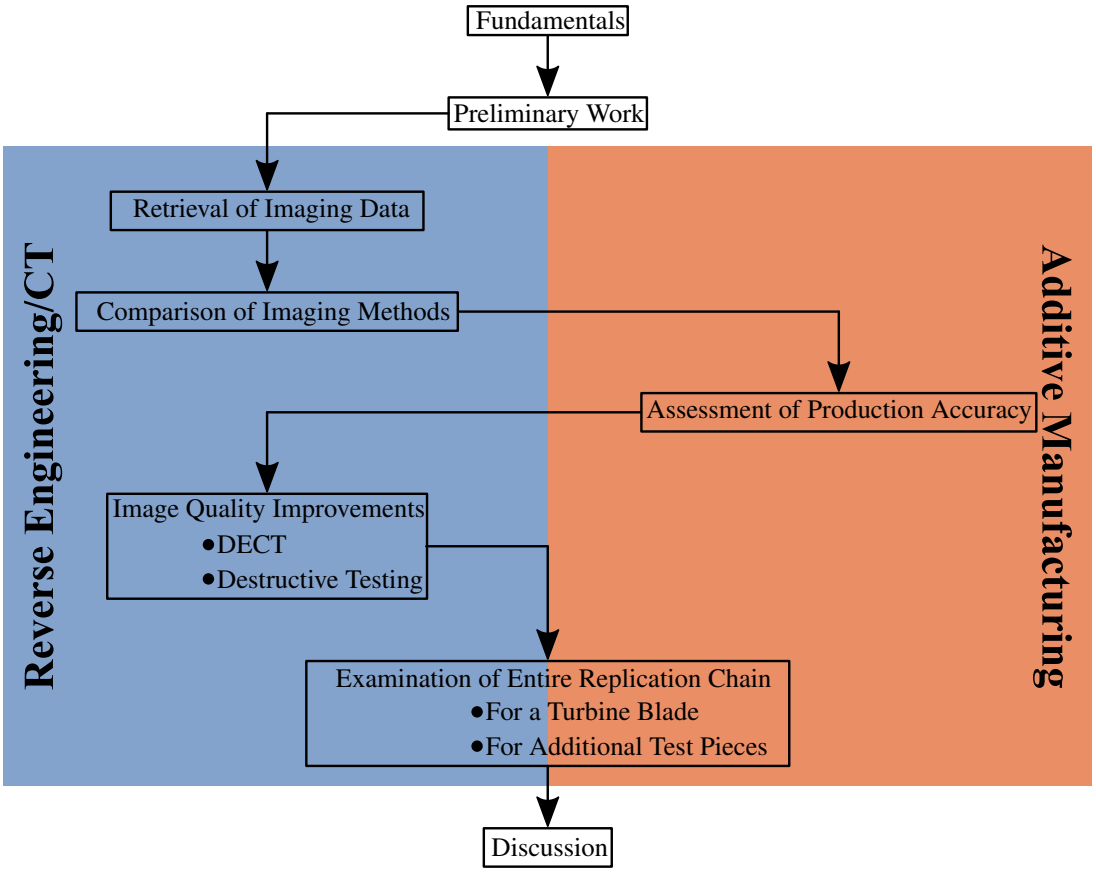

Figure 1.1.: Schematic structure of the entire Master's Thesis.

- In section 6, we take a closer look at original blade and estimate the accuracy of manufacturing and areas at the part that have proven problematic for fabrication.
- To overcome disadvantages and weaknesses of our Reverse Engineering methods, we provide two different approaches to improve the quality of the RE-model in sec. 7 and 8.
- In section 9 we finally consider the whole replication workflow as such. We combine previous results and assess potential weaknesses and aspects that are well-suited for further optimization. We also express the accuracy and fidelity of the process quantitatively.
- To show that our framework is not only suitable for turbine blade parts but can also serve for other applications, we provide two additional test pieces in sec. 10 and analyze them analogously to sec. 9.
- Finally we discuss our findings and propose aspects that need to be investigated for further improvements in the future in sec. 11.

2. Fundamentals

In this chapter we provide the basic principles that this thesis is based on. First we will give a very short introduction into turbines, turbine blades and typical damages in sec. 2.1. Next, we will provide an overview over Computed Tomography (CT) (sec. 2.2), comprising the applications (sec. 2.2.1) and basic physics (sec. 2.2.2 to 2.2.4) and other related steps such as image reconstruction (sec. 2.2.6) or emerging artifacts (sec. 2.2.7). We will also deal with the application of CT in metrology and Non-destructive Testing (NDT) in sec 2.2.1. Next, in sec. 2.3, we will explain what Reverse Engineering (RE) is about and what steps need to be performed for it. We will end with a short overview of possible Additive Manufacturing (AM) technologies that are able to process and manufacture steel and related alloys in section 2.4.

2.1. Turbines and Turbine Blades

Turbines are generally defined as a device that is able to convert the energy inherent to a fluid stream into mechanical energy [Encyclopædia Britannica 2017]. The typical buildup for a gas turbine is depicted in fig. 2.1. First, atmospheric air is sucked into the compressor. This part is usually made up of several stages, each consisting of a row of rotating airfoils and a row of stationary blades, the so called stators. These are arranged in such a way that the air gets compacted before it enters the combustion chamber. This section consists of a casing, a flame tube and a fuel injection system and has the purpose to ensure a stable, continuous and efficient combustion at all possible operating conditions without any pulsations or suchlike. The hot gases are subsequently expanded in the final stage – the actual turbine – where the thermal energy is converted into mechanical work. The turbine is linked with the compressor via a shaft, so the rotation is directly used to compress the incoming air flow. The remaining useful work is available as shaft power, e.g. to drive a generator in order to produce electric energy. This cycle is often referred to as the Brayton Cycle [Langston and Opdyke 1997].

Probably for the majority of people the most familiar application of turbines is their use as jet engines for airplanes. For this purpose, the energy produced by combustion is transferred to the shaft in order to generate thrust and propel the aircraft. The gas turbines we will deal with in this thesis are common land-based systems used for power generation, e.g. in power plants. Other uses comprise compressors for gas pipelines or as compact but powerful engine for vehicles. For instance, devices are used in ships, helicopters or tanks [Giampaolo 2006, p. 20f].

During operation, turbines encounter a remarkably hostile environment. Foils are exposed to high mechanical stresses due to centrifugal force (the rotation can exceed 10,000 rpm) as well as vibratory and flexural load. Usually a turbine does also not operate at the same speed, but is subject to changing loads (start-ups, slowing downs, trips, overhauls, etc.). The air and fuel flow are polluted to some degree with contaminations or solid particles. High temperature gradients as well as generally the temperatures reached pose to be subject of additional stress to

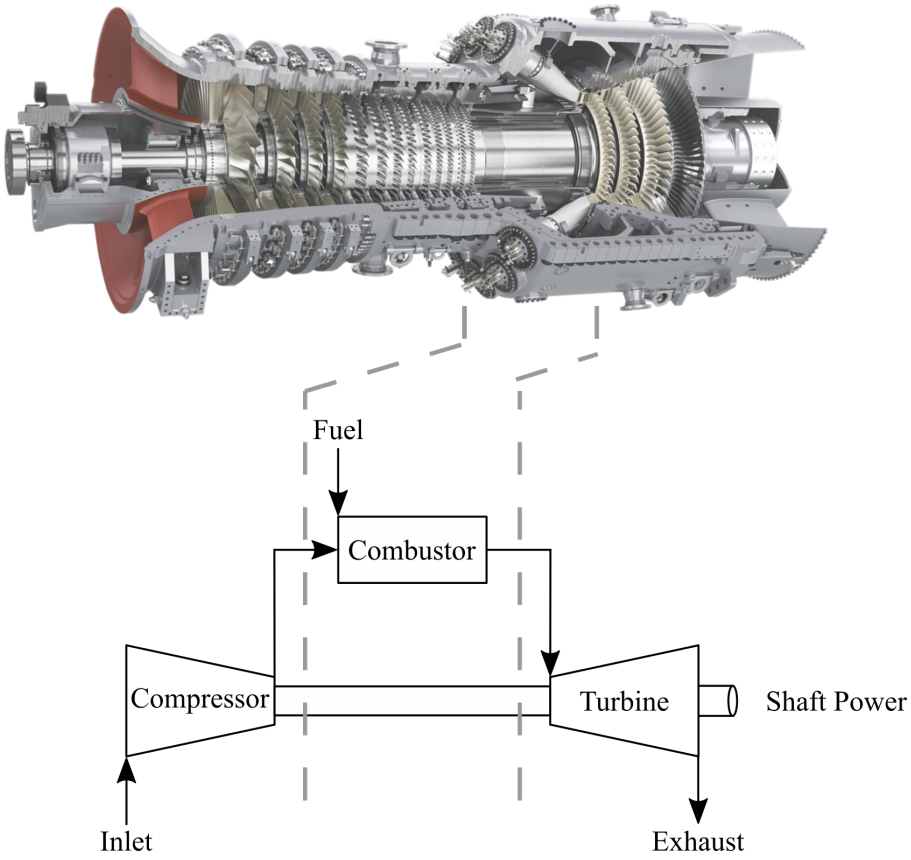

Figure 2.1.: Typical buildup of a gas turbine and its stages (Siemens SGT5-8000H heavy duty gas turbine [Langston and Opdyke 1997; Siemens AG 2017]).

the material [Gameros et al. 2015; Mazur et al. 2005; Savio et al. 2007]. These factors usually cause a significant reduction of lifetime to the blade, provoked usually by followed damage mechanisms [Mazur et al. 2005]:

- thermal and thermomechanical fatigue
- oxidation
- corrosion and fretting
- erosion
- creep
- damage by foreign objects

An investigation for a specific blade after ca. 24,000 h of service suggest that a transformation of carbides occurs due to thermal stress, resulting in a decrease of toughness and ductility down to values of only 30 % compared to its initial properties. Additionally, cracks up to 0.4 mm deep were found in the cooling system. Maximum tension stresses occurred in the middle of the cutting plane close to the cooling system due to the thermal gradient caused by it [Mazur et al. 2005]. Cooling channels feature generally a diminished resistance against surface damage, since the continuous airflow and the high temperatures favor surface oxidation and linked crack propagation. Damages often occur also at the tip of the leading edge of the blade [Dewangan et al. 2015]. For aircraft turbines, ingested foreign objects and high temperatures were found to

be the most likely sources of damage [Carter 2005]. However, since blades of power turbines can vary greatly, the underlying reasons for failure differ from foil to foil and need to be determined individually [Márquez et al. 2012]. In general, damages to the leading edge are more critical than such to the trailing edge [Giampaolo 2006].

At present, several methods exist in order to repair worn out or damaged turbine components. These techniques comprise conventional methods such as milling, brazing or welding as well as Additive Manufacturing methods [Bi and Gasser 2011; Nowotny et al. 2013]. This way, similar material properties compared to the original part (e.g. microhardness) can be achieved. It is also possible to use AM for manufacturing of engine parts or turbine blades directly, which is already possible for very complex geometries [Magerramova et al. 2016; Shitarev et al. 2014].

In order to sustain the high temperatures in operation of up to 1500 °C, turbine blades are generally provided with an internal cooling system. A continuous airflow of ca. 650 °C pressed through these veins is necessary to cool the blade to 1000 °C [Gameros et al. 2015]. Within the blade, typically used features comprise rib turbulated cooling and pin-fin cooling to increase heat exchange via convection. Internal cooling air can also be redirected to impinge on the inner side of an exterior wall of the foil to increase heat exchange; this method is named impingement cooling. In order to cool the outer surface usually a technique called film cooling is used. A certain amount of the chilled air from the internal cooling system is ejected through several small holes and provides a protective layer of air around the foil. In modern blades usually a combination of these techniques is applied [Kwak and Han 2003; Sidwell et al. 2004, p. 15].

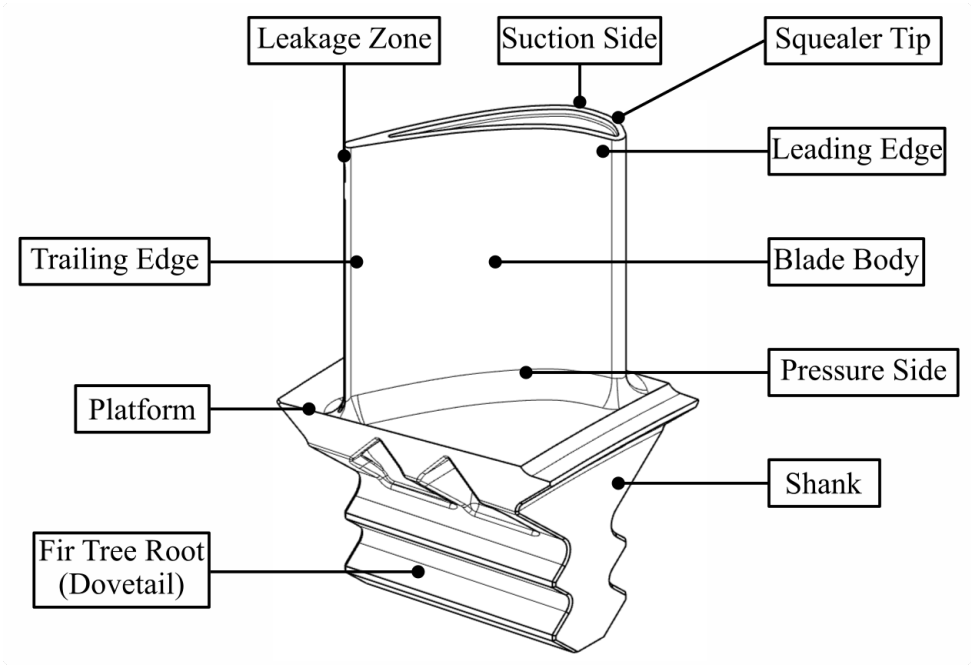

Figure 2.2.: Sketch of the used turbine blade with common nomenclature of its parts (termini taken from [Girardeau et al. 2013; Kwak and Han 2003; Yan et al. 2014]).

Fig. 2.2 shows a schematic drawing of the turbine blade we will investigate in the thesis at hand and its components. We will mostly refer to the upper part of the blade as foil and as socket to the lower part.

2.2. Basic Principles of Computed Tomography

In 1895, Wilhelm Conrad Röntgen discovered the X-rays – high energetic photon radiation that is able to pass through objects that are opaque to the human eye and reveal inner details of the penetrated entity without any need to open or destroy it. This discovery has layed the fundament for the emergence of all radiographic techniques, starting with the planar radiography that was developed some years later and transpired to be valuable in many fields [Buzug 2008, p. 15].
Nevertheless, since conventional X-ray radiography is a projection technique, its usage is accompanied by a loss of geometric information, i.e. only a two-dimensional image is obtained. Averaging over the complete object of investigation brings a diminution of depth information and a noticeable reduction in contrast with it. In order to overcome these drawbacks, the first CT-scanner was invented in 1972 by Godfrey Hounsfield. Driven by the health industry, the CT has developed greatly until today. Machines for special purposes are able to acquire an image slice in 50 ms or obtain voxel[1] sizes of less than 1 µm [Buzug 2008; Hounsfield 1973; Kalender 2006; Salamon et al. 2008, p. 75f]. Common to all is still the same basic principle: the object of investigation is exposed to X-ray radiation from different angles. For each position the radiation intensity is measured and the detector is moved to the next position. Since the radiation intensity is directly linked to the path integral of the material attenuation values (see sec. 2.2.4) it is possible to draw conclusions about the shape of the volume. By varying the distances between source, object and detector it is also feasible to accomplish a scale-up of the projected image compared to the original size of the part, so that the detector resolution appears to be M-times higher than the detector can physically offer, with M being the magnification factor. This way the resolution for image capture can be increased remarkably. The spacing between focal spot of the X-ray tube and object is called the source-object-distance (SOD) and to the detector source-detector-distance (SDD). Making use of the intercept theorem, we can determine the magnification M (and with it the voxel size as well) of a cone beam setup easily by adjusting both distances according to $M = \frac{SDD}{SOD}$. However, Wiacker (1991) notes that detail perceptibility is in fact even better – to the subvoxel level – which he traces back to accumulating geometric information via the reconstruction procedure.
The general procedure for a CT is depicted in fig. 2.3. In this chapter we will provide a short insight into each step that needs to be performed until the final volume information is available for further processing. First we give an overview over current applications (sec. 2.2.1) and the physical actions involved: sec. 2.2.2 and 2.2.3 explain the generation and properties of X-rays,

[1] A voxel is the three-dimensional pendant to a pixel.

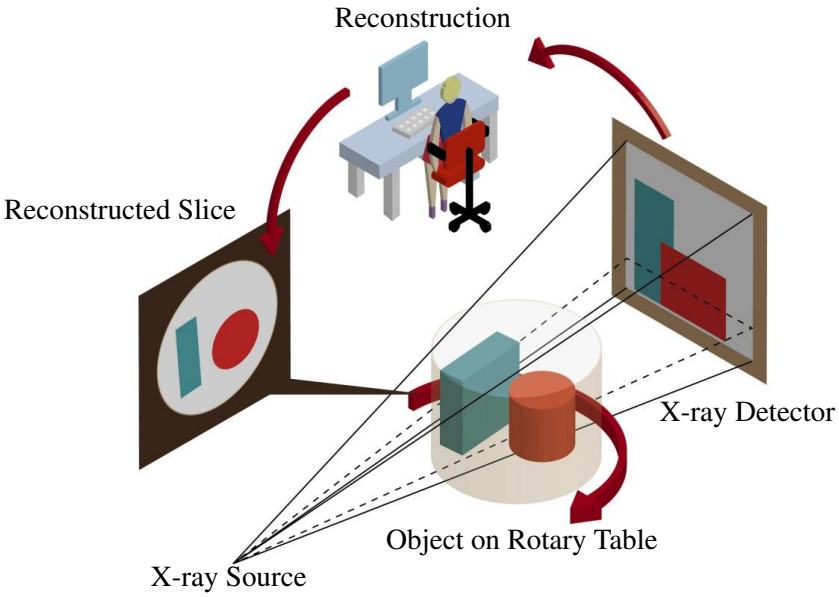

Figure 2.3.: Typical workflow of a cone beam CT (adapted from [Sun et al. 2012, p. 13]).

while in sec. 2.2.4 we will contemplate with the photon-matter-interactions in the workpiece and its detection in sec. 2.2.5. Finally we give a short insight into relevant reconstruction techniques in sec. 2.2.6 and possible artifacts in the reconstructed image in sec. 2.2.7.

2.2.1. Applications of Ionizing Radiation

In general, three different primary applications for CT systems have emerged. Traditionally, the first one is medical imaging, where the technology also originates from. Detailed contemplations with this sector and linked developments seem omnipresent in the literature, therefore we refer to Kalender (2006) for a more detailed overview of its history and achievements. Second, the CT is applied in the field of material and Non-destructive Testing (NDT). The third and last large field for CT lies the application of gauging and measuring. Radiography-based metrology is a relatively young field: the first approaches have been conducted in the early 90s but started to draw serious attention only after 2005. The greatest advance compared to other methods like optical scanning or coordinate measuring machines (CMMs) (see sec. 2.3.1) is the possibility to probe inner areas of an object of investigation as well as multi-material boundaries – a benefit that no other application is able to offer so far. This can be particularly important if an assembly needs to be probed, which can have different dimensions compared to the single pieces it is made of (e.g. plastic connectors). Also, CT is able to obtain not only geometric information, but also material specific data (density, etc.) simultaneously. Typical NDT investigations like analyzes related to porosity, material homogeneity or welding quality can be carried out without any time loss during checks for deviations of form [Kruth et al. 2011; Wiacker 1991].
A survey concerning the accuracy of CT as metrological instrument involving 27 laboratories came to the conclusion that measurements concerning length and roundness are precise with an accuracy of 6 µm to 53 µm (compared to ≤ 5.5 µm for CMMs). Significant differences between

participating institutions were found as well [Angel and De Chiffre 2014]. We want to stress that these investigations were conducted by artifact-free CTs, i.e. the objects of investigation were chosen accordingly. In the context of this thesis we will deal with artifact-affected and flawed volume data, so these tolerances apply only very limited for our usage. For a more detailed discussion we refer to section 5.4.

Metrologic and NDT CT are often summarized under the term industrial CT. Applications for this sector are manifold: typical branches are the aerospace and transport industry and the field of electronics. Emerging markets can be found in the food and security industry as well as to probe new materials (e.g. foams or composites) [De Chiffre et al. 2014]. Radiography is also used in many other industrial fields. For a more detailed contemplation, see e.g. Lowenthal and Airey (2001). The literature also holds less apparent applications like soil sciences or automated cutting lines for animal carcasses in the meat industry [De Chiffre et al. 2014; Taina et al. 2008].

2.2.2. X-ray Generation

X-rays are essentially electromagnetic waves with wavelengths of ca. 10^{-8} m to 10^{-13} m [Buzug 2008, p. 16]. The electromagnetic spectrum comprises low energy radiation like radio waves up to shorter wavelengths, e.g. ultraviolet or γ-rays. Figure 2.4 provides a rough overview of the spectrum and related ranges.

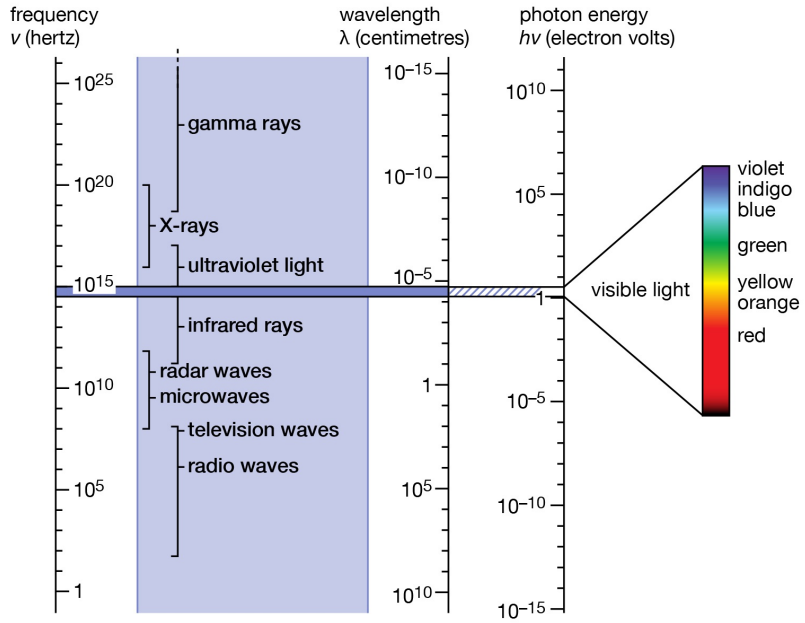

Figure 2.4.: The electromagnetic spectrum and its ranges [Encyclopædia Britannica 2017].

Usually X-rays are produced within an X-ray tube by directing a beam of fast electrons at a metallic target. The subsequent deceleration of charge carriers generates a spectrum of high energetic photons. The typical build-up of an industrial X-ray tube is shown in fig. 2.6. A cathode filament is heated up to approximately 2400 K. This temperature is sufficient to overcome the

binding energy of the filament, which is usually made of thoriated tungsten. As a consequence, the electrons are boiled off by thermionic emission and get drawn to the anode. By applying an electrical potential to a cup-shaped metal electrode – the so called Wehnelt Cylinder – the electron trajectories can be influenced in order to control the desired convergence and intensity. Subsequently the electron beam can also be shaped, i.e. by use of magnetic lenses. A uniform speed for all electrons is beneficial for this step. The beam finally hits the target, the electrons are slowed down abruptly and their energy is converted into heat and X-rays that leave the vacuum tube.

(a) Projection with Large Focus

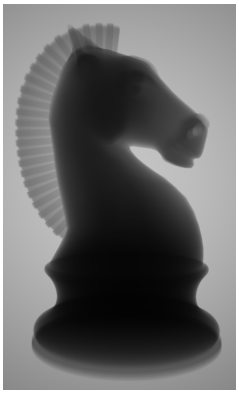

(b) Projection with Small Focus

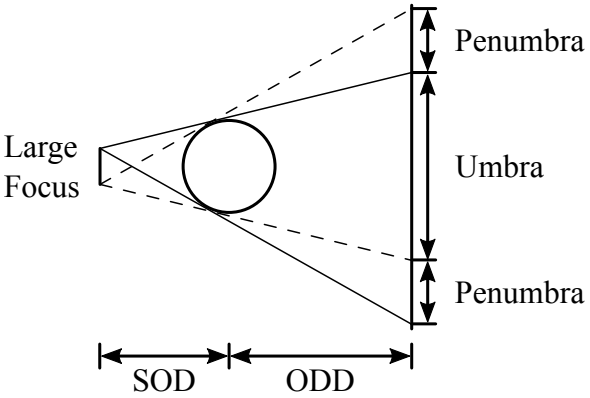

(c) Geometric Influence of Large Focus

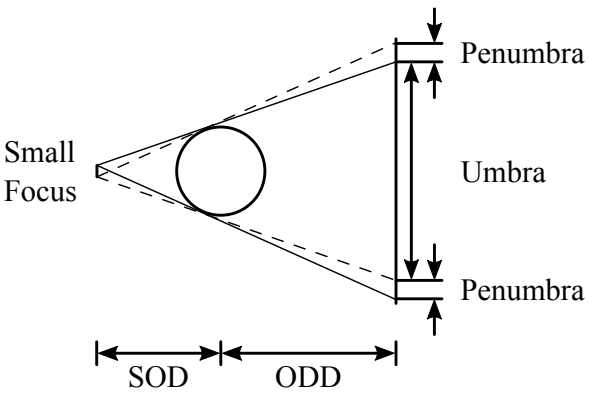

(d) Geometric Influence of Small Focus

Figure 2.5.: Geometric influence of the focal spot size by creation of disturbing penumbra and desired umbra regions (fig. 2.5c and 2.5d). Also shown are the source-object-distance (SOD) and object-detector-distance (ODD). The resulting images in a 2D-projection are shown in fig. 2.5a and 2.5b (scheme adapted from [Kueh et al. 2016], images simulated via aRTist).

Since over 99 % of the electron energy is converted into heat, the cooling of the metallic target is crucial. Its material must be able to withstand high thermal stress and possess a good conductivity for the produced thermal energy. A material often used for this purpose is tungsten. In order to obtain as sharp images as possible it is necessary to concentrate the electron beam on a very small area of the target. This spot is called the focal spot or focus and can even become smaller than a micrometer (i.e. nanofocus). With higher electron power it becomes increasingly difficult to cool the target, so that the focal spot needs to be adjusted to greater sizes of typically 30 µm to 1000 µm.

In general, tubes with a focal spot of 5 µm to 300 µm are named microfocal tubes. Contrary to that, tubes with smaller spots are referred to as nanofocal tubes, but so far no norm is available for a uniform definition [Buzug 2008; Kruth et al. 2011; Schiebold 2015; Stegemann 1995, p. 15f, p. 9, p. 87]. The influence of focal spot size is depicted in fig. 2.5. The finite size of the focus gives rise to so called penumbra regions, which lead to a diminished image quality. This is especially visible at the borders of the object; the edges become blurry and less well-defined. Since the detector features a fixed pixel size and superposition with other artifacts like the partial volume effect (see sec. 2.2.7) can occur; the phenomenon poses a significant problem and a small focus becomes crucial if an improvement of the image quality is desired. This can be accomplished by reducing the acceleration voltage, which is in direct conflict with the penetrability of the X-ray beam (see sec. 2.2.4) [Kueh et al. 2016]. Instead of reducing the focal spot size, another possibility to decrease the influence of penumbra regions is to increase the source-object-distance (SOD). Unfortunately, the necessary exposure time is linked with the squared SOD so that this tempting option is only possible to a limited extent. Also, the source-detector-distance (SDD) needs to be adjusted in order to retain a constant magnification and resolution, which is not always feasible. Likewise, this is the reason for a tendency to longer durations for an entire CT when a microfocus system is used [Hanke 2010; Schiebold 2015].
Contrary to medical X-ray tubes which rely on a massive reflective target, fig. 2.6 shows the cross section of a transmission target construction. The produced photons exit the tube in the same direction like the incident electrons. Since the target needs to be rather thin and cooling is hindered in such a design, only comparably low electron energies of few 100 keV may be used to prevent damage to the target [Kruth et al. 2011].

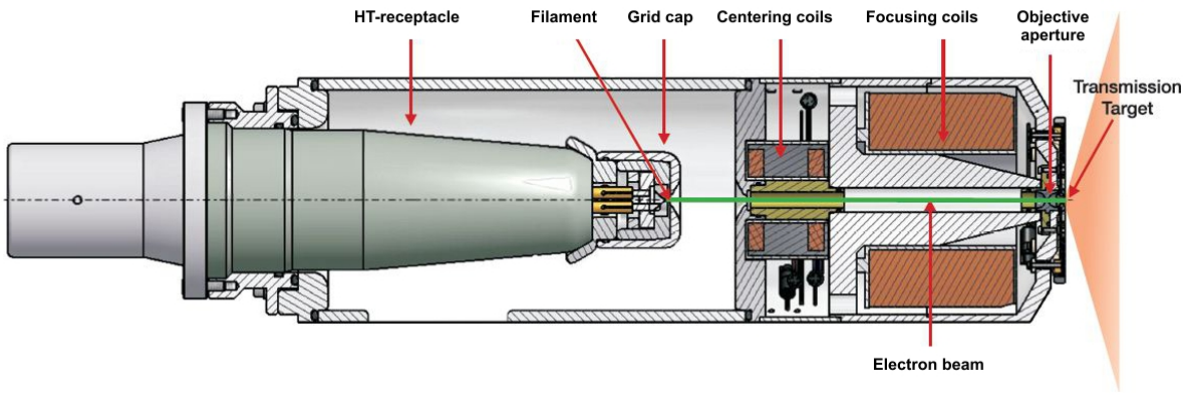

Figure 2.6.: Typical design of an X-ray tube with transmission target [X-ray WorX 2017].

2.2.3. X-ray Spectrum

The produced X-rays are not monoenergetic but follow a target material dependent distribution. In general, two effects contribute to the overall spectrum: *bremsstrahlung* and emission of a

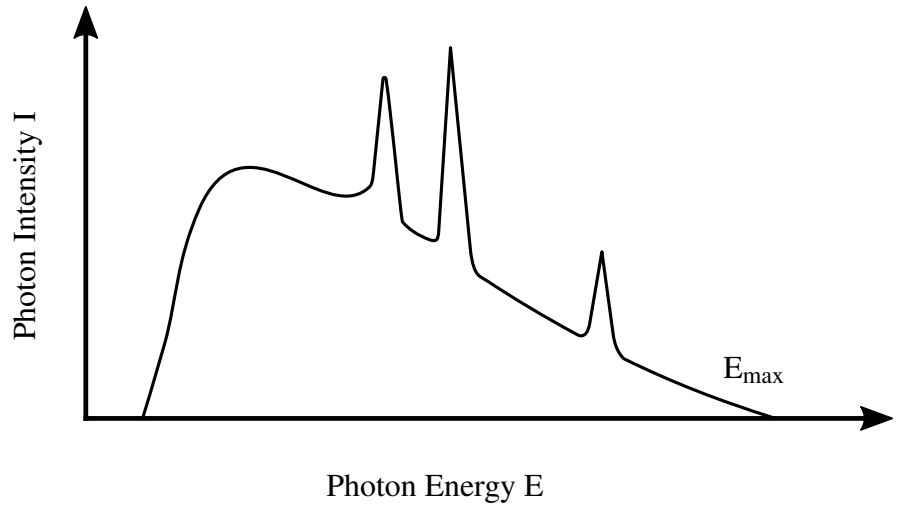

Figure 2.7.: Schematic distribution of a typical polychromatic X-ray spectrum. The discrete characteristic peaks are clearly distinguishable from the continuous *bremsstrahlung*.

characteristic line spectrum. When fast electrons hit the target they can get deflected by the electromagnetic field of charged particles in the medium. This happens essentially at atomar nuclei, but also deflection via ambient electrons is possible [Shultis and Faw 2002, p. 205]. According to classical electromagnetic theory, the (de)acceleration of charged particles is related to the emission or absorption of radiation. Since this happens usually not in a single event but a cascade of several deceleration stages instead, a continuous distribution emerges. This fraction of the radiation spectrum is known as *bremsstrahlung*. The maximum possible frequency ν_{max} of the spectrum is determined only by the applied voltage. Considering the conservation of energy we can determine it as $eU_a = h\nu_{max} = E_{max}$ with the charge of a single electron e, acceleration voltage U_a and Planck's constant h [Buzug 2008; Van Grieken and Markowicz 2001, p. 3, p. 21]. The acceleration voltage U_a is typically in the range of 25 keV to 150 keV for medical imaging and up to 500 keV for material inspection [Kramme 2011, p. 322]. However, for special applications several megaelectronvolt can be necessary, which cannot be produced anymore by conventional X-ray tubes but need more sophisticated and expensive linear accelerators instead (see also sec. 2.2.7) [Kruth et al. 2011].

Furthermore, beam electrons can interact with the inner shell of electrons of the target material and forcefully remove them from the atom. The vacancy is subsequently filled by electrons of outer, less energetic shells. The energy difference is set free by emission of photons of wavelengths that are characteristic for the respective target material. A spectrum with sharp edges arises and superimposes the *bremsstrahlung*. The resulting overall X-ray spectrum is illustrated in fig. 2.7.

2.2.4. Interaction of X-rays with Matter

In this section we will briefly present the different mechanisms that accomplish an attenuation in the intensity of the X-ray beam as it passes through the test object. Subsequently we will discuss the mathematical formulation related to this issue.

Attenuation Mechanisms

Radiographic testing methods rely on the attenuation of X-rays as they pass through the object of investigation. In general, one can distinguish between a slew of different types of photon-matter interaction that are able to alter the energy as well as the direction of photons. Here we will concentrate only at the most important ones. These are:

- **Scattering:** Two mechanisms of scattering will be important for us:
  - **Coherent Scattering:** If an X-ray photon strikes an electron several reactions are possible, depending on its energy. If the energy is comparably low (the frequency of the photon is smaller than the natural frequency of the hit electron) elastic scattering represents an important part of the attenuation. Only the direction of the incident photon is slightly altered, but no energy transfer occurs and its wavelength remains the same. Depending on the collision partner the process is also termed Thomson or Rayleigh scattering [Buzug 2008; Shultis and Faw 2002, p. 34, p. 186].
  - **Compton Scattering:** The pendant to an inelastic collision is conceivable as well. In this case the photon loses a fraction of its energy to the electron that is subsequently ejected from the atom. For the photon, the direction of propagation is altered and its wavelength is prolonged due to the loss of kinetic energy. Both collision partners can still possess enough energy to undergo additional successive reactions after the incident. The total Compton cross-section can be calculated via the Klein-Nishina equation [Buzug 2008, p. 38].
- **Photoelectric Absorption:** For photoelectric absorption, the X-ray photon interacts in such a way with the atomar electron that the photon disappears completely and the electron is ejected of the atom. This process is only possible with an entire atom and cannot be observed with free electrons. For sufficient energy of the photon, most absorbing reactions occur in the K-shell, which is the most tightly bound one (equates the inner shell). The emerging vacancy is filled subsequently with an electron from an outer shell or band electrons by emitting characteristic fluorescence photons. If this photon is energetic enough, instead of leaving the atom it can transfer its energy to another electron – the so called Auger Electron – that is emitted instead [Buzug 2008, p. 36].

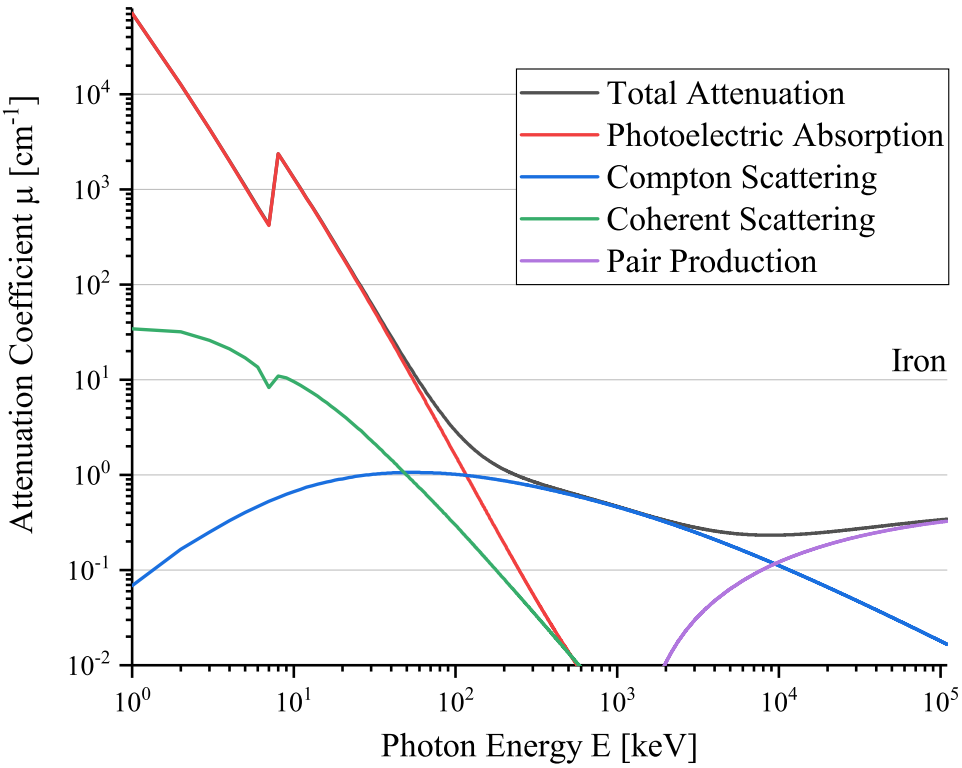

Figure 2.8.: Composition of the Linear Attenuation Coefficient for Iron. We will deal with photon energies in the range of ca. 0.1 MeV to 10 MeV, which is dominated by the Compton Scattering effect. Values were obtained via simulation by aRTist (*BAM*, Berlin, Germany).

- **Pair Production:** Very high energetic photons are able to interact with the Coulomb field of the nucleus. In this process they vanish entirely but produce a pair of an electron and its anti-particle, the positron, with both receiving approximately the same amount of energy. Usually the positron exhibits a very short lifetime, since it can recombine with another electron. Subsequently both disintegrate into two γ-rays with an angle of ca. 180° between each other. This annihilation process is utilized for medical imaging in Positron Emission Tomography (PET). Pair production interaction can only occur if the energy of the incident photon surpasses a threshold of E=1.022 MeV, which equals the combined rest energy of both produced particles. The probability of interaction raises continuously with gaining photon energy and poses the dominant mechanism for energies $h\nu > 10$ MeV. Pair production is also possible in the field of an electron, the so called triplet production [Buzug 2008, p. 39f].

Fig. 2.8 shows the relative attenuation coefficient and the contribution of different effects for energies for iron. The scope of this work comprises scans involving energies ranging from several hundred keV up to almost 7 MeV. The predominant mechanism for this range is Compton Scattering. Note also that in this range the attenuation coefficient does not change considerably. Because of that, a higher acceleration voltage as used in linear accelerators is able to probe thicker materials (or such with a higher density). Most X-ray detectors in operation obtain their

signal not by the count of incident photons, but from the deposited energy $E_p = nh\nu$ instead[2]. Here, n denotes the number of photons, h Planck's Constant and ν the frequency of a single photon. Since the photon energy is linked to the energy of an electron $E = eU_a = E_{max}$, a rise in the acceleration voltage leads to an increased signal intensity [Guni 2012, p. 7].

Lambert-Beer's Law

The fundamental formula to describe the reduction of X-ray intensity is called Lambert-Beer's Law. It holds for many attenuation processes in nature as well. Attenuation is accomplished by scattered radiation that will not hit the detector as well as absorption in the material. If we assume both effects to be linear, we can define a scatter coefficient μ_S and an absorption coefficient α. Combining both effects into a single value gives the linear attenuation coefficient $\mu = \mu_S + \alpha$, which we assume to be constant for a given photon energy [Buzug 2008, p. 32]. In general, the attenuation of intensity is mainly influenced by:

- **Photon energy:** Photons with a small wavelength λ are able to pass through a medium with less losses, according to $\alpha \propto \lambda^3$. Since conventional X-ray sources are usually not monoenergetic, this gives rise to a phenomenon called beam hardening, which can cause artifacts in the image (see sec. 2.2.7).
- **Atomic number:** A higher atomic number Z greatly influences the absorption coefficient with $\alpha \propto Z^4$.
- **Mass density:** A greater density ρ influences the attenuation with $\alpha \propto \rho$.
- **Thickness of the medium:** The loss of intensity ΔI is proportional to the penetrated pathway $\Delta\eta$, like specified in eq. 2.5.

In order to investigate the influence of the radiated path length of the medium to the obtained intensity, we consider a monoenergetic X-ray that penetrates a homogenous medium with linear attenuation coefficient μ. The intensity at the point η is given by $I(\eta)$ like shown in fig. 2.9.

$$I(\eta + \Delta\eta) = I(\eta) - \mu(\eta) I(\eta) \Delta\eta \ . \tag{2.1}$$

Reordering and solving for infinitesimal small thicknesses yields the differential quotient:

$$\frac{dI}{d\eta} = \lim_{\Delta\eta \to 0} \frac{I(\eta + \Delta\eta) - I(\eta)}{\Delta\eta} = -\mu(\eta) I(\eta) \ . \tag{2.2}$$

[2]This formula is simplified for a monoenergetic X-ray source. For a more realistic contemplation, n needs to be replaced by an integral over all photons with various frequencies.

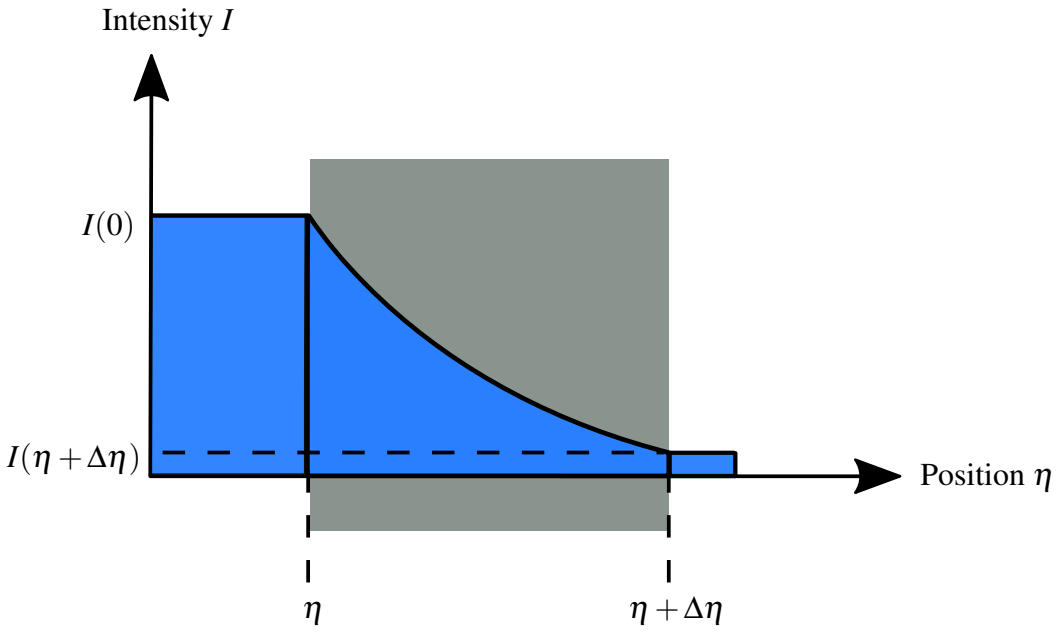

Figure 2.9.: Attenuation of X-ray intensity in a workpiece at position η.

We reorder again and integrate both sides:

$$\int \frac{dI}{I(\eta)} = -\int \mu(\eta) d\eta \; . \tag{2.3}$$

Since μ is assumed to be constant we can obtain an implicite expression for the intensity:

$$\ln(|I(\eta)|) = -\mu\eta + C \; . \tag{2.4}$$

For the undiminished intensity at the beginning we obtain the maximum intensity, i.e. $I(0) = I_0$. Thus we can set $C = 0$ in order to fulfill this condition. Furthermore, the intensity cannot be negative. Making use of the exponential function we find the special solution

$$I(\eta) = I_0 \, e^{-\mu\eta} \; . \tag{2.5}$$

This formula only holds for monoenergetic rays (see sec. 2.2.3) and a homogenous medium. Furthermore, we assume scattered radiation to vanish entirely [Buzug 2008, p. 32f].

2.2.5. X-ray Detection

A multitude of different constructions for X-ray detection exist so far. Within the framework of this thesis, we will only use an indirect conversion flat panel detector (FPD). Additional informations about other detector types can be found in the literature [Körner et al. 2007; Yaffe and Rowlands 1997]. The build-up of such is depicted in fig. 2.10. The incident X-rays strike a scintillator layer, usually made of NaI(Tl), CsI or gadolinium compounds. Due to the effect of photoluminescence, visible light (ca. 390 nm to 700 nm) is set free. The intensity of the

detected X-ray radiation is proportional to the number of generated low energy photons. The height of photon pulses is measured by a photodiode detector array underneath and read out via thin-film transistors (TFTs) or charge-coupled devices (CCDs). The obtained data allow to draw conclusions about the spatial intensity distribution of the original radiation [Chotas et al. 1999; Shultis and Faw 2002, p. 214–234].

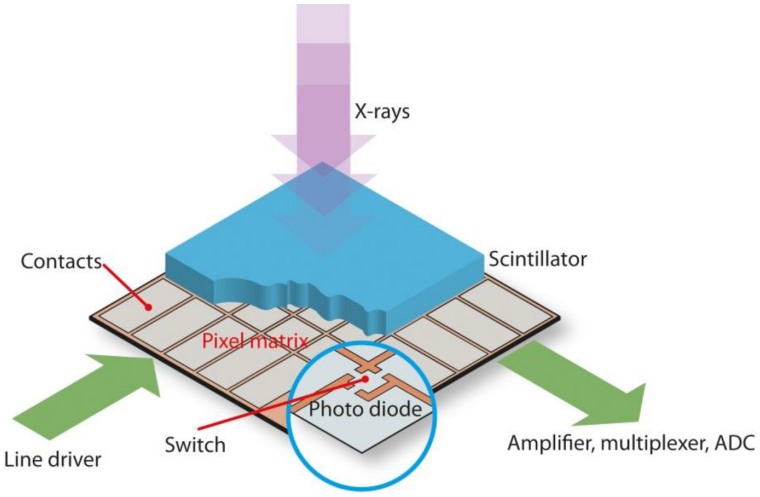

Figure 2.10.: Internal structure of a scintillation detector [Sun et al. 2012].

2.2.6. Image Reconstruction

Once the projection images are available they need to be processed by an image reconstruction algorithm in order to obtain the desired volume. From a mathematical point of view, this can be considered an ill-posed inverse problem where we take plane projections of an object and trace them back to its spatial structure; this task is accomplished by an image reconstruction algorithm. For such, many different methods are available, comprising Fourier-based, algebraic and statistical reconstruction methods. Since a detailed contemplation with these sophisticated approaches is beyond the scope of this thesis, we will only give a brief explanation of the two-dimensional Filtered Back-Projection (FBP), which is a standard method for CT image reconstruction. The FBP is widely spread and implemented in all modern CT systems [Buzug 2008, p. 175].

Since the system of radiation source and detector is moved relatively to the object, we start by introducing two Cartesian coordinate systems: (x,y) for the object-fixed system and (ξ,η) for the source-detector system. Both are linked to each other by the rotation angle γ and the equation

$$\begin{pmatrix}\xi\\ \eta\end{pmatrix} = \begin{pmatrix}\cos(\gamma) & \sin(\gamma)\\ -\sin(\gamma) & \cos(\gamma)\end{pmatrix}\begin{pmatrix}x\\ y\end{pmatrix}. \tag{2.6}$$

Note that it is irrelevant for further proceeding if the object or the detector is the moving part, since the relative position is described only by a single parameter γ. Depending on the direction of rotation and which of both parts is considered to be fixed, the rotation matrix needs to be

multiplied with the factor -1. In reality both coordinate systems only allow discrete values, since the detector features a certain pixel size and the angle γ is usually not changed continuously. Nevertheless, we will neglect this for the sake of a more graspable explanation. Due to the same reason we consider a pencil shaped X-ray collimation, a constant SDD and a maximum rotation angle of $\gamma_{max} = 180°$ so that each projection image does only exist once.

The goal of a CT is to determine the spatial distribution of the attenuation values μ of the object of interest. Since it is physically more meaningful to define these directly in the source-detector coordinate system we link them to the part by defining:

$$\mu(\xi,\eta) = f(x,y)\ . \tag{2.7}$$

We now introduce the so called Radon transformation $\mathscr{R}$. This is basically the line integral over all attenuation values that lie on a specific straight path L in the (ξ,η) space. Furthermore, we consider ideal conditions (e.g. no scattering or beam hardening) and attenuation coefficients that are independent from the incident photon's energy. Now we define:

$$\mathscr{R}(f(x,y)) := \int_L \mu(\xi,\eta)dl = \int_{-\infty}^{+\infty} \mu(\xi,\eta)d\eta \tag{2.8}$$

$$= \int_\gamma f(x\cos(\gamma)+y\sin(\gamma), -x\sin(\gamma)+y\cos(\gamma))d\gamma = p_\gamma(\xi)\ . \tag{2.9}$$

A widely used representation is obtained if we use the equivalent delta function $\int_{-\infty}^{+\infty} f(x)\delta(x-x_0)dx = f(x_0)$ [Arens et al. 2012, p. 1169] to rewrite this equation into

$$\mathscr{R}(f(x,y)) = \int_{-\infty}^{+\infty}\int_{-\infty}^{+\infty} f(x,y)\delta(x\cos(\gamma)+y\sin(\gamma)-\xi)dxdy = p_\gamma(\xi)\ . \tag{2.10}$$

Note that the resulting projection $p_\gamma(\xi)$ depends on the position in the source-detector-system (or more precisely, the distance from the center of rotation) as well as the relative position of both coordinate systems, expressed by the angle γ. The whole set of transformed values $p_\gamma(\xi)$ is called the Radon Space. A single projection can be obtained by linking the initial X-ray intensity to the final intensity measured at the X-ray detector by using the formula of Lambert-Beer that is described in eq. 2.5.

Radon and Fourier Space of the same image can be linked via the Fourier Slice Theorem. It states that the Fourier Transform, which is given by $\mathscr{F}(f(x)) = \int_{-\infty}^{+\infty} f(x)\exp(-2\pi ixt)dt$ of an one-dimensional image projection equals one of the radial lines of the two-dimensional Cartesian Fourier space of the object under the corresponding angle γ. We define the Fourier Space in Cartesian coordinates (u,v) as well as in polar coordinates (ψ,ω) for easier handling. The theorem can be expressed by

$$\mathscr{F}_1(p_\gamma(\xi)) = \mathscr{F}_2(f(x,y))|_\gamma = F(u,v)|_\gamma = F_P(\psi,\omega)|_{\omega=\gamma}\,. \tag{2.11}$$

Theoretically it is possible to apply an inverse two-dimensional Fourier transform to the one-dimensional Fourier transformed Radon Space in order to obtain the desired distribution of the attenuation values. The corresponding formula is given by

$$f(x,y) = \mathscr{R}_2^{-1}(\mathscr{R}_2(f(x,y)))\,. \tag{2.12}$$

However, due to practical limitations (e.g. necessary coordinate regridding and interpolation issues) this approach is usually not adopted. Instead, we can go a longer way depicted in fig. 2.11 by using the Fourier Slice Theorem and the two-dimensional inverse Fourier Transform, which is given by

$$f(x,y) = \mathscr{F}_2^{-1}F(u,v) = \int_{-\infty}^{\infty}\int_{-\infty}^{\infty} F(u,v)e^{2\pi i(x\cdot u + y\cdot v)}dudv \text{ [Buzug 2008, p. 179].} \tag{2.13}$$

For this, we express the path of γ directly in polar coordinates, whereby $\omega \equiv \gamma$ holds. After further simplification we yield

$$\begin{aligned}
f(x,y) &= \overbrace{\mathscr{F}_2^{-1}(\mathscr{F}_1(p_\gamma(\xi)))}^{\text{see eq. 2.11}} && (2.14)\\
&= \int_0^\pi \int_{-\infty}^{\infty} \mathscr{F}_1(p_\gamma(\psi))e^{2\pi i\psi(x\cos(\gamma)+y\sin(\gamma))}\psi d\psi d\gamma && (2.15)\\
&= \int_0^\pi \int_{-\infty}^{\infty}\int_{-\infty}^{\infty} p_\gamma(\psi)e^{-2\pi i\psi t}dt\cdot e^{2\pi i\psi(x\cos(\gamma)+y\sin(\gamma))}\psi d\psi d\gamma && (2.16)\\
&= \int_0^\pi \int_{-\infty}^{\infty} p_\gamma(\psi)\underbrace{\int_{-\infty}^{\infty}\psi e^{2\pi i\psi(x\cos(\gamma)+y\sin(\gamma)-t)}d\psi}_{\text{Filter Term}}dtd\gamma && (2.17)\\
&= \int_0^\pi \underbrace{p_\gamma(\psi)}_{\equiv p_\gamma(\xi)} * r(\underbrace{x\cos\gamma + y\sin(\gamma)}_{=\xi,\text{ see eq. 2.6}})d\gamma = \int_0^\pi (p_\gamma * r)(\xi)d\gamma\,. && (2.18)
\end{aligned}$$

In the step from eq. 2.17 to eq. 2.18 we have used the convolution theorem in the Fourier space that is given by $(f*g)(x) = \int_{-\infty}^{+\infty} f(\tau)g(x-\tau)d\tau$ [Buzug 2008, p. 124]. The final equation 2.18 is called the Filtered Back-Projection (FBP) and can be split in two parts: first, each set of projections is filtered by a filter term $r(t)$, the so-called ramp filter that is defined as

$$r(t) = \int_{-\infty}^{+\infty} \alpha e^{2\pi i\alpha t}d\alpha\,. \tag{2.19}$$

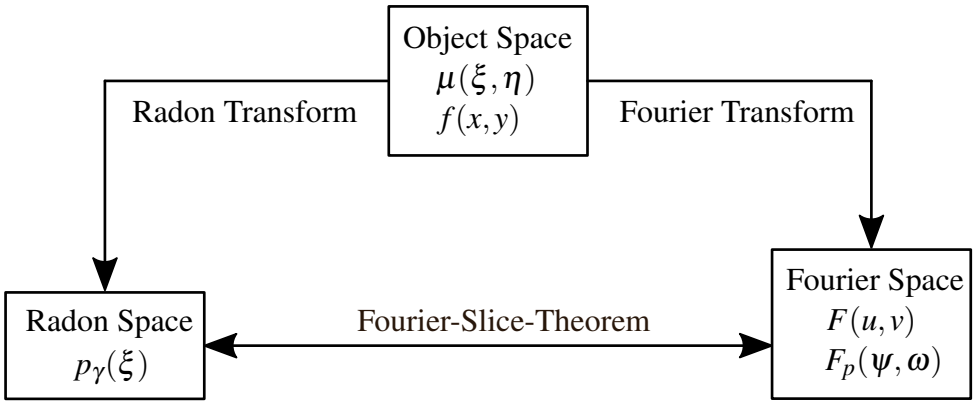

Figure 2.11.: Object, Radon and Fourier Space and related connections (adapted from [Buzug 2008, p. 167]).

The ramp filter $r(t)$ takes a necessary high-pass filtering into account to improve image quality. The second part consists of the back projection of these filtered data over the entire image. Figuratively speaking, the projection profiles are smeared back into the direction of the X-ray source. These two steps are repeated for all angles γ; the superposition of all profiles yields the desired presentation of the object space $f(x,y)$ [Buzug 2008; Schörner 2012; Turbell 2001, p. 151f, p. 22f, p. 13f]. The entire workflow for FBP is depicted in fig. 2.12.

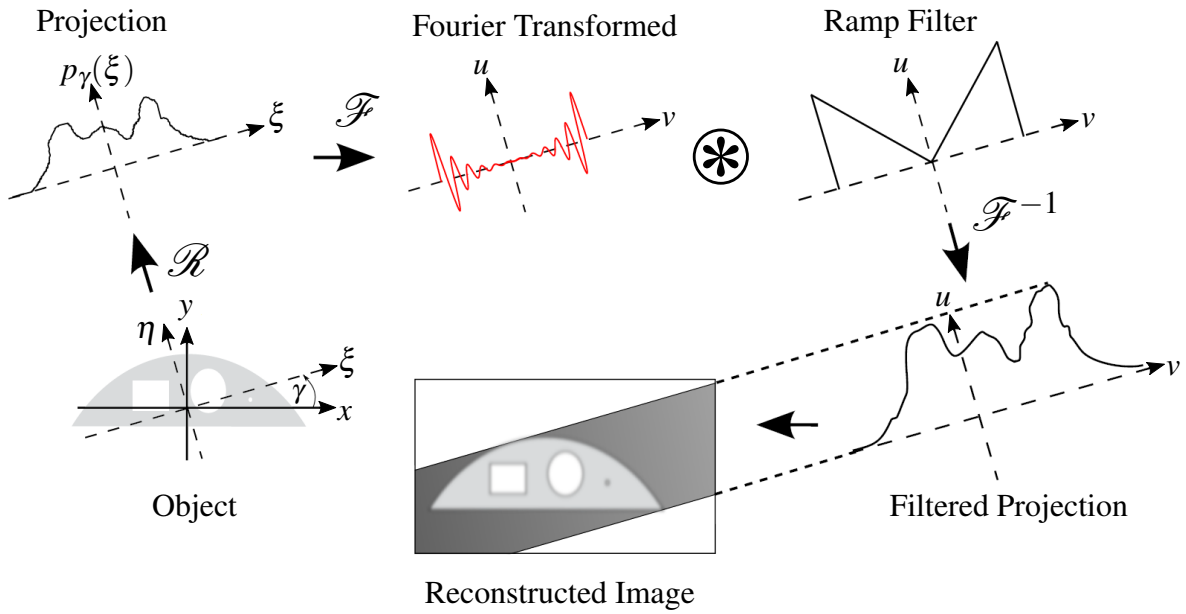

Figure 2.12.: Complete Workflow for FBP. For the sake of a clear arrangement not all coordinate systems are depicted (adapted from [Schrapp 2015]).

2.2.7. Artifacts in Computed Tomography

Reconstructed images are usually far from being flawless. Depending on machine parameters, the object shape and material, the reconstruction, and other influences the imaging quality can vary greatly. In this section we will give a short overview over the most important imaging errors and artifacts for our investigation [Buzug 2008, p. 423].

Beam Hardening: Low energetic photons are attenuated more rapidly compared to such of higher energy. As a consequence, after a short track in the workpiece the latter will predominate since most low energy photons have vanished. This phenomenon is called beam hardening since this way the average energy of the remaining beam is raised. The absorption of the first irradiated millimeters get overestimated which gives rise to artifacts (e.g. the outer layers of the object can appear to be of lighter color than the rest of the workpiece) and severe misinterpretations, including worsened part edge detection or the possibility to discriminate between different materials. A way of reducing beam hardening effects is to bring a filter of e.g. copper or aluminum in the X-ray beam before it enters the material. Hence, the softer fractions of the spectrum are filtered out prior to reaching the object of interest and enhanced surface edge detection is made possible. On the other side, the exposure time needs to be adjusted in order to compensate for the reduced intensity in the whole spectrum and the linked deterioration in signal-to-noise ratio (SNR). Additional methods to reduce or even compensate beam hardening completely are mostly software based [Hunter and McDavid 2012; Kruth et al. 2011]. Investigations have shown that beam hardening corrections improve the overall image quality, but can also have benefits for the accuracy [Dewulf et al. 2012]. One of the typical artifacts that occur due to beam hardening is the cupping artifact, which is depicted in fig. 2.13 together with a corrected image.

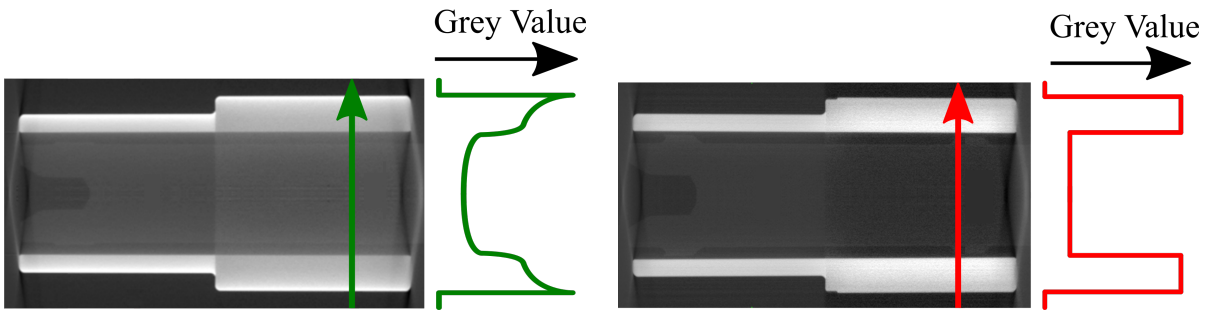

(a) Without Beam Hardening Correction **(b)** With Beam Hardening Correction

Figure 2.13.: Beam hardening and cupping artifacts. Due to the nonlinear absorption of X-rays the most outer layers of an object are depicted with higher grey values than the rest of the material (fig. 2.13a). With beam hardening correction the homogenous material appears as uniform grey values (fig. 2.13b).

Scatter As explained in sec. 2.2.4, two of the four dominant photon-matter interactions are scatter reactions. X-ray photons can be redirected in the workpiece, the air, the detector and other materials and give rise to an unwanted signal in the detector. Scatter reduces the CNR locally and makes it more difficult to separate the material edge from the background. When a FBP is used, typical streak artifacts can emerge [Buzug 2008; Kruth et al. 2011, p. 443].

Noise As for any measurement, noise is also an inherent property of CT. It can originate from many sources, such as electronic detector noise, quantization of incident X-ray photons, the signal processing and many more [Kruth et al. 2011].

Cone Beam Artifacts The cone shaped geometry of the X-ray beam gives rise to some additional artifacts. The most important one is also often called the cone beam effect. In order to obtain a complete sampling of the Radon space, of each parallel plane of the object an image must be captured, which is not possible with just a single circular trajectory. As consequence, artifacts occur especially for such objects that lie parallel to the detector-source-axis, but in a relatively shifted plane [Scarfe and Farman 2008]. This artifact can be corrected by adjusting the CT trajectory, e.g. to a helix or a circle and an additional line path [Schrapp 2015; Siemens AG 2015, p. 11, p. 11].

Ring Artifacts If defective pixels (e.g. such with an incorrect offset) are not corrected, this artifact can occur. The wrong voxel value follows a circular track as the object moves. Consequently, the pixel appears as a ring of sharp contrast with its midpoint being the center of rotation during the scan [Kruth et al. 2011].

Partial Volume Artifacts: Detector screens feature a pixel-wise alignment of singular detection elements. Consequently, the projected image can only be sampled with a finite resolution and since the edge of the object does usually not correspond with the edge of a detector pixel, the image gets blurred to some extent. Several other problems are linked to this partial image overlap. For instance, the artifact intensifies for cone beam CT performed with large aperture, since two, 180°-shifted projections of the same slice do not result in exactly the same image [Buzug 2008, p. 435, 446].

Limited Penetration Artifacts: In general, due to the attenuation of photon intensity that is inherent to all radiographic methods only a limited path can be probed. This range decreases with increasing attenuation properties of the investigated material. In order to visualize the problem, we consider a concave-convex shaped object in figure. 2.14. We assume a homogen material with attenuation coefficient μ and a typical noise level of $I/I_0 = 1\,\%$. Outside of the object attenuative processes are neglective, so that $I_{outside} = I_0$ holds. The radiation intensity can be calculated by use of the formula of Lambert-Beer (see sec. 2.2.4) that can be written as $I(\eta)/I_0 = \exp(-\mu\eta)$ with pathway η. Combining both formulas we can expect the noise to be of approximately the same level as the signal by

$$\eta = -\ln(1\,\%)\frac{1}{\mu_{Fe}} \approx 4.00\,\text{cm}\,. \tag{2.20}$$

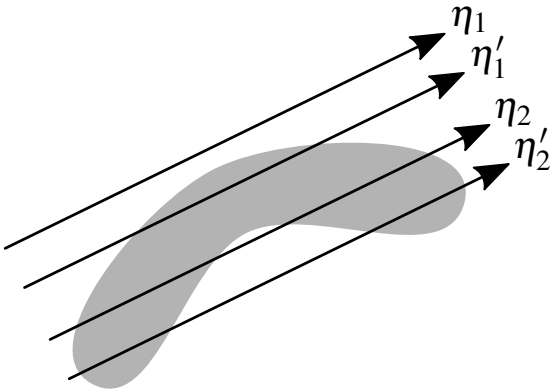

(a) X-ray Pathways of Various Length

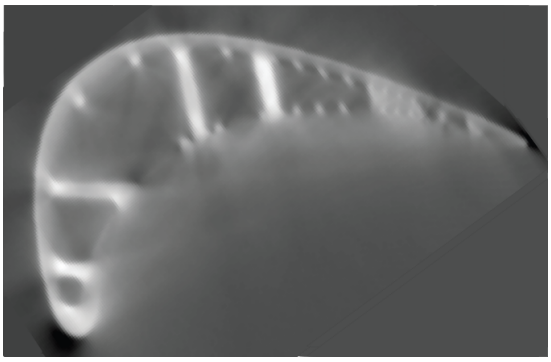

(b) Result in Reconstructed Volume

Figure 2.14.: Example for an artifact caused by limited penetration. Depending on the length of the pathway in the object (fig. 2.14a) the attenuation of the signal intensity can bee too much to obtain usable data. A resulting slice after reconstruction is depicted in fig. 2.14b (adapted from [Schrapp et al. 2014b]). While the convex side features a good SNR, the concave one suffers from bad contrast caused by indistuingishable differences in intensity and smears in the reconstructed image. A picture of this phenomenon for our application can be found in fig. 5.10.

Here we have used $\mu_{Fe} = 1.15\,\mathrm{cm}^{-1}$, which is roughly the attenuation coefficient of iron for photons with an energy of 200 keV (see also fig. 2.8). The interpretation of eq. 2.20 holds that no features with a path length of ca. 4 cm or more in iron can be resolved, since the superposition of noise does not permit any interpretable signal. Transferred to our example of fig. 2.14 we can easily investigate the consequences of this result: The path lengths of η_2 and η_2' are too long for the given material, so that their measured intensities become indistinguishable and disappear in the noise signal. The result is a blurred edge with very low contrast-to-noise ratio that does not contain any usable information. Contrary to that, the SNRs of the adjacent paths η_1 and η_1' are very good: The undiminished $I(\eta_1) = I_{outside} = I_0$ can easily be separated from the measured signal $I(\eta_1') >> I_{noise} = I_0/100$ and we obtain an excellent SNR and contrast [NIST 2017; Schrapp 2015, p. 27]. This explanation is investigated in detail for our application in sec. 5.5.2. A more convenient unit used to express the penetrability of a material is the half-thickness η_h. It is defined as the path length in the material that is needed to decrease the intensity to $\frac{I_0}{2}$. We calculate the half-thickness for iron with $\eta_{h,Fe} = -\frac{\ln(0.5)}{\mu_{Fe}} = 6.08\,\mathrm{mm}$ [Shultis and Faw 2002, p. 177].

2.3. Reverse Engineering

The fundamental idea of Reverse Engineering (RE) is to systematically acquire design information of an already existing object by measuring, testing and analyzing it, usually with the purpose of duplicating it. Contrary to the common engineering and manufacturing workflow, one does not end but start with the finally available object and traces it back to the CAD geometry and the design intents that lead to its production. Reverse Engineering is applied in various fields. Many modern products are inspired by biological designs, for instance the shape of airplane wings are similar to such of birds. RE of existing products is applied in military applications, car

manufacturing, medical purposes, design engineering, marketing enhancement, in the electronic and software industry but also in sectors associated with product piracy or plagiarism [Bidanda and Geng 2016; Yan and Gu 1996].

The motivations for RE (or more general, Digital Engineering) are manifold: in product development it can be desirable to have a model of an already designed object digitally available for further handling, e.g. turbine blade design or for aesthetic reasons in consumer products. If a part has been iteratively modified in field, CAD data are not available for the new geometry. For the sake of design data storage, RE can also be a remedy. Especially important are the possibilities to check produced parts for dimensional deviations due to manufacturing and to restore lost or unavailable blueprints to some extent [Geng and Bidanda 2017].

Generally speaking, the reverse engineering workflow can be divided in four parts: first, we need to acquire geometric information (e.g. images) of the object of interest. Depending on the data a second preprocessing step can be necessary, for instance to clean them from artifacts. Next the data undergo surface determination and meshing – aspects we will discuss in detail. The final step is to create the desired CAD model that is available for further handling [Várady et al. 1997]. For this part also other previously obtained knowledge is often considered, like several boundary conditions, experimentally won knowledge and many more.

In this section, we will provide a short overview of common data acquisition methods (sec. 2.3.1). Subsequently we will contemplate with the segmentation steps and further processing in section 2.3.2. We will also broach the issue of errors in RE in section 2.3.3. For more detailed information concerning this topic we refer to Raja and Fernandes (2008).

2.3.1. Contact and Optical Based Data Acquisition

Before all other steps, we desire to obtain as much geometric information from the object that is to reverse engineer and make it available for further processing. Many imaging and measuring methods are available for this purpose, but we will focus here only at the most common and important methodologies. See Savio et al. (2007) and Weckenmann et al. (2009) for more detailed discussions, including other RE devices like interferometry or ultrasonic sensors. Another possible imaging method is radiographic CT imaging, which we contemplated in detail in sec. 2.2.

Contact Methods

The easiest and most traditional approaches to obtain an object's geometry are the contact-based methodologies. A mechanical contact with the surface, often in form of a stylus or contact probe is obligatory. These methods have been used since decades and are usually capable to achieve a very high accuracy, but are more time-consuming than non-contact methods [Geng and Bidanda 2017].

Manual Measurement Probably the oldest possibility to determine the dimensional shape of an part is simply to measure it by hand. Experienced workers investigate the key dimensions with traditional instruments that comprise tools like measuring gages, calipers or angle finders. These key points can be entered into a CAD system that generates a three-dimensional model of the object. The process is quite flexible, but the accuracy is determined by subjective measuring skills of the worker and limitations concerning more complex or freeform shaped parts. These drawbacks, as well as the highly time consuming measuring process has lead to a rare use of this method nowadays [Geng and Bidanda 2017].

Contact Surface Scanners Coordinate Measuring Machines (CMMs) exist since the early 60s and are still among the most popular devices in RE. A stylus, which is highly sensitive to pressure, is repeatedly moved to the surface in order to scan the object of investigation. Touching forces below 500 µN can be sensed with a speed of up to 150 mm s^{-1}. These machines are well researched and are commercially available in many different configuration and types. Their use is quite costly and time consuming, but they feature superior scanning accuracies and resolutions in the range of 0.05 µm to 5 µm [Geng and Bidanda 2017; Savio et al. 2007].

Optical Scanners

Optical scan systems use light or laser beams to scan the surface of the object of investigation. Such scanners can be further subdivided in active and passive systems. Active devices utilize a light beam to scan the surface and obtain the desired data from the reflection of that beam, which is measured by light sensors. Contrary to that, passive optical solutions are able to work with ambient light. Hybrid systems, utilizing methods from both field exist as well. As a disadvantage compared to contact scanners, these methods are not capable of tracking small features or hollow structures at the surface of transparent objects. Also, the accuracy compared to tactile methods is usually lower and in the range of 0.01 mm to 1 mm for precision and accuracy [Bidanda and Geng 2016; Geng and Bidanda 2017]. While contact methods face difficulties for easily deformable surfaces, optical measurements of highly reflective materials or glass can transpire problematic [Heinzl et al. 2007]. Like for other methods of measurement, recalibration at regular intervals is crucial for precise measurements. For this purpose a multitude of testing artifacts are available [Mendricky 2015].

Active Optical Scanners The most common optical method is the classical **triangulation** laser scanner. A laser source emits a beam of laser light directly to the surface of the object while a camera detects the reflection of the beam. Since both angles of the beam compared to sender and receiver are known, it is possible to infer the position in space of the illuminated spot. This method is well-established, fast and robust. The accuracy lies in the range of ca. 25 µm.

A common alternative are **structured light** systems. Instead of a scanning beam, they project a light pattern at the surface of the target, which is simultaneously recorded. By analyzing the geometric distortion of the obtained picture, the measurement is accomplished. Several different projection patterns exist, each with their very own benefits and weaknesses. Obtainable accuracies are usually higher than for triangulation systems. The **shape-from-shadows** method works similar, but instead of projecting a pattern, it projects the shadow of an object with known geometry. This reference object is illuminated by a moving light source, causing its shadow to move as well. The image analyzis is performed analogously. The method is comparably cheap and requires only simple equipment. Nevertheless, the accuracy is rather poor, which is why the method is only seldom used. **Shape-from-shading** works similar again. Here, the object of unknown geometry is illuminated directly by a moving light source, which creates shading in the background. Depending on the angle of incident light, the shading on the surface of the object changes and is recorded as well. This approach is also rather inaccurate [Geng and Bidanda 2017].

Passive Optical Scanners If the light source of i.e. the triangulation method is replaced by a second camera, a **stereo scanning** system is formed. By combining two or more photographs via identification of common points and subsequent triangulation, it is possible to obtain geometric information without any additional light source. Unfortunately, often human participation or huge processing power is still required. The quality of the results is highly dependent on the sharpness of the surface texture and its reflectance. The method features small costs and is comparably simple. Due to its ability to detect features quickly and in real-time it is especially used in the fields of robotics or computer vision. Systems based on **texture gradients** utilize surface texture elements (so called texels). The farther away an object is, the smoother appears its surface. Since some geometric objects relate to an orientation (like tiles at a wall), the inspection and distortion of these element can be used to determine the geometry. The procedure is simple and cheap but achieves only low precision and accuracy. **Shape-from-focus** devices finally use the depth of field phenomenon. A lens is used as range finder by adjusting its focal plane and trying to minimize the blurriness of an investigated point at the surface in the obtained picture. The technique still achieves only low accuracies and features a non-uniform spatial resolution, which turns it inappropriate for commercial use [Geng and Bidanda 2017].

2.3.2. Surface Determination and Meshing of CT Data

Depending on the method for data acquisition the obtained geometry is available in different formats. For CT, this is a voxel data set of grey values from which we wish to derive the considered object's shape. In order to capture the contour of the workpiece, an edge detection process needs to take place. A common method to conduct this is the grey-value-threshold-based

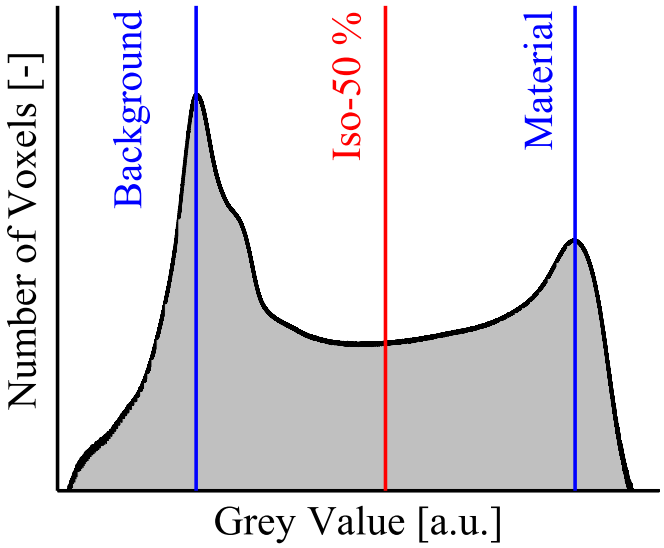

Figure 2.15.: Segmentation graph for iso-50 % method. Peaks for the background and the material are determined and the threshold is defined in the middle between these. In this example, every voxel with a grey value right of the red iso-50 %-line is supposed to belong to the object of investigation.

„iso-50 %“ value approach, which we want to sketch in the following. First, a histogram of the number of pixels is plotted versus the grey value. Usually the resulting graph exhibits a peak for each material in the beam path, which can vary greatly in magnitude according to the irradiated volume. Now, exactly two peaks are defined: one for the background (typically the surrounding air) and one for the object material like depicted in fig. 2.15. The abscissa is usually scaled logarithmic, the ordinate linear. The threshold that defines what is considered as background and what counts as material lies now in the middle of these two peaks, posing origin of the algorithm's name. If the considered object contains more than one material, additional iterations can be necessary. Performing a proper segmentation is not trivial: beam hardening effects and other present materials can influence the outcome of the algorithm. Experiments conducted at the KU Leuven have shown that the iso-50 % approach is often not ideal, with optimal threshold values lying between 35 % for aluminum and 90 % for steel [Dewulf et al. 2012; Kruth et al. 2011]. Also, due to the beam-hardening effect, a threshold fitting the outer surface of an object perfectly might be inappropriate for the inner structures. A possibility to improve results is to decrease the considered region of interest for segmentation. Rather than applying a global threshold, the considered area is splitted in several smaller pieces with the material peaks being determinated individually for each region. Especially complicated is edge detection for multiple materials since sharp borders between several peaks vanish more and more; here additional effects like acceleration voltage, integrating time and similar attenuation values come also into play. Among sophisticated algorithms, multi-energy approaches and data fusion approaches (see sec. 7.2) are considered to solve the emerging problems in this field [Dewulf et al. 2012; Kruth et al. 2011].

After performing the steps described above, we usually end up with a set of points that are located in the interface layer between object and surrounding or between different materials. For further handling this set – often referred to as point cloud – needs to be converted into a surface model that usually consists of a triangular mesh. This task is accomplished by a topological association of neighboring points. For this purpose, several algorithms are currently available, with the marching cube algorithm being among its most famous representatives [Lorensen and Cline 1987]. For a discussion of the drawbacks and benefits of this algorithm, see e.g. Ma et al. (2001). A good overview and classification of available meshing algorithms can be found at Várady et al. (1997). The final surface meshes are usually translated into the Standard Triangulation Language (STL)-format, which is also supported by most modern CAD systems [Kruth et al. 2011].

While we will only go so far for our investigations, STL-geometries are by no means the ideal outcome of a complete Reverse Engineering. The generated surface is usually not associated to the geometric features it is supposed to exhibit, like planes or spheres. Also for metrology, points to be measured need to be determined before the actual measurement can take place. For single features (e.g. the size of a plane, the diameter of a cylinder, etc.) fitting algorithms are available, which can determine these geometries, for instance based on a least squares fit approach. Nevertheless, this task proves to be quite cumbersome and less reliable for a more complex geometry. For a satisfactory RE-process, the entire STL surface needs to be converted into a parametrized CAD model [Kruth et al. 2011].

Once the final geometry is derived, the actual analyzis can take place. Often performed is the actual-to-nominal comparison, where the obtained model is compared to a known ideal geometry. We want to emphasize that for this purpose the direction (i.e. which part is used as actual or nominal geometry) is crucial. The difference between an incorrect comparison does not just result in a reversed sign but can also cause additional undesired effects and deviations. Other possible applications are, for instance, Finite-Element-calculations and investigations concerning wall-thickness or porosity. Some of these do not require an entire CAD model, but are also possible with voxel-based geometries or meshes [Kruth et al. 2011].

2.3.3. Errors in Reverse Engineering

In the course of a Reverse Engineering and Additive Manufacturing workflow, many errors can emerge due to various reasons. According to Mohaghegh et al. (2007) typical error sources are:

- **Sensing Errors:** These are errors that are linked to the precision of the image acquisition system and related measurements.
- **Approximation Errors:** These are errors occurring in the later handling of these data. Examples are errors that originate from fitting geometries to approximate the point sets. Also, the image reconstruction algorithm itself is afflicted to inaccuracies.

- **Numerical Errors:** Since most RE methods are carried out on computers or digital systems, only discrete values are permitted. As a result, by rounding the measured values to floating point numbers errors are introduced. Other numerical procedures and algorithms can introduce noise and worsen precision as well.
- **Object Wear and Tear:** Usually reverse-engineered objects are not investigated directly after production but a certain period of time of its life cycle. Until then, the shape can be affected by daily use, wear, rust or other external factors that prohibit exact measurements of the original geometry.
- **Particular Manufacturing Method:** Depending on the production process, postprocessing can be necessary. Typical methods comprise blasting, blending, polishing or machining by hand – all comparably hard to control treatments that lead to irreproducible distortions of the surface. Nevertheless, these aberrations are captured by RE and taken as reference.

By summation of errors, an overall error can develop that exceeds the originally defined tolerances of the part. So it seems reasonable to take a closer look at the workflow, which is depicted in fig. 2.16. We start with an initial design with reference size A, as it was constructed e.g. in CAD. Since this is actually what we want to obtain finally, no errors are present. Due to manufacturing and postprocessing, a first error δ_M is introduced to the part geometry. We can assume that this error does not surpass the specified tolerances $\delta_T > \delta_M$ of the part, since it would be declared as waste and removed from the production otherwise (given that the part is relatively new). Since we want to reverse-engineer this workpiece, we introduce a new, additional error δ_{RE}. It is made up of many different factors. The most important ones are the precision of our measurement tools and the loss of accuracy that is caused by the generation of a CAD model, since it requires an approximation of the geometry. But it is also possible that the creation of a CAD model by hand enables to compensate for some of the errors introduced in earlier stages. Since we have usually no detailed knowledge about the quality of the RE-approach, the generated model can already surpass the originally defined tolerance, so that $\delta_T < \delta_M + \delta_{RE}$ holds. By manufacturing the replicated part via AM the second production error δ_{AM} is introduced. If originally a conventional manufacturing method was chosen this error is not necessarily linked to it due to the different way of production. Note that some or all errors can compensate each other to some extent, so that the replicated part can be very similar to the initial design, even if some steps in between lack precision. Because of that it is necessary to investigate each step in between separately as far as possible. If the chain starts with an already reverse engineered part, even more errors can accumulate and lead to a worsened fidelity [Geng and Bidanda 2017].
We want to add that this explanation approach is not exactly true, since it considers the mean value of several considered parts A to stay identical during the entire workflow. However, if we assume a set of parts that undergo similar treatment and handling, it seems comprehensible to us

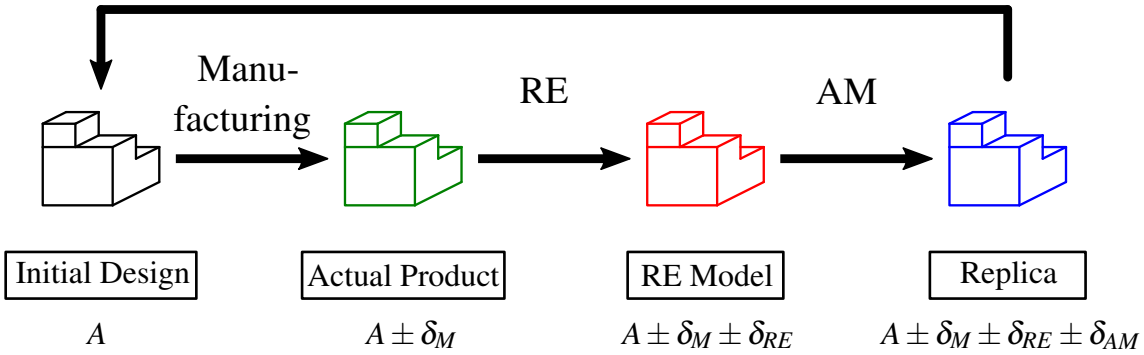

Figure 2.16.: Error propagation in the Reverse Engineering workflow. The initially intended geometry is superpositioned by errors introduced from manufacturing, RE and AM (adapted from [Geng and Bidanda 2017]).

that this condition is not necessarily fulfilled. For instance, if the object underwent productive use, wear and corrosion can lead to a degradation of the mean metrologic value while an increase of material seems intuitively unlikely. On the other side, if the part was produced via casting that has been incorrectly planned or conducted, a certain off-value is added to its geometry due to thermic shrinking. That means that the characteristic of the part distribution does not only get wider, but also the mean value shifts due to systematic errors with A_M, A_{RE} and A_{AM}. Additionally, a simple addition of all emerging errors like performed by Geng and Bidanda is not entirely correct in the strict sense, since errors can influence and compensate each other to some degree. By reason of these considerations we provide an enhanced examination at this point.

The standard deviation δ of a value $A(x_1, x_2, \ldots, x_N)$ that depends on N independent parameters and each of them yield the Gaussian-distributed results x_i can be calculated by

$$\delta = \sqrt{\sum_{i=1}^{N} \left(\frac{\partial A}{\partial x_i} \delta x_i \right)^2} \quad \text{[Eden and Gebhard 2014, p. 34].} \tag{2.21}$$

If we assume a shift of the mean value $A_{new} = A_{old} + A_M + A_{RE} + A_{AM}$, with A_x being able to be negativ, the equation simplifies to

$$\delta_{A_{new}} = \sqrt{\delta_{A_M}^2 + \delta_{A_{RE}}^2 + \delta_{A_{AM}}^2} \,. \tag{2.22}$$

This deviation is superposed to the aberration caused by the shift of the mean value, so that the dimension of the final part is given by:

$$A_{new} = A_{old} + A_M + A_{RE} + A_{AM} \pm \sqrt{\delta_{A_M}^2 + \delta_{A_{RE}}^2 + \delta_{A_{AM}}^2} \,. \tag{2.23}$$

Usually the mean value shifts A_x are not known or underlie a certain variability as well. However, if there are given deviations – e.g. such that have been determined experimentally – they have to be treated analogously by eq. 2.22.

2.4. Additive Manufacturing Methods for Metals

Additive Manufacturing (AM) has gained increasing attention within the last years. Related methods are capable of producing customized and highly complex parts that might even prove impossible to produce at all utilizing only conventional methods. AM is defined as "a process of joining materials to make objects from 3D model data, usually layer upon layer, as opposed to subtractive manufacturing methodologies" [ASTM 2013]. Since contemplating with this new technology in detail is beyond the scope of this thesis we will subsequently give a very short summary of metal processing AM methods, focusing on the one needed for our investigations. An excellent overview of currently available printing technologies can be found in [Medellin-Castillo et al. 2010].

All established techniques follow the same basic workflow. First, a three dimensional CAD model is needed. The geometry data are typically derived from available blueprints, but can also originate from alternative sources like scans of already existing assemblies. The most widespread geometry input format is called Stereolitography, Standard Triangulation or Tessellation Language (STL), which features a plain data structure based on triangular facet data. It can be necessary to rework parts of the workpiece in order to prepare it for manufacturing. In some cases additional support structures need to be added as well. In the next step, the model is sliced in several layers of a fixed thickness. These data are subsequently transferred to the AM system that generates each layer separately in a repetitive material deposition process. Usually an additional treatment including cleaning the part and conducting a surface finish is applied [Herzog et al. 2016; Lachmayer et al. 2016; Lee and Woo 2000, p. 20].

The three most important approaches are Electron Beam Melting (EBM)[3], Laser Metal Deposition (LMD) and Selective Laser Melting (SLM)[4]. For all of these, the raw material needs to be on hand as pulverized feedstock. Common metals for Additive Manufacturing are steel and Cobalt-chromium as well as Aluminum-, Titan- and Nickel-based alloys [Herzog et al. 2016]. All technologies listed here are able to obtain high filling densities of $> 99.9\,\%$ [Lachmayer et al. 2016, p. 28]. They also achieve similar accuracies of and surface finish R_a of ca. 5 µm to 20 µm) [Levy et al. 2003].

Selective Laser Melting For SLM, a fine metal powder is arranged in thin layers, typically several µm thick. A feeding system in combination with a recoater blade achieves a uniform powder deposition (grain fraction 10 µm to 45 µm) in each layer and provides a continuous supply of new material. The process chamber is heated up to 500 °C in order to avoid distortion caused

[3]For most AM techniques, a multitude of labels exist due to their identifiers being protected by patents. Alternative terms for EBM comprise Direct Metal Deposition (DMD), Laser Engineered Net Shaping (LENS), laser cladding or laser deposition welding.

[4]This process is also known as Laser Beam Melting (LBM), Direct Metal Laser Sintering (DMLS), LaserCUSING, Laser Metal Fusion (LMF) or industrial 3D printing.

by thermal stress. The chamber features a nitrogen-argon atmosphere with less than 0.1 % oxygen to avoid undesired reactions of the metal powder and also shield the melt from secondary process products like weld spatter or fume. A laser beam is steered via galvanometer scanner, so it can hit the powder bed at the desired spots and selectively melts the present material. Typical beam sources are single mode fiber lasers in continuous wave mode, which work with a wavelength of ca. 1060 nm to 1080 nm and focal spot sizes of 50 µm to 180 µm, reaching a power of up to 1 kW and a speed of 15 m s^{-1}. In general, the pattern of the beam follows a special calculated trajectory – the so called scan strategy – that lets the melt tracks overlap to a certain degree. The melted material solidifies subsequently along the heated tracks and forms a fix connection. As final step of the cycle, the build plate is lowered and a new layer of powder is distributed on top of the workpiece. The procedure is repeated until the part is finished and can be culled from the machine [Bremen et al. 2012; Herzog et al. 2016]. A scheme of a Selective Laser Melting-system is depicted in fig. 2.17.

The accuracy of SLM has been subject to several studies. Depending on the material and methodology used, different values have been derived so far for the accuracy. For the outer geometry, accuracies better than 40 µm can be achieved [Ben and Jean-Pierre 2007]. The accuracy concerning internal features has been determined to have a standard error larger than 5 % compared to the target size. One of the greatest drawbacks of the method was found to be its quality of surface finish. Typically only a comparably high surface roughness can be achieved with values for the averaged roughness of ca. R_a=10 µm, rendering an expensive subsequent surface treatment obligatory for many purposes. Manufacturing accuracies are discussed in detail in sec. 6. SLM is used for instance in the tool- and mold-making industry or in the production of working prototypes [Bremen et al. 2012; Ghani et al. 2017].

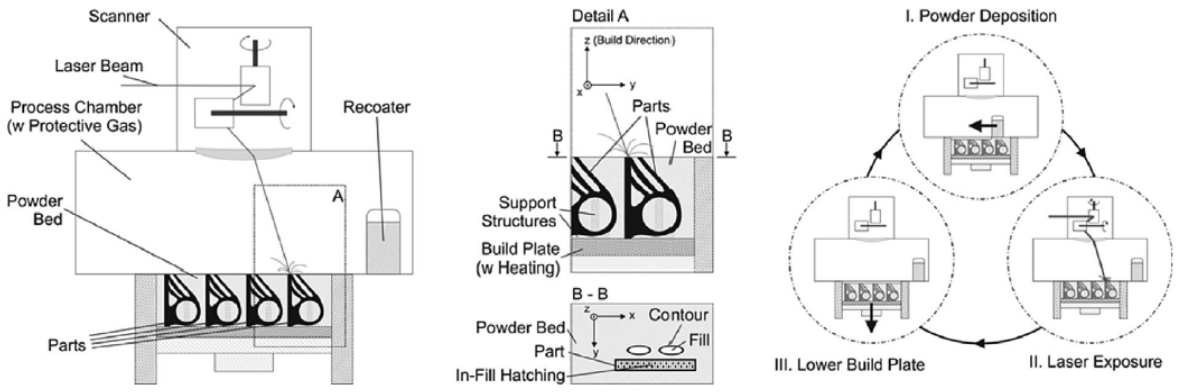

Figure 2.17.: Typical build-up of an Selective Laser Melting machine. The production cycle is illustrated on the right [Herzog et al. 2016].

Electron Beam Melting This technique basically relies on the same build-up like SLM, but instead of a laser beam, the melting process is induced in a different way. An electron gun

Table 2.1.: Comparison of common metal processing Additive Manufacturing methods [Herzog et al. 2016; Lachmayer et al. 2016, p. 28].

	SLM	EBM	LMD
Layer Thickness [µm]	20 to 150	$<$ 50 to 200	40 to 1000
Max. Work Area [mm]	800×400	$\varnothing$ 350	Unlimited
Max. Resolution [µm]	< 30	100	> 30
Energy Density [J mm^{-3}]	< 100	150 to 900	90 to 220
Scan Speed [mm s^{-1}]	250	100	2.5 to 25

accelerates electrons with an acceleration voltage of up to 60 keV and a high beam current[5] of 5 mA to 10 mA. An optic system of magnetic scan coils and electromagnetic lenses directs the beam to the surface to the powder, analogous to the galvanometer of SLM. This way the scan speed can reach 1 m s^{-1} during the melting process. As work environment a vacuum of < 100 mPa is applied. Alternatively an inflow of helium up to 1 Pa can be used in order to prevent the powder of becoming electrically charged and to accelerate the cooling process [Herzog et al. 2016].

Laser Metal Deposition Contrary to the previously mentioned methods, a LMD system does not rely on powder beds. The machines are basically build up like common Fused Deposition Modeling (FDM) printers that have become widespread for personal use in the last years. The powder or wire feedstock is fed into a nozzle that shoots it towards the part surface where it gets melted via Nd:YAG, diode or CO_2 laser. During this procedure, an argon or helium atmosphere is provided. Wire-based raw materials can alternatively be processed via electron or arc beam. This way the material is simultaneously fused and applied to the workpiece. The nozzles move over the work platform and distribute the material according to the desired structure. This method is rarely used to produce complete components but has gained attraction for repair measurements, e.g. for components of airplane turbines [Herzog et al. 2016; Lachmayer et al. 2016, p. 25].

[5] Before the actual manufacturing process, the beam is used to heat up the powder bed. For this purpose, currents of 30 mA and an even higher beam speed of $10 \cdot 10^4$ mm s^{-1} are applied. This way temperatures of 700 °C and beyond can be reached [Herzog et al. 2016].

3. Preliminary Work

Most parts of the replication toolchain have already been developed and brought to maturity in various fields. In this section we will give a brief insight in already existing solutions and assess their usability for our purpose. For special applications several – often spectacular – other examples can be found, e.g. replication of historical art pieces or fossils. Likewise, Appleby et al. (2014) manufactured a replica of the skeleton of the British King Richard III, which is now exhibited. A more detailed overview is provided by Thompson et al. (2016).

3.1. Medicine

Imaging techniques have a long tradition in life sciences. Ancient Romans and Greeks already possessed knowledge of optical magnification and the first operating microscope for biological studies dates back to the 17th century [Bardell 2005]. Computed Tomography (CT) found its way into clinical practice in the 70s and has greatly evolved since [Kalender 2006]. But in the last decades, also Additive Manufacturing methodologies have started to gain attraction. In fact, the first combination of RE with AM was accomplished in life sciences in 1990 by Mankovich et al. (1990).

These days, several areas use the combined workflow of both, imaging as well as generative manufacturing technologies. A common field of application is the education of ongoing physicians. For instance, are bone replicas, produced from image data of real bones, able to overcome some of the disadvantages real bones hold, like preservation issues or biological risks. Artifacts produced via rapid prototyping (RP) can enhance learning and enable to show even seldom anatomic malformations with a lifelike example. Also, complex surgical procedures can be mastered by intensive training at such artifacts. Patients can also benefit directly, since the process of surgical operations can be explained in a more demonstrative manner. Due to this benefits, education of students and patients is among the most important operational areas. Since 2015, over 70 % of clinical 3D-printing has been used in order to produce anatomic models [Martelli et al. 2016; Rengier et al. 2010]. The possibility to produce patient-specific surgical tools exist as well, for instance screw guide templates that help the surgeon to fixate bone screws during operation more easily [Mok et al. 2016].

The use of patient-specific tissue and organ replicas has proven very valuable for preoperative planing and training. Surgeons feel more confident during actual operations and can perform them more quickly if they have trained adequately before with models and determined the most suitable surgery strategy. Since 2008, almost half of the published papers in this field have broached the issue of surgery planing and training [Ávila et al. 2016].

A comparably unfrequently performed possibility to use AM is the field of medical research. For example, printed blood vessels and artificial airways allow more realistic hemodynamic as well as aerodynamic investigations and patient-based phantoms can improve the ability to simulate *in*

Figure 3.1.: Already existing examples for the use of RE and AM in a combined workflow. Left: prosthesis for scapula replacement, manufactured via Selective Laser Melting of titan (excised tumor displayed as well). Right: AIO Robotics ZEUS, commercial 3D-printer with replication ability [AIO Robotics, Inc. 2017; Fan et al. 2015].

vivo conditions. Only 5 % of all considered published papers related to anatomy since 2008 had medical research upon anatomical replicas as topic, which is especially low since many of these investigations were carried out with the purpose of subsequent publication [Rengier et al. 2010; Ávila et al. 2016].

While all purposes mentioned above are primarily carried out via comparably simple 3D-printer for home use and with polymer materials, also more sophisticated approaches exist to construct fully operative implants. While prostheses are commercially available in standard sizes, for some purposes individual ones can be necessary. This is for instance the case, if tumors have destroyed tissue or bones at extraordinary spaces that cannot be covered easily via off-the-shelf implants. Also, the dimensions of a patient's anatomy can be out of the usual range or anatomical peculiarities make more advanced customization obligatory. Therefore, prostheses manufactured via AM are used especially in maxillofacial and orthopedic operations were these advantages take particularly effect. An example for a scapula prosthesis as replacement for the previously by cancer destroyed tissue is shown in fig. 3.1. Processed materials comprise polymers as well as ceramics and metals like Titan-alloys for load-bearing applications [Rengier et al. 2010]. In maxillofacial surgery, also soft tissue prosthesis have been printed so far. Typical example are ears or the nose. Experimentally, parts of the eye and other tissues have been produced as well, but are far less widespread than metal made devices [Martelli et al. 2016; Shafiee and Atala 2016; Subburaj et al. 2007; Wu et al. 2007]. Fingers and knee joints for use in prosthesises have also been manufactured so far [Curodeau et al. 2000; De Laurentis and Mavroidis 2002].

Table 3.1 provides a non-exhaustive overview of current applications of RE in combination with AM in implant surgery. Despite the promising results, also some negative aspects need to be mentioned. Drawbacks of the new method in comparison to standard implants are high costs and the lack of intraoperative flexibility. Also, the time needed for processing the image data, design of the device and manufacturing time have proven cumbersome for its spread. In general,

the manufacturing of fully operational prosthesis is much more challenging than its counterparts, for instance for educational use. Since 2014, only 8 % of relevant published papers related to medical AM have been dealing with implant design. Considering the broad availability of standard implants that fit sufficiently for most patients, one can consider custom-made prostheses to be more of a niche application that is currently still in its infancy [Martelli et al. 2016; Wong 2016].

Table 3.1.: Overview over some previous applications of RE with Additive Manufacturing to manufacture patient specific prostheses. Abbreviations refer to: polymethylmethacrylate (PMMA), polyether ether ketone (PEEK), acrylonitrile butadiene styrene (ABS), 3D-Printing (3DP), Electron Beam Melting (EBM), Fused Deposition Modeling (FDM), Selective Laser Melting (SLM) and Computerized Numerical Control (CNC).
***The authors only name "a stereolithographic technique" without specifying further details.**

Body Part	Imaging	AM	Material	Source
Skullcap	CT	EBM	Titan	[Parthasarathy 2014]
Skullcap	CT	SLM	Titan	[Jardini et al. 2014]
Skullcap	CT	STL*	Hydroxyapatite	[Staffa et al. 2012]
Skullcap	CT	CNC	PEEK	[Parthasarathy 2014]
Sternum, Rips	CT	EBM	Titan	[Aranda et al. 2015]
Heel Bone	CT	EBM	Titan	[Imanishi and Choong 2015]
Tooth	Optical Scan	3DP	Wax Pattern for Zirconia Ceramic Sintering	[Sun and Zhang 2012]
Collarbone Shoulder Blade Pelvis (Partial)	CT CT CT	EBM EBM EBM	Titan Titan Titan	[Fan et al. 2015]
Pelvis (Partial)	CT	SLM	Titan	[Wong et al. 2015]
Jawbone	CT	3DP	α-Tricalcium Phosphate	[Saijo et al. 2009]
Face	Optical Scan	CNC	Wax Mold for Silicone Casting	[Tsuji et al. 2004]
Ear Conch	CT	FDM	ABS and Wax Molds for Silicone Casting	[Subburaj et al. 2007]
Nose	CT	STL	Photopolymer Mold for Silicone Casting	[Qiu et al. 2011]

3.2. Commercial 3D-Printers

Within the last years, 3D-printers have gained access to private households. Costs have reached a niveau that make it nowadays possible for individuals to afford such a device. It is used for model making, personalization of accessories or for creative purposes such as art, instruments or product design [Lachmayer et al. 2016, p. 1]. The possibility to produce parts in a stable, repeatable process has turned out to be a tempting chance in the do-it-yourself community.
With an increasing number of potential customers, also the quantity of providers has risen. Meanwhile it does not seem enough to just offer a printing device, but the need for unique features has emerged. One of the gadgets some of the newest printer bring with them is a

Table 3.2.: Overview of commercially available 3D-printers for end users that have been equipped with surface laser scanners. All systems operate on Fused Filament Fabrication (FFF). Material abbreviations refer to polylactic acid (PLA) and acrylonitrile butadiene styrene (ABS). Specifications were provided by producer homepages [AIO Robotics, Inc. 2017; FLUX, Inc. 2017; XYZprinting, Inc. 2017].

Name	Manufacturer	Print Resolution	Scan Res.	Materials
ZEUS	AIO Robotics, Inc.	$(80 \times 120 \times 200)\,\mu m$	150 µm	PLA
da Vinci 1.0 Pro	XYZprinting, Inc.	100 µm	250 µm	PLA/ABS
FLUX Delta+	FLUX, Inc.	$(200 \times 200 \times 50)\,\mu m$	1 mm to 2 mm	PLA

laser-based 3D-scanner that enables the devices to determine the shape of an object. Table 3.2 shows commercially available 3D printers in the home-use price category that are equipped with laser scanners.

The combination of 3D-scanner with 3D-printer is basically a combination of RE with AM capabilities. So far, only the ZEUS (*AIO Robotics, Inc.*, Los Angeles, USA, see fig. 3.1) has been explicitly advertised with its replication abilities, for example to produce replacement for broken toys.

The quality of the laser scanner varies greatly. For instance, the FLUX Delta+ (*FLUX Inc.*, Taipei, Taiwan) only possesses experimental scanning abilities which allow scans with a very poor quality of up to 1 mm. But even the best commercial hobby printers do not even come close to the accuracy modern optical industry scanners can offer (see sec. 2.3.1). As a matter of course they start in a totally different price category and aim at a different group of customers. Also, processible materials are only certain polymers that cannot withstand serious loads. The print resolutions are not yet comparable to most industrial needs as well.

A possible improvement is to use industrial grade scanners and AM systems. Since these devices are able to resolve remarkably smaller structures and print with much higher quality, functional replicas for productive use seem feasible. The idea has been proposed by various researchers and termed differently. So suggested Fischer (2000) the idea of a ”3D-fax” while Geng and Bidanda (2017) termed it a ”3D-copier”. Surprisingly, to our knowledge this idea has barely been strived outside of research and educational sectors so far. A reason might be that high-precision RE systems are still costly, while AM machines have dropped in price just in the recent years. Also, with such a setup only superficial scans and replicas are possible, while replications of parts with internal structure call for CT or destructive measurements. We assume that the application areas for such limited and expensive systems are not numerous.

4. Retrieval of Imaging Data

The first step of each Reverse Engineering process is always the data acquisition. In this section we will describe the turbine blade under investigation (sec. 4.1) and our CT setup (sec. 4.2). Subsequently we will also deal with the generation of imaging data from other sources in sec. 4.3 and 4.4, respectively.

4.1. Turbine Blades for Investigation

The turbine blade used for the investigations is depicted in fig. 4.1 (and schematically in fig. 2.2). The blade itself was not designed to be used in a real turbine but only for our investigation purposes. Because of that, it features different internal and external features that can normally not be seen in the given form and composition at a real blade, but allows to investigate many different geometries at once. It is manufactured entirely by use of Selective Laser Melting. As only material the alloy "EOS NickelAlloy HX" was used; this is a nickel-based superalloy which is able to withstand temperatures up to 1200 °C. Heat treatments are possible as well as several machining procedures after production. Referring to manufacturer information, a typical achievable part accuracy of ca. 50 µm can be achieved. Detailed information about the material are provided in its datasheet in the appendix (see sec. B.2). We also tried to model the attenuation characteristics of the material using the simulation software aRTist (Analytical RT Inspection Simulation Tool, *Bundesanstalt für Materialforschung und -Prüfung (BAM)*, Berlin, Germany). Results are provided in sec. B.1. A penetrability estimation analogous to the one provided in sec. 2.2.7 yields a maximum allowed material thickness of ca. 3.4 cm, i.e. the material is even harder to investigate than iron (assuming a noise fraction of $I/I_0 = 1\,\%$ and an attenuation coefficient of $\mu_{HX} = 1.34\,\mathrm{cm}^{-1}$; half value thickness is given by ca. 5.2 mm).
After Additive Manufacturing, the blade was blasted in order to burr sharp edges. This production step is not expected to distinctly alter the surface. During the manufacturing process an additional layer of molten metal was attached to the socket in order to fixate it to the working platform. For the production no falsework was necessary. We investigate two blades based on the same drawing. The only difference was the manufacturing method; the first blade (termed blade I from now on) was produced with a slice thickness of 20 µm, while the second blade (blade II) holds only 40 µm. From a visual point of view both blades do barely exhibit any significant differences or aberrations.

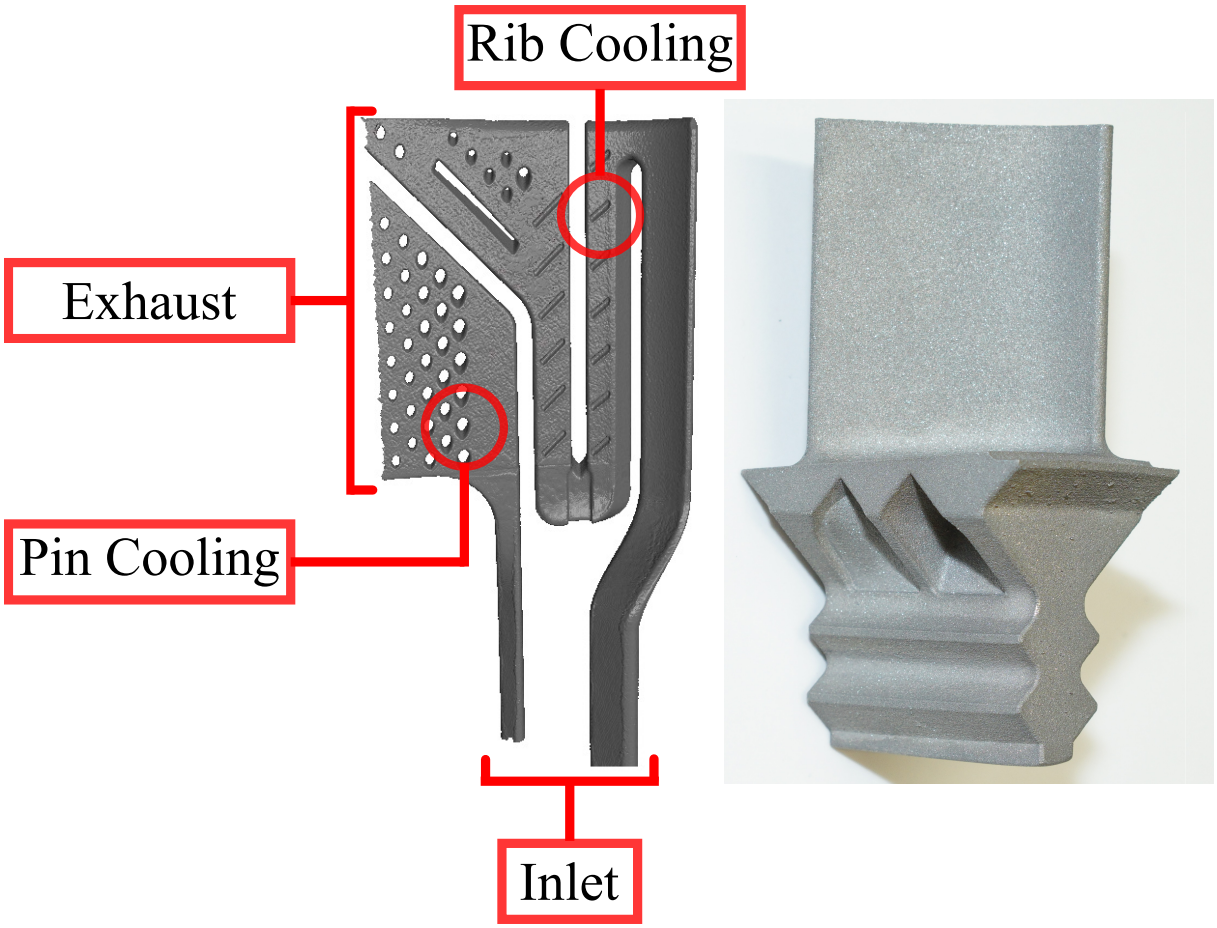

Figure 4.1.: The SLM-manufactured turbine blade for our investigations. Left: internal structure of the blade with most important features indicated (geometry derived from CAD-file). Right: final produced part. Both pictures are aligned in the same way, i.e. the exhaust is located left for both. The complete blade has a total height of 80 mm.

4.2. Set-Up for Low Energy Computed Tomography

Figure 4.2 shows the setup for our low-energy CT-scans. It consists of a cone-beam X-ray tube **A**, an attachment for the probe **B** and a detector **C**. These gadgets are described below. Both – attachment and detector – are mounted on a linear bearing, allowing to precisely adjust the distance between each device. The mount for the object of investigation is equipped with a precise motor that allows to move the object during the tomographic scan. X-ray source and detector can be lifted or lowered independently from each other. All CT scans with energies up to 225 keV in this thesis were performed by this setup.

X-ray Tube For all recordings we used a water-cooled transmission X-ray tube type XT9225-TED (*Viscom AG*, Hannover, Germany) with a tungsten target. The source can reach a maximum acceleration voltage of 225 keV and a maximum anode current of 1 A. Maximum target power is given with 120 W and focal spot size with $\leq 120\,\mu$m.

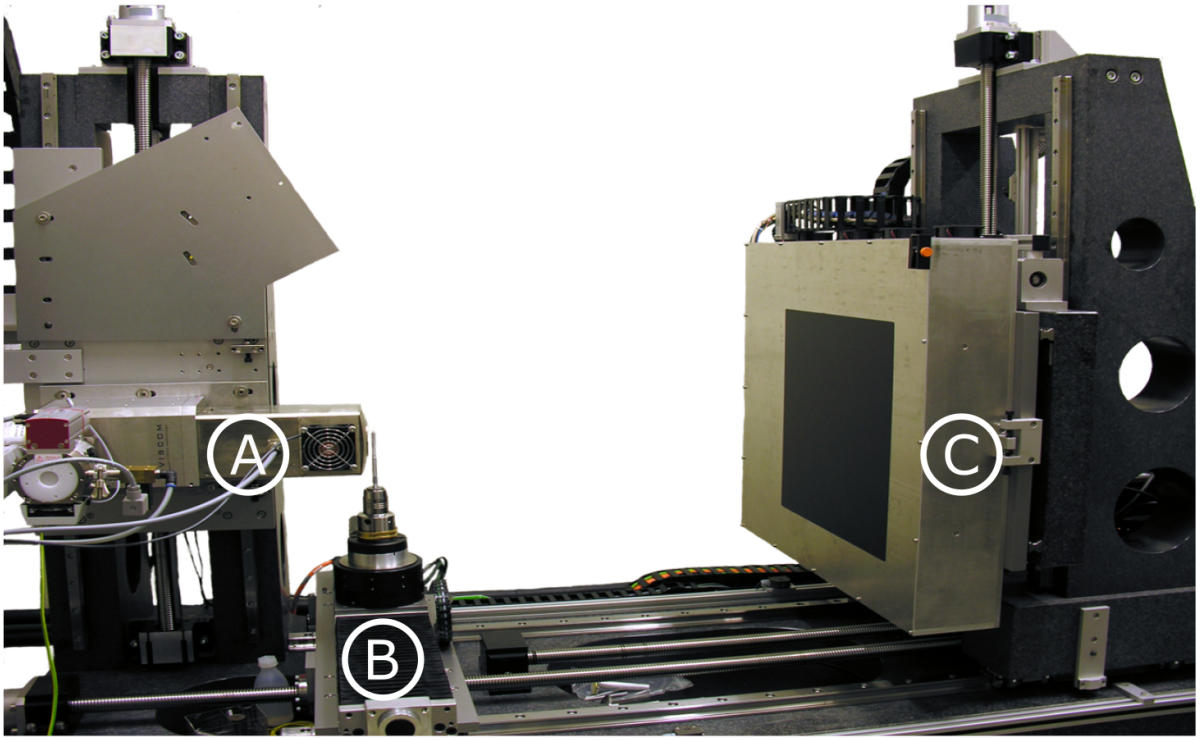

Figure 4.2.: Our setup for image- and CT-acquisition. It consists of X-ray source (A), attachment for the object (B) and detector screen (C). All low energy CT measurements have been conducted by use of this installation (adapted from [Schrapp 2015]).

Detector We used a flat panel detector type XRD 1621 AN14 EHS (*PerkinElmer, Inc.*, Waltham, USA). The system utilizes a (41×41) cm screen with a pixel size of 200 µm (equals a lateral resolution of 2048 pixels) and a dynamic range of 16 bit. It features a gadolinium oxysulfide (GOS)-based scintillator (see sec. 2.2.5) and a fiber optic interface.

Acquisition Protocol Before each scan, six images are acquired at different voltages between 0 kV and 225 kV (equals maximum possible voltage of the X-ray tube). The first picture is used to determine the offset caused by intrinsic electronic noise (dark current) with no radiation present. The remaining recordings are utilized to account for the varying luminance behavior of each pixel at different photon energies. After each CT scan, these information are used in order to apply a gain and offset correction to the images. After the scan the object is removed and replaced by a metal rod of 13 mm in diameter that covers the whole vertical field of view. Subsequently, a CT of this rod is performed; these data are used for the algorithm to determine the actual axis of rotation and compensate for occurring distortions of it during the first scan. The CT setup is calibrated for geometric distortions regularly by use of artifacts to compensate possible inaccuracies of the measurement system for source-detector-distance (SDD) and source-object-distance (SOD).

In order to improve the signal-to-noise ratio, each image is the result of an averaging process over several separate pictures. The number of images for the averaging process can be determined

Table 4.1.: Used parameters for the low energy Computed Tomography. The target position was changed between scans, so that some values might not be directly comparable.

	Blade I	Blade II
Acceleration Voltage	225 keV	220 keV
Filament Current	420 µA	300 µA
Power	94.5 W	55.0 W
Filter	1 mm Copper	1 mm Copper
SOD	195 mm	195 mm
SDD	780 mm	780 mm
Magnification	4.00	4.00
Voxel Size	50 µm	50 µm
Exposure Time	500 ms	500 ms
Number of Images for Adjustment Averaging	128	128
Number of Images for Scan Averaging	32	16
Number of Projections for Scan	2500	2000
Number of Projections for Rod Calibration	72	72
Duration of Complete Scan	ca. 11 h	ca. 4 h 30 min

independently for the calibration recordings and the ones necessary for a single image during the actual CT. For our usage the number of pictures needed for each rod calibration image are the same like for each CT image. All relevant machine parameters are given in tab. 4.1. Note that the target position was altered between the scans, so some values are not directly comparable. Especially a lower filament current was observed to obtain the same result after a position change. This is probably caused by a less abraded wolfram coating at the new focal spot position. Reconstruction was performed using the algorithm proposed by Feldkamp, Davis and Kress (FDK), which is basically an extension of the Filtered Back-Projection to three spatial dimensions (see sec. 2.2.6). We applied additional corrections for beam hardening and ring artifacts.

4.3. High and Medium Energy Computed Tomographies

All in all we have three different CT scans available for blade I, each one has been performed by use of a different acceleration voltage: we have scans featuring 225 keV, 450 keV and 7.6 MeV available; we will refer to them as low, medium and high energy (or Linac) scans from now on. While the first one was conducted by our own installation (described in sec. 4.2) the latter two were performed by an external service provider. All available information are provided in tab. 4.2 for comparison.

Table 4.2.: Parameter overview for all CT scans of blade I. For empty fields no information was available.

	Low Energy	Medium Energy	High Energy
Acceleration Voltage	225 keV	450 keV	7.6 MeV
Focal Spot Size	ca. 50 µm	–	1.9 mm to 2.5 mm
Filter	1 mm Copper	–	No Filtering
SOD	195 mm	–	2962.12 mm
SDD	780 mm	–	4346.94 mm
Magnification	4.00	–	1.47
Voxel Size	50 µm	$(70 \times 70 \times 280)$ µm	$(280 \times 280 \times 660)$ µm
Exposure Time	500 ms	–	40 ms
Number of Projections	2500	–	900

4.4. Optical Scan

Optical scans (see sec. 2.3.1) were performed by an external service provider with a Tritop XL photogrammetry system and an ATOS III Triple Scan optical scanner (*Capture 3D*, Santa Ana, USA). The latter device works with structured blue light and features two 8 megapixel cameras and a point spacing of 0.01 mm to 0.61 mm [Capture 3D 2017]. Measurements were carried out without color spraying of the surface, since the material was not smooth enough to achieve a coating of uniform thickness. The complete time for the image acquisition was stated to be around 1 h.

5. Initial Comparison of Imaging Methods

All methodologies used for imaging have their very own strengths and weaknesses. We performed pre-examinations to determine in detail which scan features the best abilities for which part of the blade. The goal of these investigation was to find the most suitable scan methods for the given application. Different scans were necessary in order to find the most suitable parameters with respect to resolution and material penetrability.

5.1. Definition of Regions of Interest

In order to be able to evaluate more adequately the particular benefits and allow improved segmentation results, we split our blade into four different regions of interest (ROIs) for independent analysis. They were created by taking the original CAD-file as reference. We segmented the lower half as well as the inner surface structure and increased their size by expanding until they covered ca. half of the wall thickness. An analogous procedure with the outer surface and eroding the structure resulted in the outer part ROI. The *modus operandi* was repeated for the upper part of the blade subsequently. The resulting four ROIs are depicted in fig. 5.1.
Due to the manufacturing process, the blade was produced with an additional metal part at its bottom, which was probably used to attach it firmly to the platform during fabrication. As a side effect of using the originally desired CAD-geometry for generation of the ROIs for segmentation, we do not take these deviations into account, which results in more meaningful results. However, we are not able to cover the upper tip of the blade entirely. Since at this point deviations are unlikely and a subsequent surface treatment or machining probable, we can also assume this error to be irrelevant. All four ROIs are characterized in tab. 5.1 and as followed:

1. **Inner Part of Socket:** The inner part of the socket features a comparably simple structure with few features. However, a lot of massive material and great wall thicknesses make it hard for X-ray radiation to penetrate the component. Therefore, we expect severe artifacts for low energy CT in combination with a reduced resolution compared to inner features of the foil. Since optical methods are not capable of capturing the inner structure, we cannot obtain data from them for the inner parts.
2. **Outer Part of Socket:** The outer surface of the socket is by far the most complicated part of the blade. It features irregular shaped parts and undercuts as well as high differences in wall thickness and freeform surfaces. Also, the maximum wall thickness is very high, which makes it again hard for low energetic X-rays to penetrate the walls and capture the geometry. Due to the undercuts with re-entrant angles and partially high gradients of path lengths for the laser beam we expect artifacts or geometric distortions to be likely.
3. **Inner Part of Foil:** The inner part of the foil features a very filigrane structure, which can only be covered appropriately with small focal spots. Therefore, we assume high

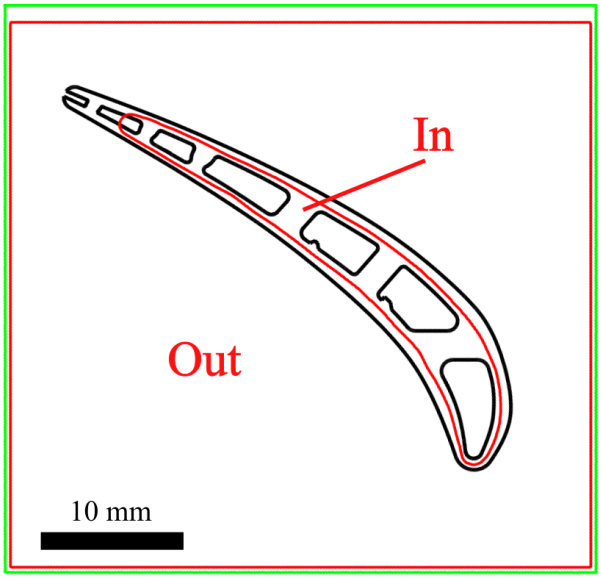

(a) The Outer and Inner Geometry of the Foil

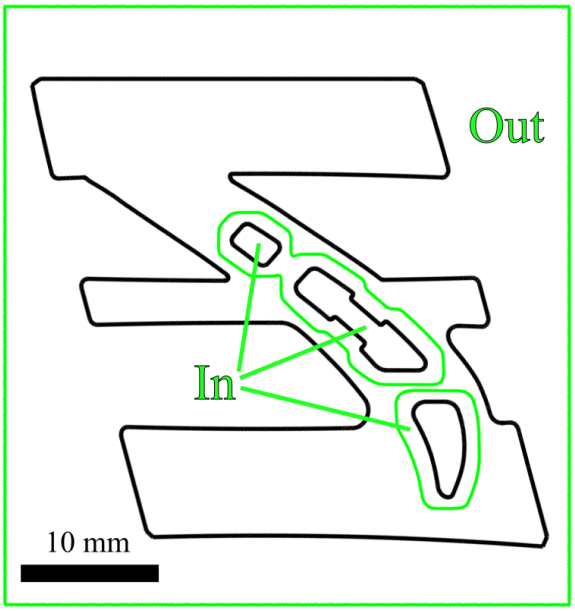

(b) The Outer and Inner Geometry of the Socket

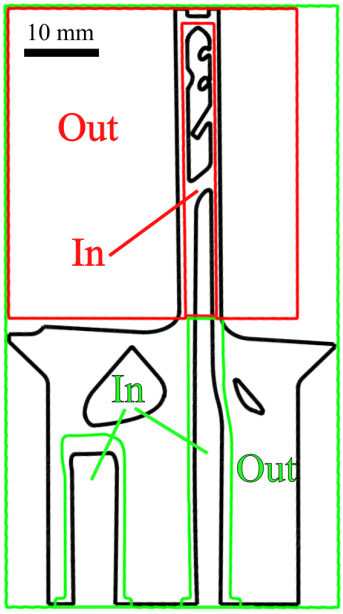

(c) All four ROIs seen from the Side

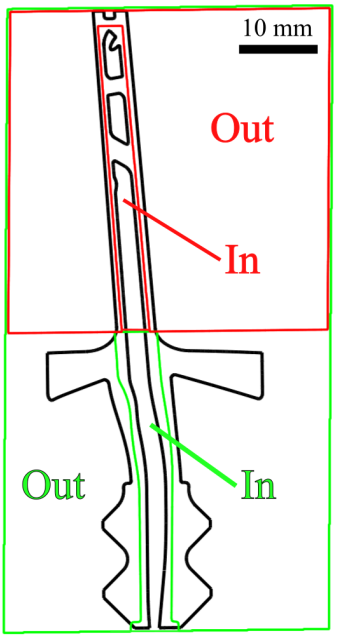

(d) Overview seen from the Front

Figure 5.1.: Location of the four ROIs for our metrologic investigations.

energetic X-rays to lack the accuracy needed in order to cover all details and low energy methods to be superior. Wall thicknesses are small here, so we expect all radiographic methods to provide exploitable data. Again, it is impossible to receive any data from optical measurements.

4. **Outer Part of Foil:** The outer part of the foil features again comparably thin walls. Despite the fact of having a hard to describe freeform surface, its structure is relatively

Table 5.1.: Comparison of respective ROI properties.

	X-ray Penetration Ability	Complexity of Structure
Inner Socket	Low	Low
Outer Socket	Low	High
Inner Foil	High	High
Outer Foil	High	Low

plain and easy to grasp. This part of the blade is supposed to be the one best suited for NDT and metrological analysis.

5.2. Generation of Scan Meshes

The X-ray CT data were viewed and edited via the program VGStudio MAX 3.0 (*Volume Graphics*, Heidelberg, Germany). This software is used for all investigations in this thesis and will be named with its short form VGStudio from now on. After registering the datasets, we segmented the scan data in each of the four ROIs (see sec. 5.1) separately. For this purpose, in each region an appropriate threshold for the grey values was used and the geometry was segmented by use of VGStudio's built-in segmentation algorithm. As contour healing the option "remove particles and all voids" was applied and the edge search distance was chosen individually for best results. We applied no smoothing in order to stay as close to the scan data as possible and do not distort the obtained surface data. The socket of the 225 keV-scan was subdivided in five smaller ROIs (one for each step of the fir-tree root, one for the pockets and one for the side parts of the blade platform) for more accurate results. These were combined in order to yield the surface of the socket part. We ensured that all adjacent ROIs overlapped slightly to make certain to cover the whole dataset and not miss any local features. This way, some voxels were assigned to two or more ROIs. However, we assume the emerged failure as negligible, since the overlaps are only very small.

Subsequently the surfaces of all four ROIs were merged to receive a closed face for the entire blade. Successively it was converted into a mesh by use of standard parameters ("super precise" accuracy of meshing, no simplifications or smoothing) and saved as STL-file. Errors originated by meshing are described in sec. 5.6 and assumed negligible. For all comparisons within this chapter only these final meshes were used. The complete workflow can be found in sec. D.1 in the appendix.

5.3. Determination of Ground Truth

Estimating the accuracy of an optical scanning system is challenging since it depends on many parameters like surface of the object, angular range, light, distance and many more. So far, the only published standard we can rely on is the VDI/VDE 2634 guideline [Eiríksson et al. 2015].

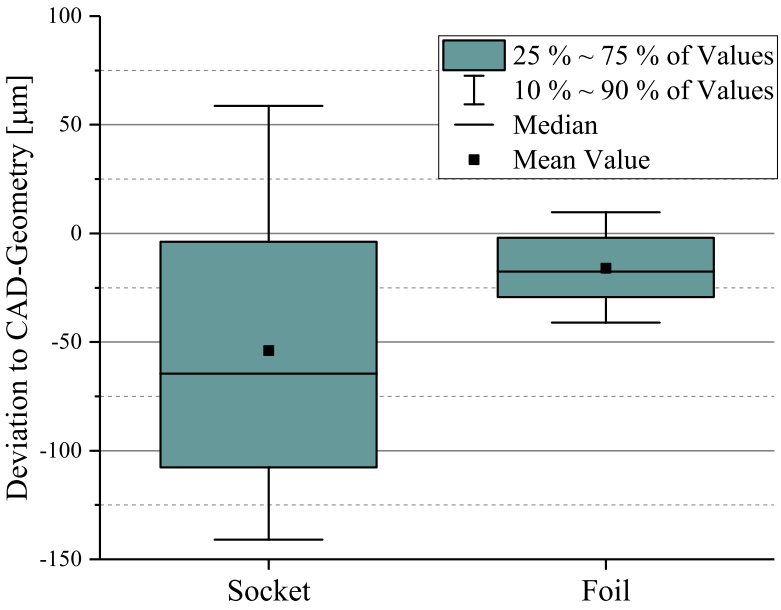

Figure 5.2.: Comparison of the surface obtained by the optical scan with the CAD-model.

For this test, a spherical calibration artifact is captured. Instead of giving an accuracy and a related standard deviation for this scan, four different quality parameters are given:

- **Probing Error Form P_F:** A sphere is least-square fitted by use of the measured points. The P_F describes the radial range of residuals for the fit.
- **Probing Error Shape P_S:** Describes the signed deviation between the nominal object and the least squares fit for the sphere.
- **Sphere Distance Error *SD*** Two different spheres with a fixed distance between each other are separately least square fitted. The difference between both assumed sphere centers is given and compared to the nominal distance; the difference is named *SD*.
- **Flatness *F*:** Analogous to P_S, only with a planar object measured. Describes the range of residuals between a fitted plane and the nominal one.

For each of these values a maximum of 0.3 % of all values (equals ± 3 *SD*) may be rejected. All measurements are performed at up to 10 different pre-defined positions around the object of interest [VDI/VDE-2634 2012]. The manufacturer of the used optical system states its accuracy in a slightly different form using combined values for P_F and P_S. As such, a maximum probing error of 0.002 mm and a maximum distance error of 0.004 mm were given. More detailed information are provided in the acceptance test protocol in the appendix, see sec. C. Even though we cannot assume to reach the same accuracies under normal operation conditions, we expect the optical scan to be significantly better in terms of accuracy and reliability compared to our CT-scans. We want to recall that already the deviations introduced by surface roughness are significantly higher than inaccuracies of the optical scan (see sec. 2.4).

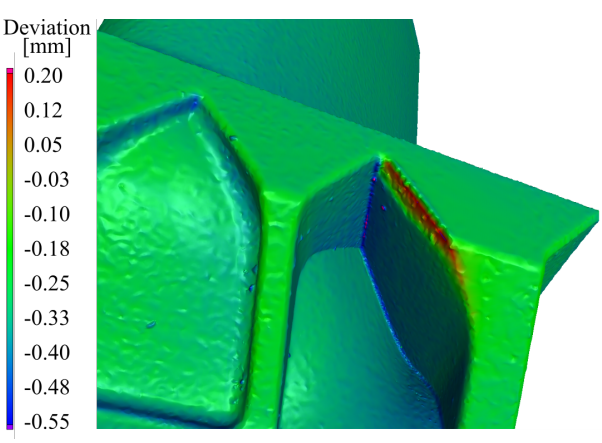

(a) Deviation Analysis by VGStudio

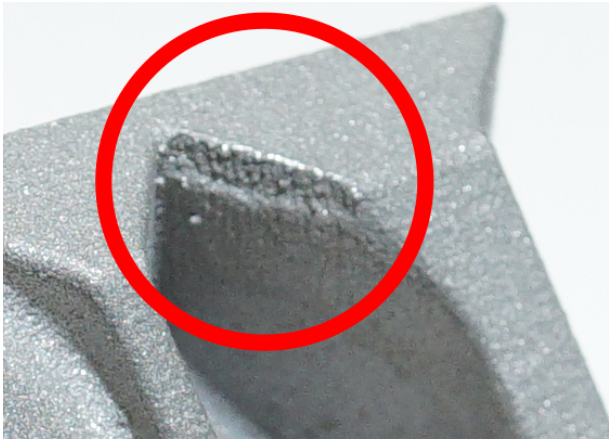

(b) Side Pocket of the Blade

Figure 5.3.: Geometric distortion of the blade due to the manufacturing process. Fig. 5.3a shows the deviation analysis performed by VGStudio on the optical scan. A view at the produced part in fig. 5.3b shows that the indicated distortion is visible in reality as well. Therefore, the optical scan seems to provide more reliable measurements than the supposed CAD-geometry.

We compared the data obtained via optical scan to the geometry provided by CAD. The results are shown in fig. 5.4. The vast part of all deviations are in the negative range (socket: $M = -54\,\mu m$, $SD = 78\,\mu m$, foil: $M = -16\,\mu m$, $SD = 25\,\mu m$), meaning that we have material missing. We expect this kind of error to be more likely for production errors than for such caused by the optical scan, since the structured light scanner would overestimate the amount of material more likely than underestimating it. Also, the highest derivations from the CAD-file are at the chamfers or at the top of the side pockets. Taking a close look at the blade, we can see very clearly that these errors indeed exist (see fig. 5.3). The deviations are also visible in all three CTs (not depicted).

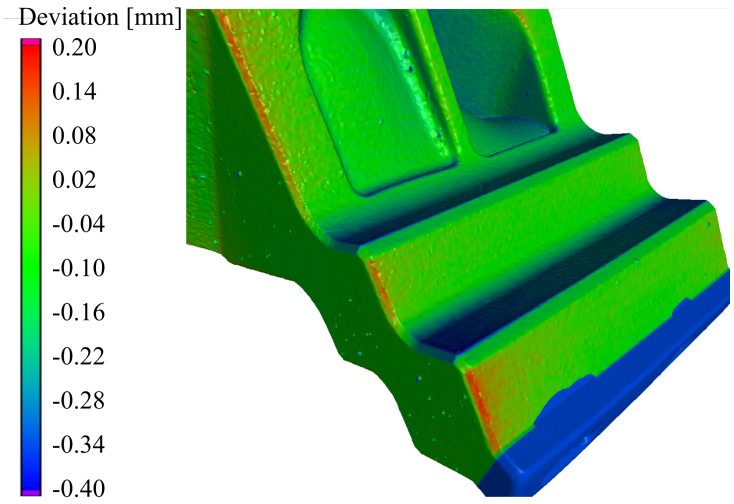

Figure 5.4.: Geometric distortions at the chamfers, seen at the metrological analysis performed with the optical scan. Also, an alternating pattern of too much and too less material is apparent. The additional material (marked blue) poses an attachment that was needed for the production process. It exists at the physical blade, but does not occur in the CAD-file and was not considered for analysis. The thorns and spikes at the surface are also apparent at the physical blade and do not originate from the image acquisition.

Considering all these aspects, we draw the conclusion that using the CAD-geometry as ground truth is not advisable due to errors and deviations caused by the manufacturing process. In contrast, we will use the optical scan data as reference point for further comparisons since we assume them to fit the actual geometry of the part significantly better.

5.4. Suitability Comparison of Computed Tomography Scans

A first view yields great differences between the CT-scans. Like we can see in fig. 5.5, the resolution decreases significantly with increasing acceleration voltage. The features begin to smear out and merge due to the missing contrast. We can hardly distinguish any features at the air outlet of the Linac-scan, so we conclude insufficient suitability of this procedure for our purposes since details might get lost. We also want to point out that in this scan the actual air outlet is not visible anymore at all. In fact, it seems that the blade features a completely closed outer surface.

Fig. 5.5a shows also the typical artifacts originating from insufficient penetrability. These are even better visible if we tend to a part of the blade that is harder to penetrate, e.g. the socket (see fig. 5.6). The low energetic CT suffers from remarkably strong artifacts due to lacking penetration energy. For this area it is barely possible to obtain usable data for any successive steps. According to our first impression, the 450 keV-scan seems to offer an acceptable compromise of penetrability and resolution. We will now approach to characterize the scans by use of more quantitative values.

We used VGStudio's built-in measurement feature to determinate the derivations between the three CT-scans and the optical scan (with the latter as nominal object). The differences were calculated for each of the outer ROIs separately. Since the optical scan is not able to obtain information about the inner structure of the blade, no comparisons were made for these. In order to shorten calculation time, the search range was set manually to 1 mm absolute derivation compared to the nominal scan.

In order to obtain meaningful data, we had to clean them of systematic measurement errors before. The optical scan is not able to resolve the inner structure of the air outlet after the first few µm, so no data are available at this place. Nevertheless, the algorithm tries to compare these nonexistent data with the ones obtained by the CT-scans and finds a considerable error at this spot. We manually removed these incorrect values from the 225 keV and the 450 keV-scan for the upper part of the blade. A correction was not necessary for the linear accelerator scan, since its accuracy was not high enough to resolve the outlet like stated above. Final results are shown in fig. 5.7. Values are given in tab. 5.2. Further details about our value correction protocol are given in sec. A.1.

In case of the 225 keV-scan for the lower part of the blade, our error search distance of 1 mm was considered to be insufficient, since only 65 % of all measuring errors were found in this range.

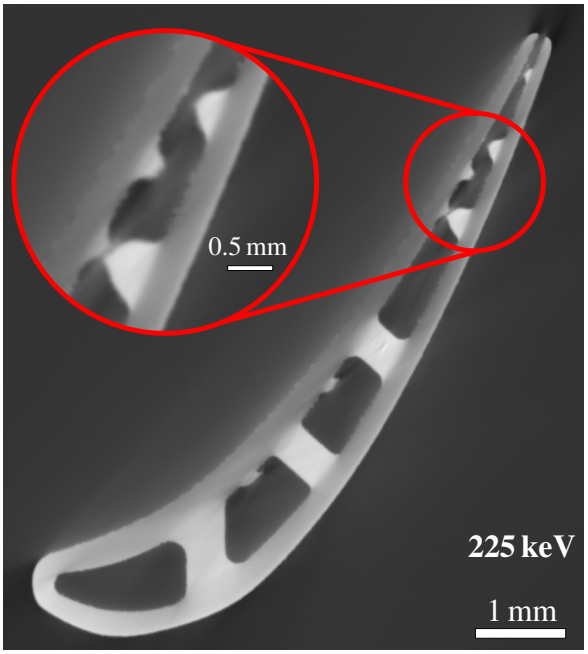

(a) 225 keV-Scan of the Foil

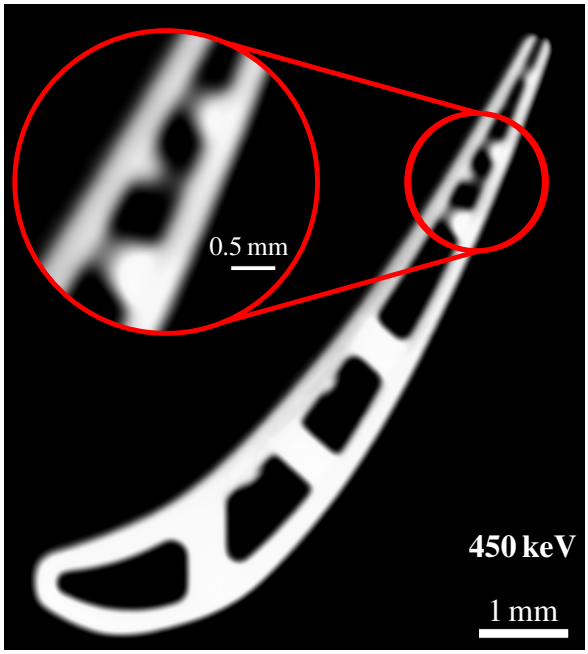

(b) 450 keV-Scan of the Foil

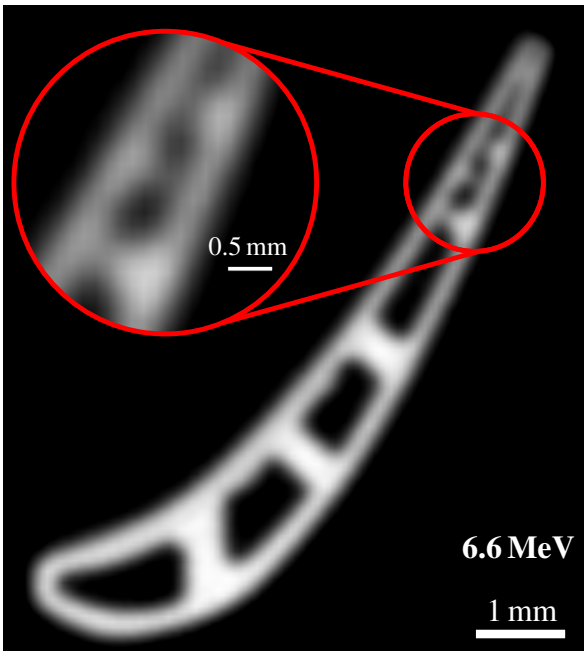

(c) Linac-Scan of the Foil

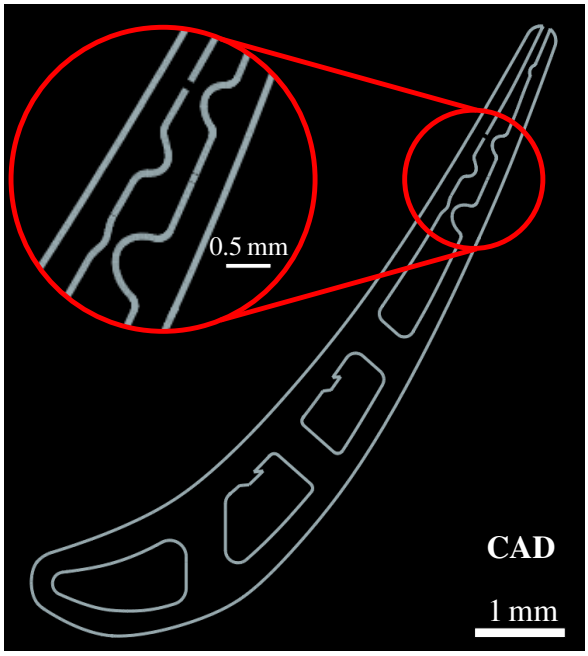

(d) CAD-Geometry of the Foil

Figure 5.5.: Comparison of different CT-scans of the foil. With increasing acceleration voltage, the resolution decreases remarkably. In the Linac-scan, almost no internal feature are distinguishable anymore.

We did not further investigate this case, since inaccuracies to such an extent would anyway exclude any practical application.

We found that all measurements give more accurate information for the upper part of the blade. This is not surprising, since wall thicknesses and penetrability are way better at this ROI. Also, the geometry is considerably simpler, so that severe metrological problems are unlikely to occur. Low X-ray energies are not sufficient to penetrate the socket adequately, so that no exploitable

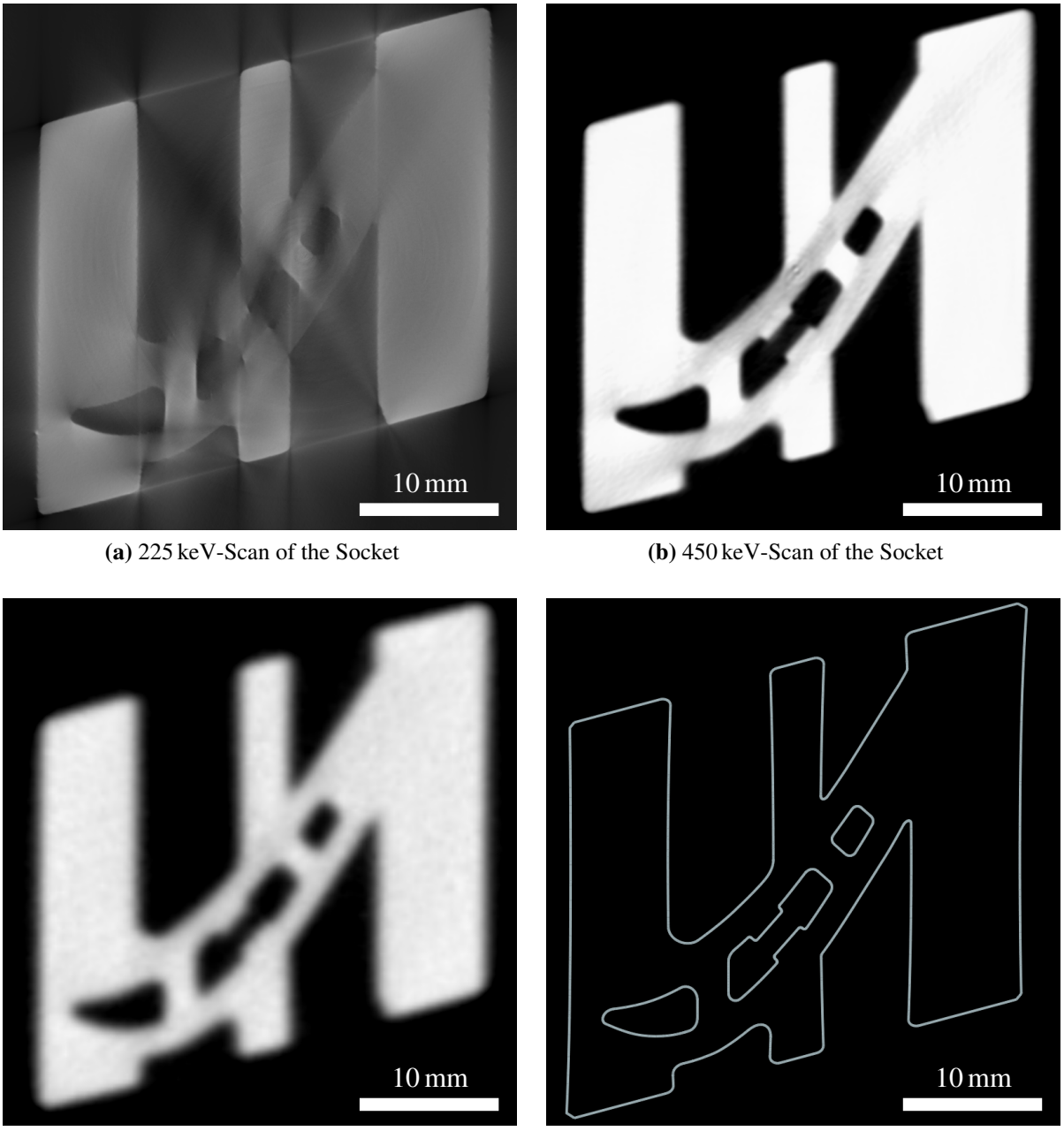

(a) 225 keV-Scan of the Socket

(b) 450 keV-Scan of the Socket

(c) Linac-Scan of the Socket

(d) CAD-Geometry of the Socket

Figure 5.6.: Comparison of CT-scans for the socket part. These slices originate from scan data taken from the platform of the blade. Due to the amount of material, it poses one of the most difficult areas of the object in terms of penetrability.

information can be gathered. Deviations to the ground truth are very widespread and do even surpass 1 mm difference for 35 % of the surface area, which is inacceptable for productive use. The usability of low energy CT is clearly better for upper blade parts, but still its accuracy and precision exceed acceptable dimensions. Nevertheless, our results are still considerably better than the findings of Gameros et al. (2015), who found most deviations for a 220 keV-CT with voxel size 51 µm of the foil of a similar turbine blade to be in the range of −60 µm to 60 µm when compared to a tactile measurement of the same geometry. They found maximum deviations to

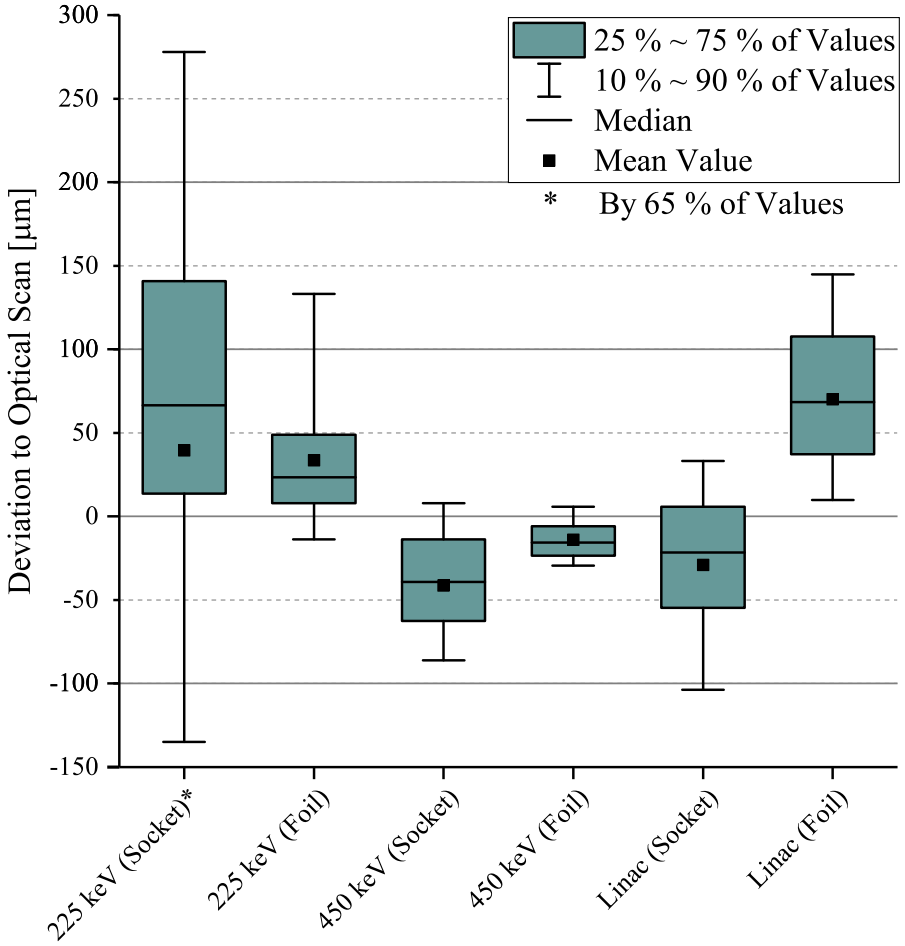

Figure 5.7.: Surface comparisons of different CTs to the optical scan. For the socket part of the 225 keV scan only 65 % of all derivations were found in the considered range of −1 mm to 1 mm. Standard deviation and mean values are given in tab. 5.2.

be −180 µm and +80 µm, whereby only the outer surface was investigated due to the need for accessibility. We suspect two different possible reasons for their deteriorated outcome. First, artifact-afflicted images have been reported, which are mostly caused by insufficient penetrability as well as cone-beam and scatter artifacts. Subsequently, the surface determination was carried out at once for the entire foil, without a choice of appropriately small ROIs that might have been necessary, so that distortions in the mesh are likely. In fact, the greatest deviations have been reported in the same area as the artifacts occurred. Second, the registration was carried out via attached spheres that have been tracked subsequently. Since these were manufactured from a different material for which the acceleration voltage was inappropriately chosen, distortions of these spheres have been reported, which are probably caused by beam hardening. We assume that this might have caused a flawed registration approach and lead to a broader error distribution. Another study of Angel and De Chiffre (2014) found significantly better results, with most deviations in the range of 6 µm to 53 µm and maximum errors of 158 µm. Since their survey involved 27 laboratories from eight different countries, we consider their outcome to be based on a more reliable ground. Their findings are also consistent with our results. Nevertheless, one

need to bear in mind that the comparability of different studies is always challenging, since the scan accuracy of CTs strongly depends on used materials and the workpiece geometry.

Deviations for the medium energy scan are mostly in the negative range, i.e. we underestimate the amount of material at the blade. In fact, the scans show systematically less material at the edges than the other scans do. We assume that this is caused by incorrect settings for the reconstruction that has been performed by the service provider.

Based on our pre-test results in this section, we conclude that CT methods are not suitable for measurement tasks at the outer surface of the blade in order to obtain a precision that can compare with the one of an optical scan. Low energetic X-rays are not able to penetrate the material sufficiently, while Linac high energy scans cannot offer the necessary resolution. As middle ground, the scan with an acceleration voltage of 450 keV gives the best overall results. Nevertheless, accuracy as well as precision are not sufficient for an adequate measurement, so we consider an additional optical scan to be obligatory, since it offers a significantly higher resolution that justifies the effort. As a consequence, we will obtain the surface of the blade from an optical scan as far as possible and use it in order to generate the outer mesh geometry.

Our results are in very good agreement with the findings of Gameros et al. (2015), who performed similar investigations with a 220 keV-CT and an optical scanner for a turbine blade made from Inconel 718. In order to reconstruct the object as accurate as possible they combined the optical scan for the outer part with the CT-scan for the inner geometry, which is exactly the same procedure we intend to use. Nevertheless, their material features better X-ray penetrability that made it possible to capture the whole part with a single scan, whereas our foil requires more sophisticated approaches. We propose possibilities to accomplish an improved scan quality in sections 7 and 8.

5.5. Assessment of Inner Feature Imaging Accuracy

We are going to utilize CT-scans to obtain the inner structure of the blade. Since we already stated in sec. 5.4 that these methods are not well suited for measurements on the outer surface but no other methodology is able to image internal structures, the assessment of their ability to resolve the inside of the blade seems particularly important. Unfortunately, we have no reliable ground truth measurement for the inner surface, since optical scans are not possible due to inaccessibility. Therefore, we will compare the CTs to the CAD-geometry instead (see section 5.5.1). We will try to estimate errors and deviations of the scans to the real workpiece by comparing to errors of surrounding surfaces in sec. 5.5.2. Since we already identified deviations compared to the ideal, desired CAD-geometry, these investigations can only give a rough first impression, since we cannot base our examination on a reliable ground truth. Therefore, we will take a close look at different features within the blade and compare the scan data directly (see sec. 5.5.3).

5.5.1. Comparison to CAD Geometry

Since no reference measurement (e.g. an optical scan) is available, we compared our CT-scans to the geometry provided by the CAD-file analogous to sec. 5.4. For this, we compared deviations in both inner ROIs separately (see e.g. tab. 5.1). A systematic error correction was obsolete since the CAD-geometry is perfect in the considered ROI. For our investigations we used an error search distance of 2 mm, which was sufficient to cover all deviations. Our comparison introduces an additional error, since differences in the shape of the turbine blade due to the production process are not known, so that we compare to a mesh that does not reflect the actual geometry. Results are shown in fig. 5.8 and tab. 5.2, respectively.

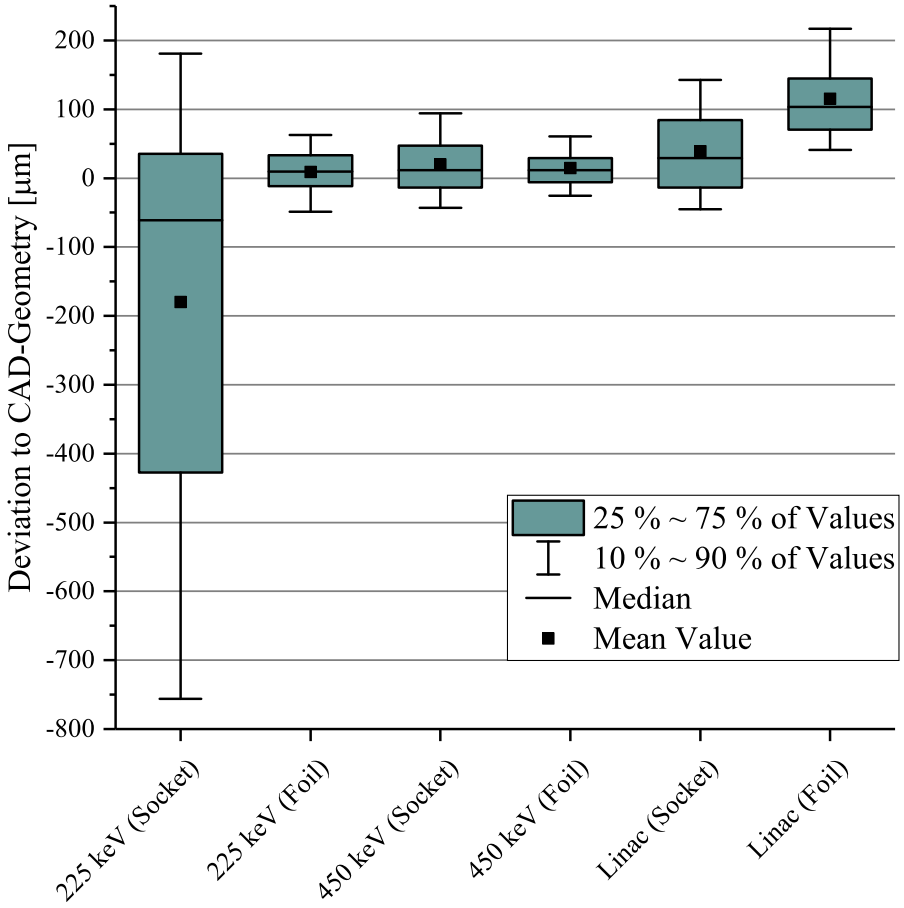

Figure 5.8.: Comparison of the inner structures resolved by different CT-scans to the CAD-geometry. Standard deviation and mean values are given in tab. 5.2.

Our calculations suggest that the 225 keV-scan is again unsuited for any metrologic tasks. This is caused by the lack of penetrability of the thick socket walls and the demanding material properties, which leads to strong artifacts in the reconstructed volume. We expected this outcome since comparisons of the outer surface already revealed similar problems (see sec. 5.4).
The low resolution of the Linac scans lead to broader distributions compared to the other scans (except the 225 keV-scan of the socket), which is caused by the relatively diminished resolution. All scans – excluding the 225 keV-scan of the socket – show a tendency to overestimate the

Table 5.2.: Mean values *M* and standard deviation *SD* of the comparisons in fig. 5.7 and 5.8. Gray fields indicate comparisons with the inner geometry, others with the outer surface.
***calculation carried out by 65 % of values (see sec. 5.4)**

		Nominal Object	
		CAD-Geometry	Optical Scan
Socket	Optical Scan	$M = 54\,\mu m$, $SD = 78\,\mu m$	–
	225 keV	$M = -180\,\mu m$, $SD = 378\,\mu m$	$M^* = 40\,\mu m$, $SD^* = 287\,\mu m$
	450 keV	$M = 20\,\mu m$, $SD = 57\,\mu m$	$M = -41\,\mu m$, $SD = 52\,\mu m$
	6.6 MeV (Linac)	$M = 39\,\mu m$, $SD = 75\,\mu m$	$M = -29\,\mu m$, $SD = 62\,\mu m$
Foil	Optical Scan	$M = 16\,\mu m$, $SD = 25\,\mu m$	–
	225 keV	$M = 9\,\mu m$, $SD = 59\,\mu m$	$M = 34\,\mu m$, $SD = 91\,\mu m$
	450 keV	$M = 15\,\mu m$, $SD = 43\,\mu m$	$M = -14\,\mu m$, $SD = 14\,\mu m$
	6.6 MeV (Linac)	$M = 115\,\mu m$, $SD = 76\,\mu m$	$M = 70\,\mu m$, $SD = 61\,\mu m$

amount of material available (i.e. the mean value is shifted to positive numbers). This is easily graspable if we assume that in fact more material is deposited during the production process for inner features. Both, the medium energy CT and the low energy foil scan, exhibit similar narrow distributions, which are all close to the ideal geometry. The 450 keV-scan of the lower part features a slightly broader distribution, which is probably caused by decreased penetrability of the socket compared to the foil. We conclude that these three methods are the ones best suited to determine the inner geometry precisely. For the socket part only the 450 keV-scan offers sufficient data, whereas low and medium energy CTs can resolve and penetrate the foil satisfactorily.

5.5.2. Error Estimation

Due to the lack of a reliable ground truth, we compared the results of CT-scans of the inner surface with the CAD-geometry in sec. 5.5.1. Now we will try to estimate the occurring error by this procedure. For this, we only consider the foil and take a closer look at both sides of it. We defined a ROI for each side and compared the deviations of the outer surface with the optical scan separately. We expect the concave side to exhibit a significantly worse fit to the optical scan due to a longer pathway, which leads to an insufficient material penetration (see fig. 5.9 and sec. 2.2.7). The results of our investigation are shown in fig. 5.10 and tab. 5.3. Essentially, the data show considerably worse accuracies for the concave foil side. We do not know how exact the data in between both extrema fit the actual geometry, but we can assume that the mistake will be in between, since the inner structure is located approximately half-way. In fig. 5.9 we see also that the connection structure between the concave and convex side appears brighter and smoother than both sides. This is a hint for the remarkably different penetration length, which leads to a weaker signal (i.e. lower grey values) as well as a higher influence of SNR and artifacts.

Unfortunately, this estimation is not possible for the socket area, since the part is approximately axially symmetrical at this place. Nevertheless, we assume that the error occurring there is

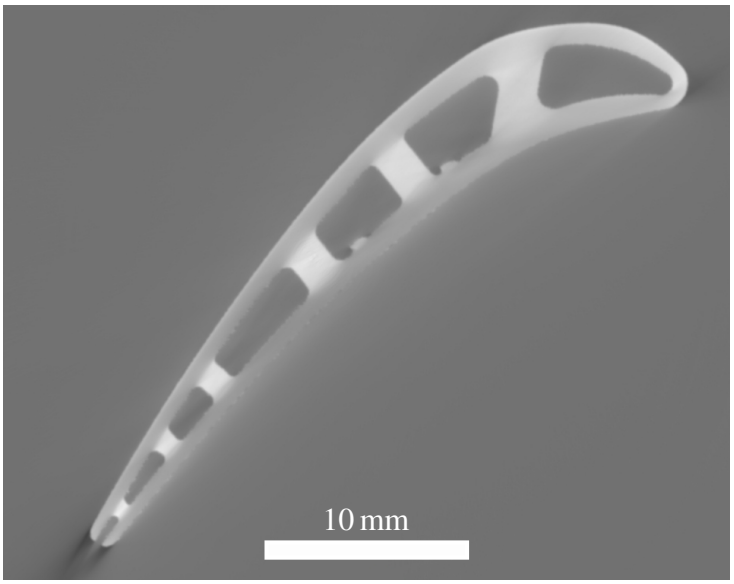

Figure 5.9.: Visual comparison of the concave and convex side of the foil. We can see clearly that the convex side has an easier to determine and more clearly visible edge than the convex one, which is caused by improved contrast. We expect the contrast of the interior to be in between both extrema.

Table 5.3.: Mean values and standard deviation for the values given in fig. 5.10.

	Mean (M)	Standard Deviation (SD)
225 keV (Concave)	49 µm	90 µm
225 keV (Convex)	21 µm	14 µm
450 keV (Concave)	−10 µm	14 µm
225 keV (Convex)	−20 µm	11 µm
Linac (Concave)	80 µm	58 µm
Linac (Convex)	70 µm	49 µm

at least as high as the errors given in fig. 5.10 and 5.7, since the penetrability is significantly worsened. However, since the socket does not feature as filigrane and small structures as the foil does, this is not expected to pose a greater problem.

We already stated in sec. 2.4 that the standard error of inner features produced via SLM is approx. 5 % of the target size, derived from a comparably simple structure. Assuming a typical feature dimension of ca. 0.5 mm we can assume a production standard error of approximately 25 µm. Other calculations given in the literature state a roughly comparable tolerance of 37 µm [Gameros et al. 2015]. This is approximately in the range of the achievable accuracy of our CT-scans (see fig. 5.10). A more detailed evaluation of literature values concerning the manufacturing accuracy of SLM-parts can be found at the end of sec. 6.

5.5.3. Comparison of Features

While the statistical analysis in sec. 5.5.1 refers more to a general test of fidelity concerning our scans, we also need to compare the given features in detail. The graph depicted in fig. 5.8 is supposed to pose more a rough estimation of inner feature accuracy and X-ray penetrability than

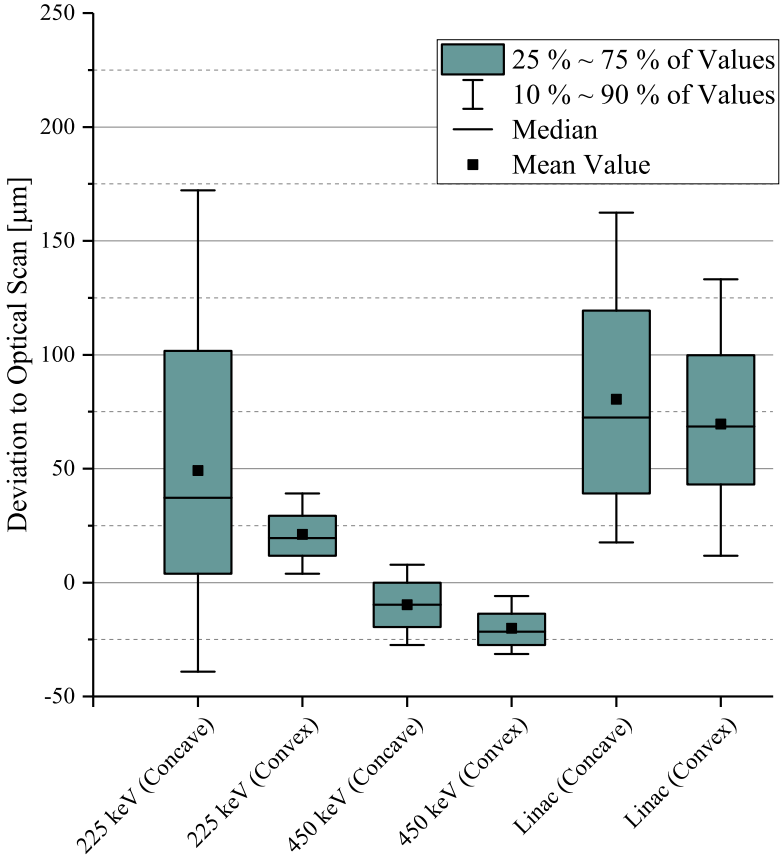

Figure 5.10.: Comparison of convex and concave sides of the foil with the optical scan as reference.

a reliable characteristic value. One needs to keep in mind as well that these values are flawed by artifacts and the actual geometry differs from the CAD-file it was compared to. In order to rely not just on these data, we are going to take a closer look at the filigrane structure at the inner surface of the blade, which is considered to be the most demanding ROI in terms of imaging precision.

Figure 5.11 shows exemplarily a detail of the inner blade. The inner region of the blade is headed left; shown is a small concave cooling rib of the pin cooling system (see fig. 4.1), approximately 0.5 mm in size. Figures 5.11b to 5.11d show extracted meshes generated by iso-50 % approach. Due to the bad and artifact-afflicted scan quality, the 225 keV-scan features a very rough surface appearease (fig. 5.11b). We can see clearly that the low energy scan in fig. 5.11b features a superior, though artifact-afflicted surface quality and resolution. The slight shift of the detail compared to the CAD geometry can be explained by insufficient registration. The 450 keV-CT is very close to the CAD, but lacks details: the concavity on the upper part of the rip is not visible anymore. In return, the outer surface of the blade and also the smooth surfaces are represented considerably better. Compared to both scans, the high energy CT features a clearly worsened resolution. The amount of material is overestimated and the detail is barely visible anymore. Note that this is also reflected by fig. 5.2, where the Linac scan showed a significantly worse outcome related to fidelity.

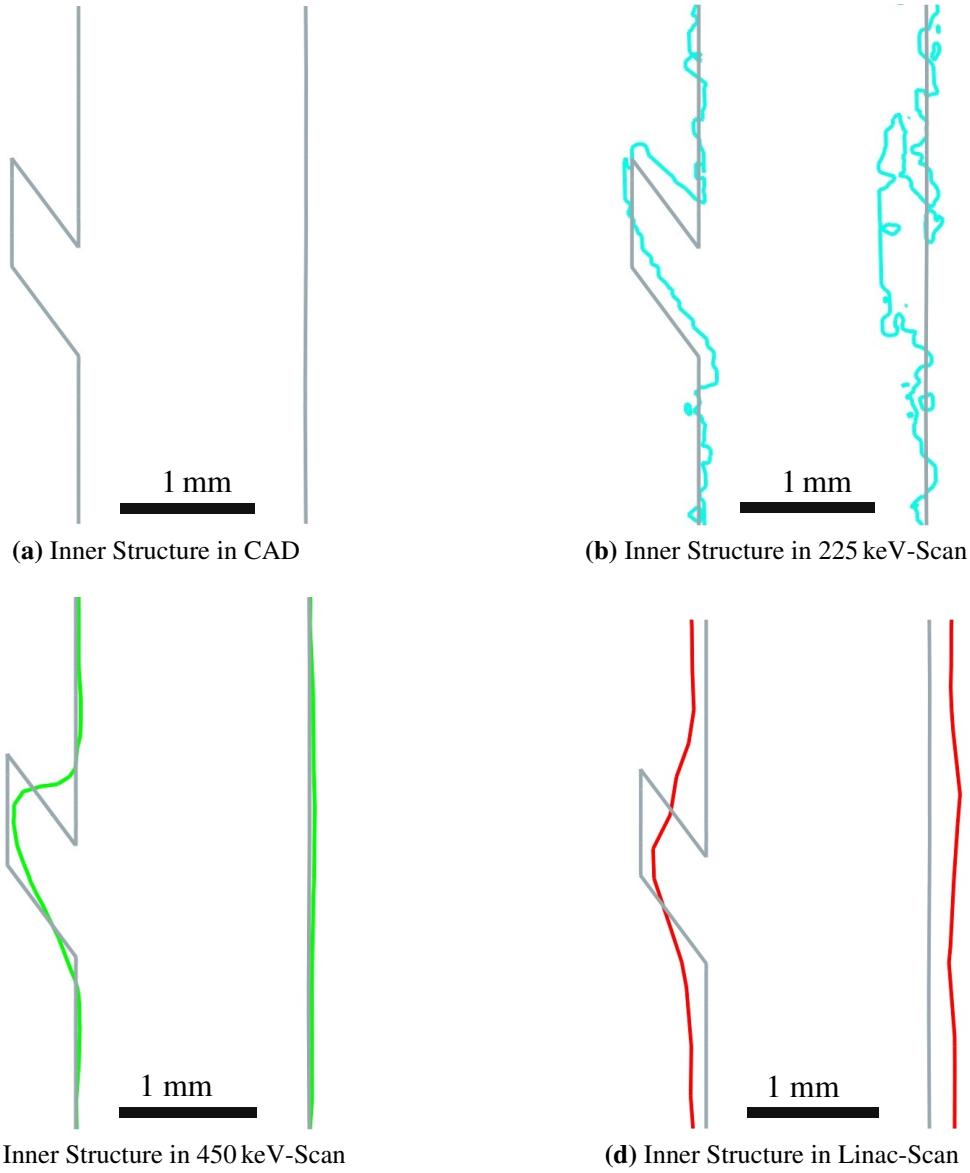

(a) Inner Structure in CAD

(b) Inner Structure in 225 keV-Scan

(c) Inner Structure in 450 keV-Scan

(d) Inner Structure in Linac-Scan

Figure 5.11.: Comparison of inner features in different scans. The blade comes with a concave rip, which is shown in fig. 5.11a. The concavity can only be resolved by the low energetic CT (fig. 5.11b), while the resolution degrades with increasing acceleration voltage in figures 5.11c and 5.11d. The slight geometry shift in fig. 5.11b can be explained by insufficient registration, which does not affect the overall suitability.

5.6. Loss of Accuracy due to Meshing

Despite being the standard format for meshes, STL-files comprise a multitude of drawbacks. Among other disadvantages, they feature redundant information that leads to increased filesize, insufficient program automation and often inconsistent implementations in common CAD-software packages. Already in 1995, Jamieson and Hacker (1995) suggested methods for AM to skip the generation of a STL-file by slicing a CAD-geometry directly in order to overcome problems with this file format and achieve better accuracy. Further disadvantages hold meshing problems like gaps, overlaps or mixed normals and especially a loss of precision caused by approximation errors. A more detailed contemplation can be found for instance in Ma et al. (2001)

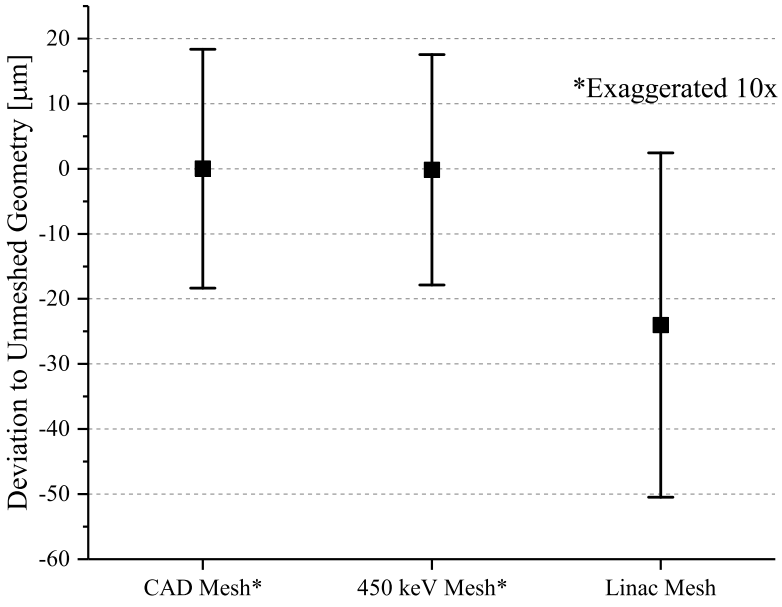

Figure 5.12.: Comparison of meshed to original geometry. Values are exaggerated by factor 10 for the CAD and the 450 keV scan, respectively.

or Lee and Woo (2000). Nevertheless, we use STL-files for our approaches in order to achieve high degrees of transferability and compatibility. Therefore, taking a closer look at possible inaccuracies introduced by meshing seems to be reasonable. This is particularly important since we are dealing with artifact afflicted data, which are known to decrease the mesh quality significantly.

In order to estimate the error caused by meshing the CT volume into a STL-dataset, we compared the CAD-model of the blade with a mesh we derived from it by use of standard accuracy parameters (”super precise”). We found that the loss of accuracy is negligible in comparison to such introduced by other sources (mean difference from CAD for the whole object $M = 0.0\,\mu m$, standard deviation $SD = 1.8\,\mu m$). Anyhow, a CAD-file features per definition perfect surfaces and can be easily described mathematically due to its ideal geometry for meshing. Hence we compared meshes obtained from the Linac scan ($M = -24.0\,\mu m$, $SD = 26.5\,\mu m$) and the 450 keV-scan ($M = 0.2\,\mu m$, $SD = 1.8\,\mu m$) as well. All considered distributions were approximately Gaussian-shaped and are therefore depicted as scatterplot in fig. 5.12. We received the optical scan data as already meshed STL-file, so no original data are available for comparison. The 225 keV-scan features too severe artifacts to reasonably cast an analysis for the entire geometry. The distribution of the Linac-scan is significantly broader than the ones derived from CAD and 450 keV-scan; this might be caused by the poor resolution of the scan, which results in considerably less geometric elements for the mesh (i.e. ca. factor 10 less than for other scans) and leads to a significantly decreased fidelity. Nevertheless, the first two considered meshes are by far more accurate than other sources of deviation. Therefore, we will neglect the slight inaccuracy introduced by them, since the meshes we are primarily dealing with are comparably precise anyway. Nonetheless, one should keep in mind that the meshing process itself can introduce

additional and even significant inaccuracies that might need to be considered, especially for such ones that originate from low resolution scans. Gameros et al. (2015) performed similar comparisons that resulted in a deviation of ±50 µm with maximum deviations at 250 µm. The errors were also found to be non-uniformly distributed over the entire surface area, but formed especially high deviations at the leading edge. However, since we do not possess any additional information about their meshing algorithm we cannot compare these values directly to ours. We conclude with stating that mesh generation itself is indeed a process that is able to introduce noticeable deviations into the RE procedure, but seems to be mostly irrelevant for the majority of applications when compared to other error sources.

6. Assessment of Production Accuracy

In the course of this thesis two blades – blade I and blade II – have been produced by use of AM. The only difference was the slice thickness during production, which has been set to 20 µm for the first and 40 µm for the latter one (see sec. 4.1). Even though first considerations according the precision of manufacturing have been made in sec. 5, we want to investigate the parts in detail in this section.

Generally, it is not very meaningful to determine the overall production accuracy; instead it seems better to do so for several features or parts of the workpiece separately. For instance, Shah et al. (2016) compared several AM methods in terms of production accuracy with CT. For this, an artifact with several features was used and for each feature the accuracy was determined separately by different segmentation algorithms as well as CMM for comparison. However, such an analysis is very time consuming and we do not have the clearly defined features of an artifact. Also, for the inner features there is still no geometry available to compare with. Because of that, we desire to calculate the overall production accuracies each of the four ROIs defined in sec. 5.1 separately. This is not ideal and highly simplified, but gives us plain values that are easy to handle and allow a rough impression of the manufacturing accuracy for each ROI.

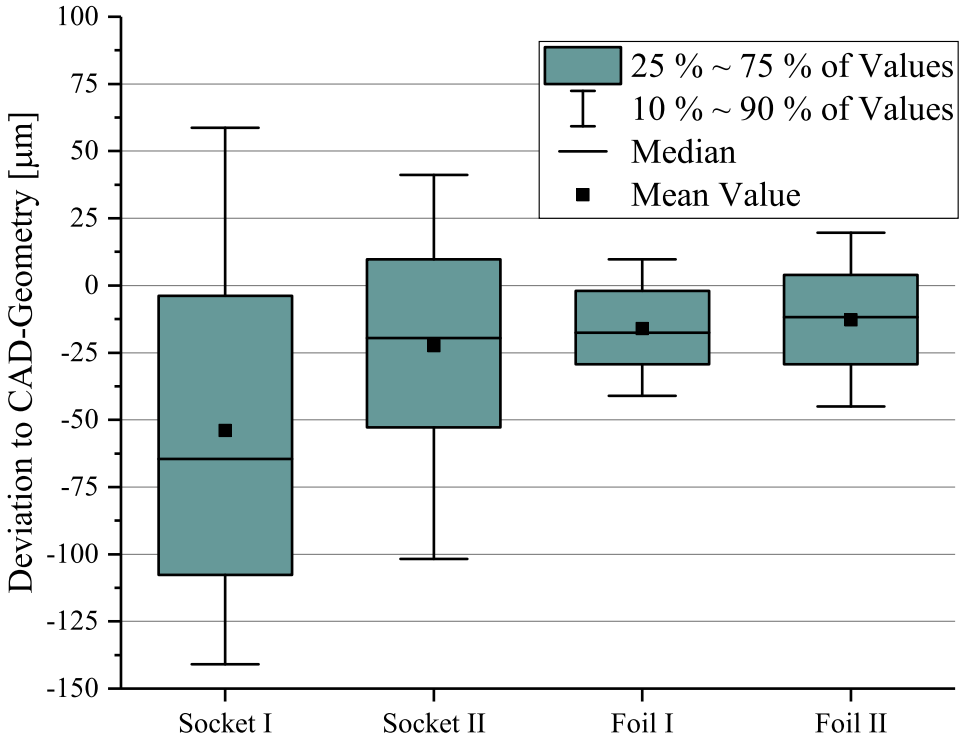

Figure 6.1.: Deviations of both optical scans compared with the CAD-geometry. Mean values and standard deviations are shown in fig. 6.1. Values for blade I are also shown in tab. 5.2.

We start by a first assessment of the outside geometry of both parts. This step has already been performed for the inner geometries of blade I in sec. 5.4 and for the outer geometry in sec. 5.3; therefore performing these comparisons again is obsolete. Nevertheless, we included

Table 6.1.: Mean values and standard deviation for the values given in fig. 6.1.

	Mean (M)	Standard Deviation (SD)
Socket I	−54.0 µm	78.1 µm
Socket II	−22.4 µm	64.9 µm
Foil I	−16.0 µm	25.1 µm
Foil II	−12.7 µm	29.0 µm

the results together with new comparisons for blade II in figure 6.1 and tab. 6.1. Surprisingly, we observe that the manufacturing accuracy for the socket of blade II is better than for blade I when comparing the socket part, while the outcome is approximately identical for the foil. All deviations have their mean value in the negative, meaning that less material is deposited than desired. Nevertheless, the overall production accuracy is quite good with mean values for the deviation of less than 60 µm and the 90^{th} percentile at less than 150 µm.

For the sake of completeness, we also provide a comparison of both optical scans against each other in fig. 6.2. The deviations for the socket part are given by mean value $M = 15.3\,\mu\text{m}$ and standard deviation $SD = 40.7\,\mu\text{m}$ for the socket and $M = 2.5\,\mu\text{m}$, $SD = 20.7\,\mu\text{m}$ for the foil region. Since both blades were manufactured by different production parameters, we cannot use these values to determine a general production accuracy for the process.

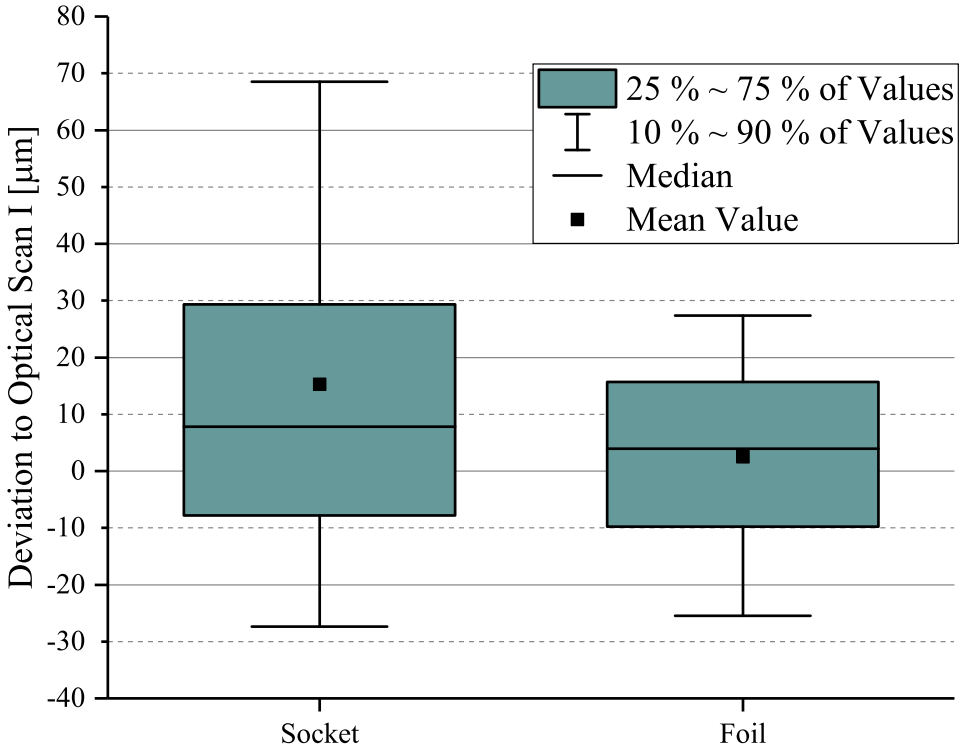

Figure 6.2.: Deviations between both optical scans.

Taking a closer look at the visual comparisons of both blades (depicted in fig. 6.3), we can see clearly that the layer thickness of the AM process influences the outcome significantly. While blade II is comparably flawless with no surface defects or material missing, the build direction

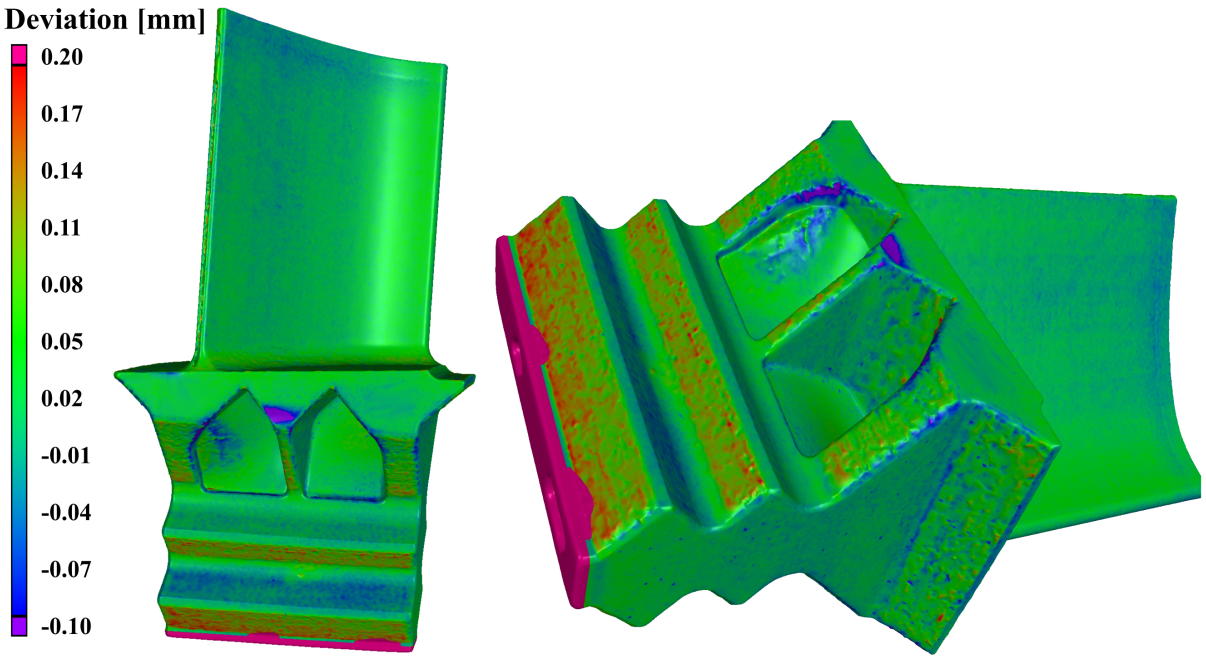

Figure 6.3.: Visual comparison of the optical scan of blade II with blade I (figures not to scale). We can see that the build direction during the AM process influences the shape of the final part to a high degree (build direction is from bottom to top when considering the left image). Platform attachement (indicated in pink) was not considered for further analysis.

is visible instead. For chamfers and parts that are directed to the build platform, we observe a material spillover of more than 100 µm at some spots, while contrary material is missing in approximately the same amount at the opposite site. This is especially visible in the area around the fir-tree root. Also, material is missing around the chamfers, but in a lower degree. This has already been noticed for blade I, but to a smaller extend. Generally, a strong dependence on the build orientation is already well known and counts – among slice thickness, material and further process parameters – to the most important influences in SLM printing [Calignano et al. 2017]. All in all, the surface quality seems to be improved for blade II (no thorns, smoother surface), which might be caused by the experience won concerning the process controlling due to the manufacturing of blade I. Unfortunately, the insufficient slice thickness diminishes this advantage almost entirely.

Since the inner structure of our CT scans is flawed by artifacts (see sec. 5) and we possess neither a high energy scan of blade II nor the possibility to destroy it (see sec. 7 and 8, respectively), we cannot compare the inner structures for manufacturing errors directly. Instead, we used the 450 keV scan of blade I and performed the DECT approach like described in sec. 7. The search distance was set to 1 mm, which is significantly larger than the manufacturing deviations we expect in the inside. This is, due to the fact that the inner deviations are assumed to be at approximately the same level than the outside manufacturing errors we described in fig. 6.1 and 6.2. Because of that, we assume that the influence of the medium energy CT is not dominant for both scans, especially for the one for blade II. The calculated deviations to the CAD geometry

are depicted in fig. 6.4 and tab. 6.2. Deviations of blade II to blade I are depicted in fig. 6.5 for each inner structure separately. We can see that the deviations and defects are larger for the socket part ($M = -33.9\,\mu m$, $SD = 122.0\,\mu m$) than for the foil ($M = -1.9\,\mu m$, $SD = 93.0\,\mu m$). This is not surprising, since fig. 6.4 also showed deviations to the CAD geometry for the outer socket part of blade II. For the foil these deviations are noticeable smaller. All in all, the deviations of the inner blade are approximately in the same scale as the ones on the outside, like already expected.

The outcome is comparable with values of the literature. For instance, Cooper et al. (2015) found deviations within a range of ca. ±150 µm in an about 10 cm long SLM-printed engine valve of Inconel 718. Their layer thickness was 20 µm, so that a comparison with blade I seems most reasonable. Indeed does blade I feature an even better accuracy, which is likely caused due to the smaller part dimensions and possible improvements in the SLM process that might have taken place in the last two years. Also, measurements for the part of Cooper et al. took place after the part was further assembled and exposed to solution anneal and age hardening heat treatments that are likely to influence the shape. A comparison with the outer structure of the part of this study seems not recommendable to us, since their workpiece was heavily machined on the outside.

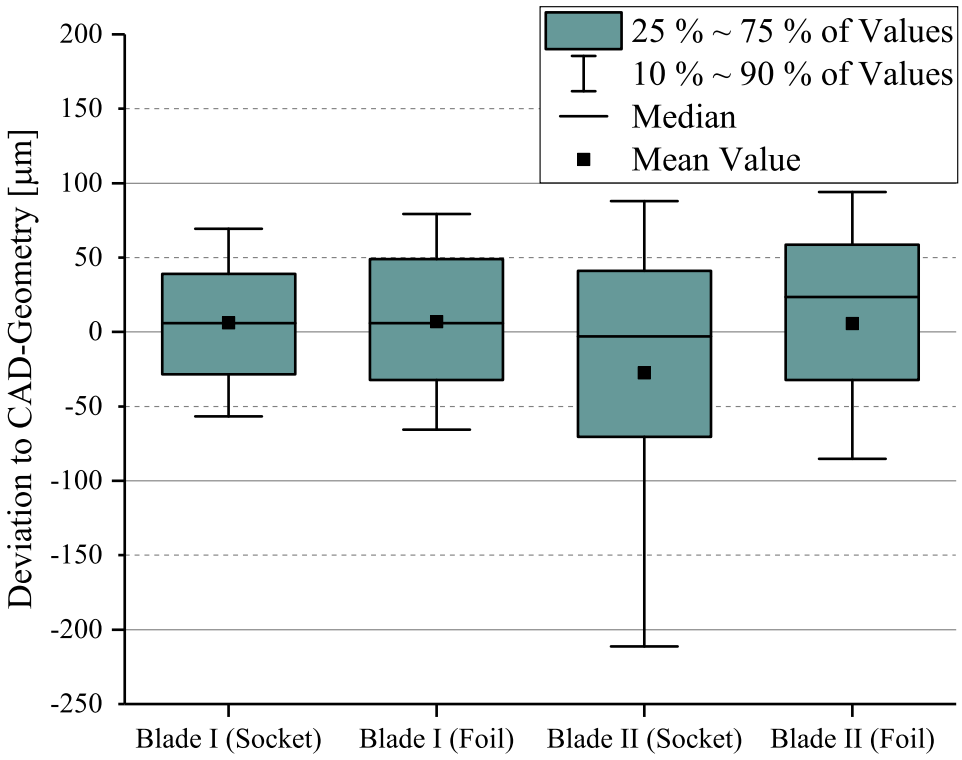

Figure 6.4.: Deviations of both DECT scans, compared to the CAD geometry at the inside of the blades. Values for blade I are also available in fig. 7.3. Values are shown in tab. 6.2.

Probably closest to our application is the analysis of Gameros et al. (2015). They investigated an Inconel 718-manufactured turbine blade of comparable size and CT-parameters to ours and stated a tolerance for internal cooling channels of ca. 37 µm for a nominal diameter of 0.85 mm. Even since this value is close to our findings, one needs to keep in mind that only the diameter of

Table 6.2.: Mean values and standard deviation for the values given in fig. 6.4.

	Mean (*M*)	Standard Deviation (*SD*)
Socket I	6.3 µm	51.8 µm
Socket II	7.0 µm	61.5 µm
Foil I	−27.4 µm	114.0 µm
Foil II	5.7 µm	97.3 µm

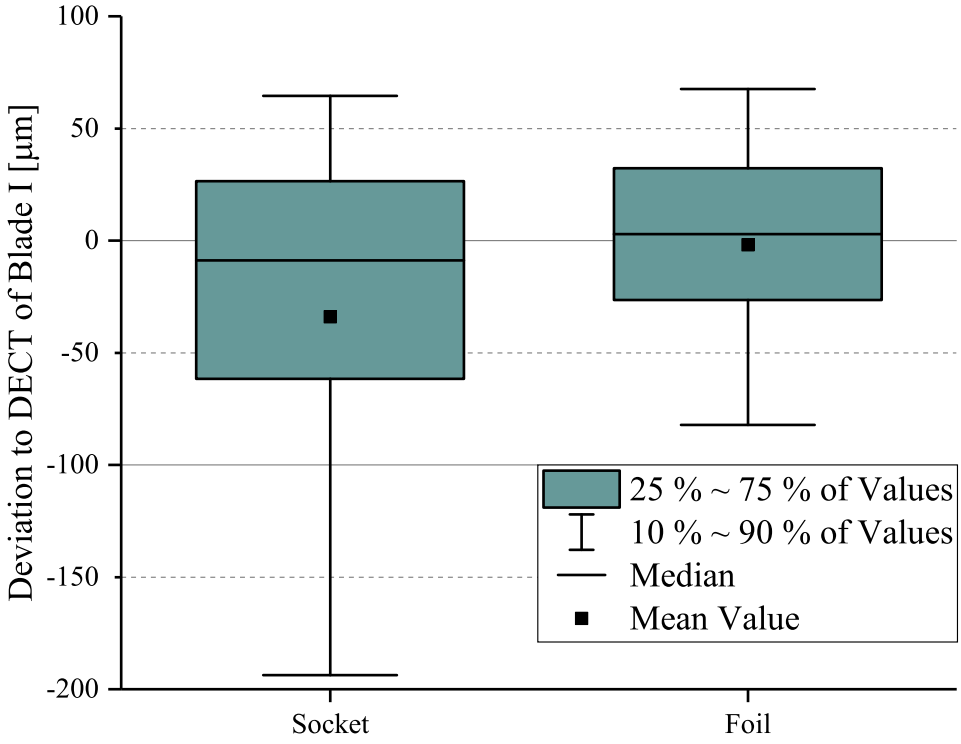

Figure 6.5.: Comparison of the inner structure of blade II to blade I.

cooling channels was considered, whereas we take the whole inner geometry into account, which is assumed to be considerably more complex and explains the higher aberrations we detected. Since no CAD geometry was available, no comparison of the tactile data with the desired shape was possible in this study.

Teeter et al. (2014) built a highly complex test artifact that featured only an outer surface. It was produced via SLM from stainless steel by using a layer thickness of 50 µm. Their investigation resulted in a mean difference of less than 100 µm compared to the desired structure. This value is also roughly comparable to our finding if we take into account that the slice thickness was higher than for blade I and blade II. Nevertheless, a different material was used, so that we cannot take this outcome for exactly comparable. It was also found that the minimum feature size is 300 µm, which is smaller than the minimum size of 400 µm to 500 µm specified by the supplier for our material (see sec. B).

For the alloys Ti6Al4V and CoCrMo, Ben and Jean-Pierre (2007) determined an outside manufacturing accuracy of better than 40 µm. He also performed SLM with a layer thickness of 50 µm. However, his test parts were very small (maximum 40 mm in one dimension) and both alloys are

very different to ours by means of material composition. Roughness values were found between a R_a of 5 µm to 20 µm, which are consistent with other values from the literature [Bremen et al. 2012; Ghani et al. 2017]. These values are relatively high when compared with other manufacturing technologies and should not be neglected.

Finally, Ghani et al. (2017) investigated the accuracy of internal features in an internally cooled cutting tool. They used SLM with a slice thickness of 50 µm and an unknown material, probably a rust-free tool steel. They derived a standard error larger than 5 % compared to the desired dimension and found similar roughness values as Ben and Jean-Pierre (2007). Stating a general desired dimension for our blade is tricky, but if we suppose a rough minimal feature value of around 500 µm and assume a tolerance of three times the standard deviation, we obtain an accuracy of 25 µm, which is way too small. We assume that this discrepancy is caused by the very application-specific value of Ghani et al. (2017), since their geometry was very simple in shape.

7. Approach Based on Dual Energy Computed Tomography

Pre-examinations in sec. 5.5 revealed superior resolution for the low energy microfocus CT, but insufficient penetrating energy to obtain a feasible image, especially for thicker regions of the object. This dilemma is well-known, and several approaches exist in literature to overcome it.

A possibility is to use image fusion techniques that combine the scan data with knowledge from other imaging systems. For instance, Schrapp and Goldammer (2013) used optical scan data to provide additional information for the reconstruction algorithm to restore blurred image areas caused by insufficient X-ray penetration. Unfortunately, the capabilities for this method are limited when it comes to resolve the inner structure. Even with additional data from ultrasound imaging, sufficient improvements for our purpose seem unlikely [Schrapp et al. 2014a].

7.1. Previous Approaches

The literature holds several approaches using dual energy CT, where the object is exposed to at least two radiographic scans with different acceleration voltages for each of them. This so called Dual-Energy Computed Tomography (DECT) can be used to improve recordings of objects that consist of several materials with strong differences in their attenuation coefficients [Philipp and Albert 2010]. DECT systems are known in the field of medicine since the 80s and are still in use today. Since the attenuation coefficients are dependent on the incident X-ray energy (see sec. 2.2.4) several new possibilities emerge. First of all, the considered material can be better distinguished from similar surrounding tissue. This is important, for instance to detect gout at bone tissues. Taking the additional information into account, improved beam hardening algorithms can be used. Bone density, atomic number and electron density can be measured and many other applications are available today as well [Sedlmair 2009, p. 27f].

For metrological purposes, one can use the high penetration abilities of hard radiation to capture the rough structure of a component. A second CT with lower energy is able to achieve a better resolution and sharper edges due to smaller focal spots. The combination of these scans finally yield a dataset with the benefits from both recordings [Heinzl et al. 2007]. For instance, combinations of MeV-scans in combination with low-energetic keV-scans have been used to improve the accuracy and contrast of cargo container scans [Kolkoori et al. 2014; Martz et al. 2016]. In other fields, Yang et al. (2011) used a combination of kilovoltage and megavoltage scans to improve the determination of proton stopping powers in human tissue. For imaging in the field of radiation therapy, DECT has been used to improve image quality for only limited availability of measurement data and to reduce the vulnerability to metal artifacts [Pearson et al. 2015].

7.2. Methods and Results of Dual Energy Scan

Consequently, we started with two CT datasets of different energy for our DECT approach. We chose the 225 keV scan as low energy and the 450 keV scan as the high energy imaging method for reasons outlined in sec. 5.5. We perform a surface extraction for the latter, artifact-free scan like described in sec. 5.1. Subsequently, we tried to determine the surface of the low energetic scan as good as possible to achieve a registration to the high energy dataset. For the surface extraction we advise VGStudio to take the 450 keV surface as starting contour and apply a starting contour healing algorithm that includes the removal of all voids and particles. Furthermore, we arbitrarily chose a search distance of 0.35 mm for our investigations, which we assume to be sufficient to compensate for the differences of both scans. In general, this value has to be defined manually, depending on the shape of the part of interest and its size. In the next step, VGStudio automatically determines the surface with the given parameters and we finally yield the DECT surface model that can be used to extract a STL- or CAD-file. The workflow is shown in fig. 7.1; the detailed pathway specified for VGStudio is depicted in the appendix in sec. D.2. The procedure is also shown in fig. 7.4. The visual inspection of the conventional 225 keV-scan (fig. 7.4b) with the outcome of the DECT data (fig. 7.4d) shows a significant improvement.
We compared the result of our DECT approach with the respective ground truth geometries (i.e. CAD for the inner and optical scan for the outer geometry). Analogous to our results in sec. 5.4, we had to clean the optical scanned foil dataset of systematic errors like explained in sec. A.1. The cleaned region was defined by thresholds of –0.9 mm and –0.4 mm, respectively. Final results are shown in fig. 7.2 and 7.3 as well as in tab. 7.1. The optical comparison is for the sake of completeness only, since we already showed in sec. 5.4 that the optical scan features significantly better resolutions for the outer geometry when compared to CT scans. Our results show that the geometry data obtained by DECT can easily compete with the other CT scans and no loss of overall fidelity is visible.
We also tried to combine the 225 keV and the Linac-scan in a second approach. Due to the poor accuracy of the latter, we were unable to generate good geometries, since even for large search distances no suitable edges were found. The result does not hold any of the smaller features and is generally not better than the pure Linac scan. Therefore, we relinquish this approach and concentrate on both scans with lower energies instead.

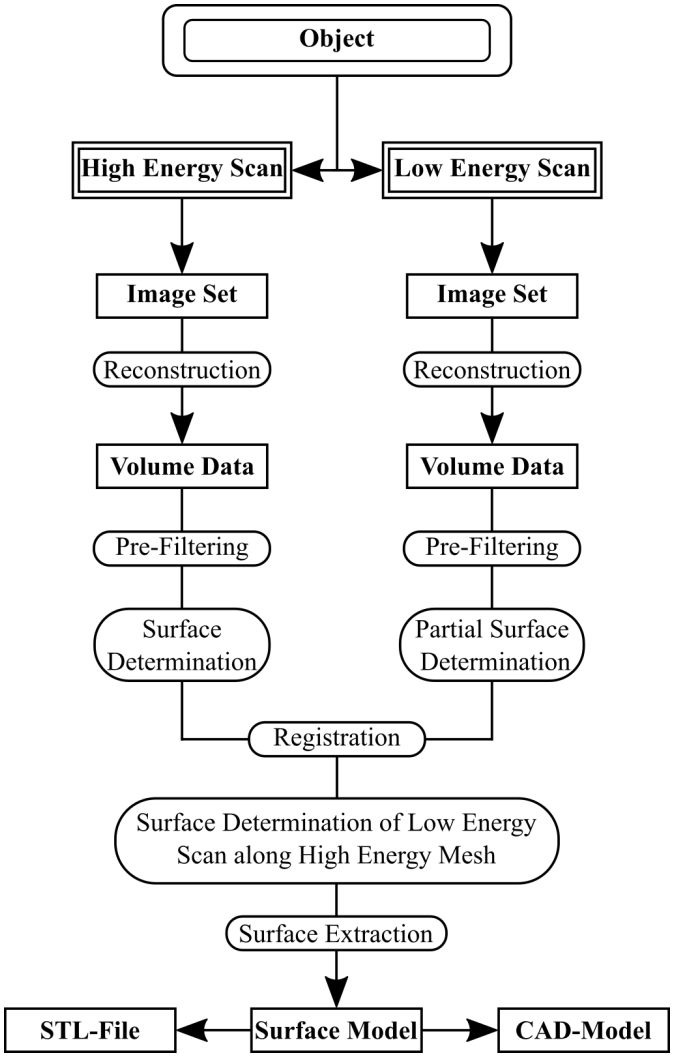

Figure 7.1.: Workflow for our DECT approach. The pre-filtering stage is only to illustrate additional possibilities of this method; no filtering was applied by us at this point. A more detailed pathway for VGStudio can be found in sec. D.2 (adapted from Heinzl et al. (2007)).

Table 7.1.: Mean values and standard deviation for the DECT values given in fig. 7.2 and 7.3. Other values can be found in tab. 5.2.

	Mean (M)	Standard Deviation (SD)
DECT Outer Socket	42.0 µm	50.0 µm
DECT Inner Socket	6.3 µm	51.8 µm
DECT Outer Foil	25.4 µm	33.4 µm
DECT Inner Foil	7.0 µm	61.5 µm

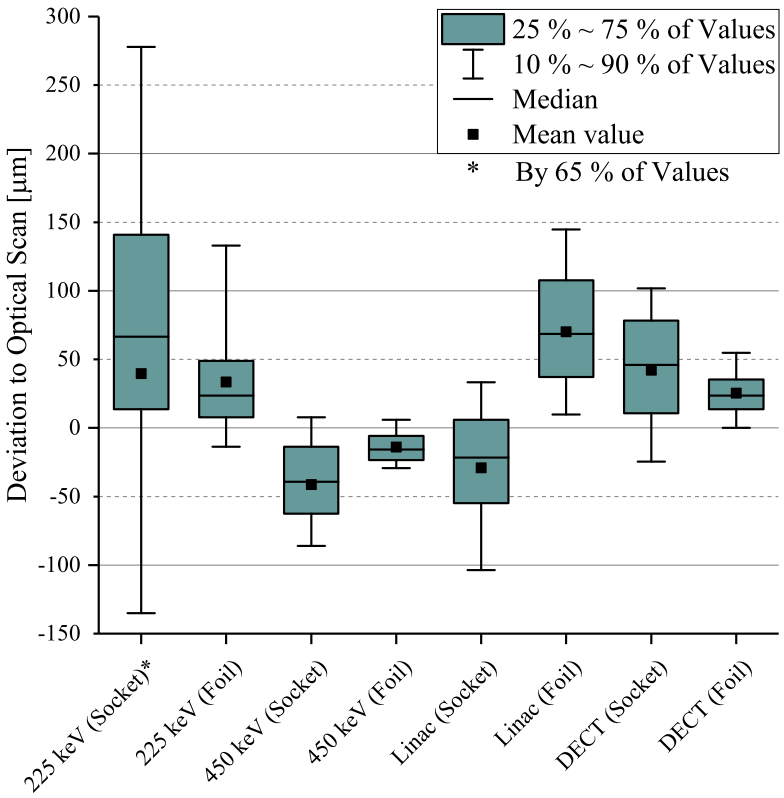

Figure 7.2.: Comparison of the outer geometry of different CT approaches compared to the optical scan. Standard deviation and mean values for DECT are provided in tab. 7.1. Other values are taken from fig. 5.7 and listed in tab. 5.2

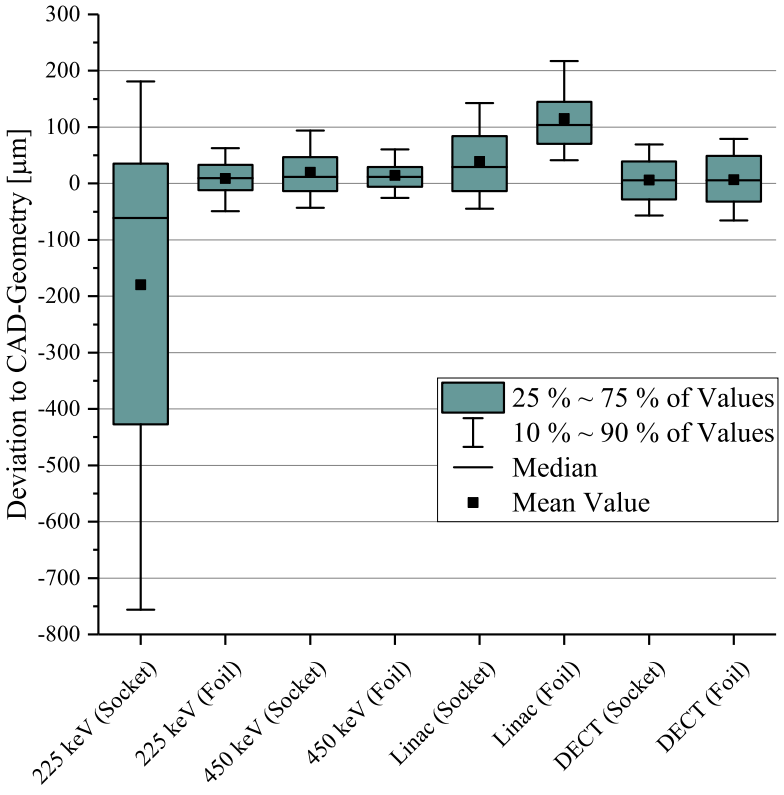

Figure 7.3.: Comparison of the inner geometry of various CT approaches compared to the CAD geometry. Standard deviation and mean values for DECT are provided in tab. 7.1. Other values are taken from fig. 5.8 and listed in tab. 5.2

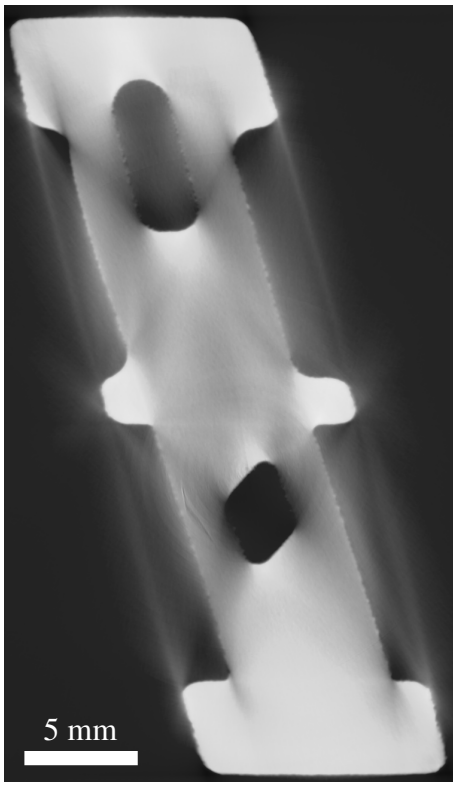

(a) Raw Scan Data From 225 keV-Scan

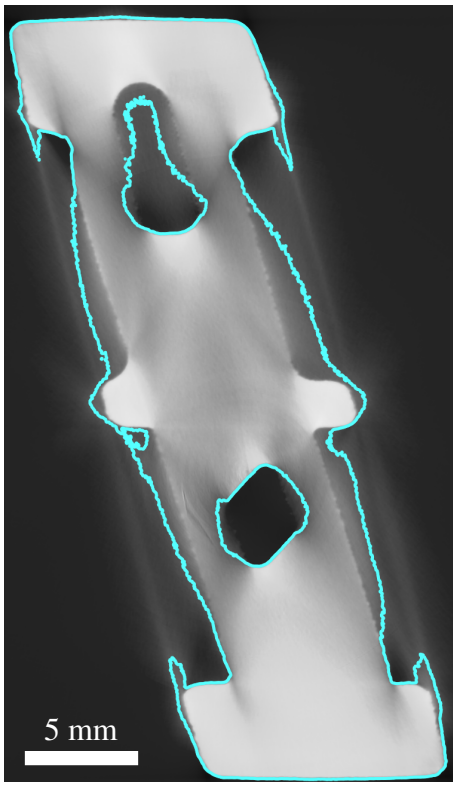

(b) Conventional Segmentation Approach

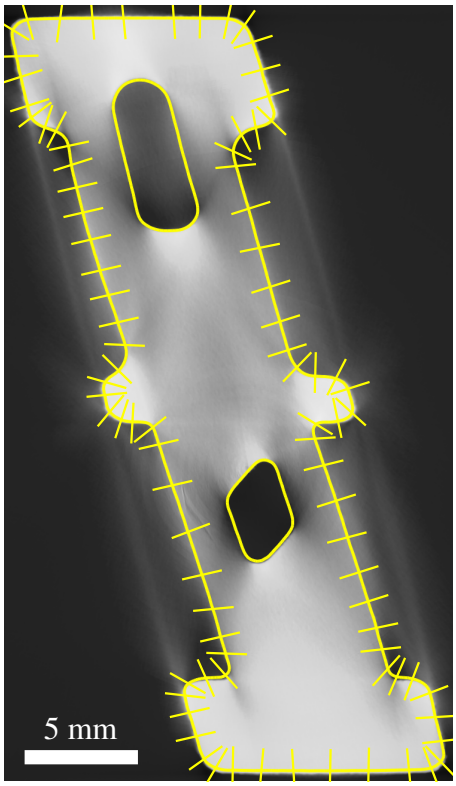

(c) Contour of the 450 keV-Scan With Indicated Search Distance

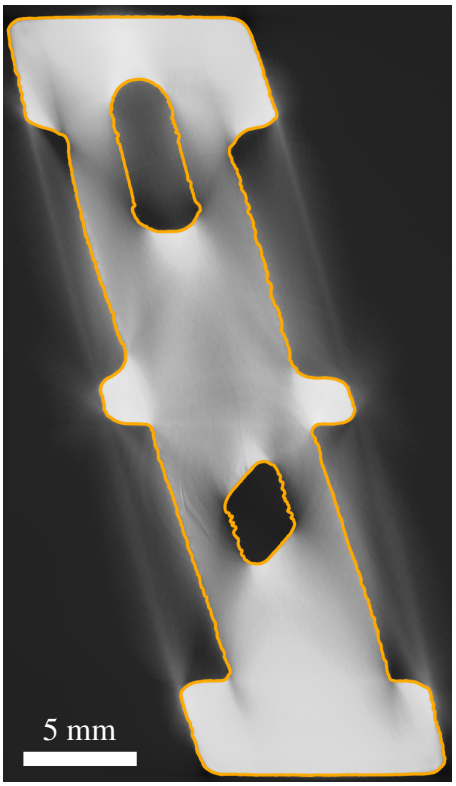

(d) Final Outcome After DECT Surface Extraction

Figure 7.4.: Workflow for our DECT approach and comparison to a conventional 225 keV-scan. Figure 7.4a shows the imaging data of the low energy scan obtained for a part of the socket. A conventional segmentation by threshold would yield fig. 7.4b, which is not suitable for further analysis. A combination with the 450 keV-data (fig. 7.4c) results in the final DECT-surface (fig. 7.4d) that is closer to the actual geometry.

7.3. Robustness of Algorithm

In sec. 7.2 we carried out a segmentation with as good as possible registration beforehand. However, a perfect registration is not a matter of course. Artifacts, wear or local irregularities of the part can lead to a deteriorated orientation. Also, it is possible to use parts of already existent CAD-files as *a priori* knowledge. These can also differ more from the original geometry than we investigated so far. Also, it can be reasonable to use a CAD-file that is not identical to the part but comes close to the desired geometry. Therefore, it seems necessary to review our approach for robustness to incorrect registration or differing CAD-starting-geometries. The 450 keV-scan describes the outer surface of the blade better than the CAD-geometry does. Therefore, we can assume it to fit the inner surface better as well. Based on this consideration we used the 450 keV-scan as contour search geometry for meshing the 225 keV-foil.

We used only the foil for our investigations, since we found the low energy scan inappropriate for the socket part (see sec. 5.4), so that related results would not be representative. Registration and mesh generation was carried out like described in sec. 7. In order to simulate a false registration, we translated the 450 keV-geometry repeatedly for 0.1 mm and performed the same operations. Contour search distance was set to 0.35 mm and contour healing option ”remove particles and all voids” was enabled. Meshes were automatically cleaned of isolated components subsequently (threshold 1 % of entire surface). We did only check initial geometry shifts into one spatial dimension and one direction since we assume the outcome of other directions to be similar and to save computation time. Also, we did not check rotational deviations, since they are locally similar to lateral transitions of changing distance, which can be easily calculated if the angle is known.

Deviations were compared to the mesh generated by the unshifted start geometry. The results are shown in fig. 7.5 and tab. 7.2, respectively. We can see clearly that distortions get larger with increasing distance to a perfect aligned and registered starting contour. This is caused mainly by local aberrations, where, for instance, smaller features get lost. The data reveal as well that the contour finding seems to be robust enough for many applications: even for a shift of 0.3 mm most deviations are smaller than 100 µm, which can be sufficient for larger geometry features. Probably this value is also linked to the chosen search distance, which is also roughly in this scale of value. Shifting with 0.2 mm achieved better results than with other shifting distances, including the previous one with 0.1 mm, which can be caused by a more suitable registration than for the other ones; probably the initial registration was not optimal. Closer investigation of the newly segmented geometry shows also that the algorithm seems to take the search geometry as segmentation geometry if it does not find any features of the 225 keV-scan within its search distance, which results for instance in unusually smooth surfaces (not depicted). This outcome is not surprising, but it emphasizes the importance of a close check of the new geometry after generation, since there is a risk that the search contour is directly overtaken without including

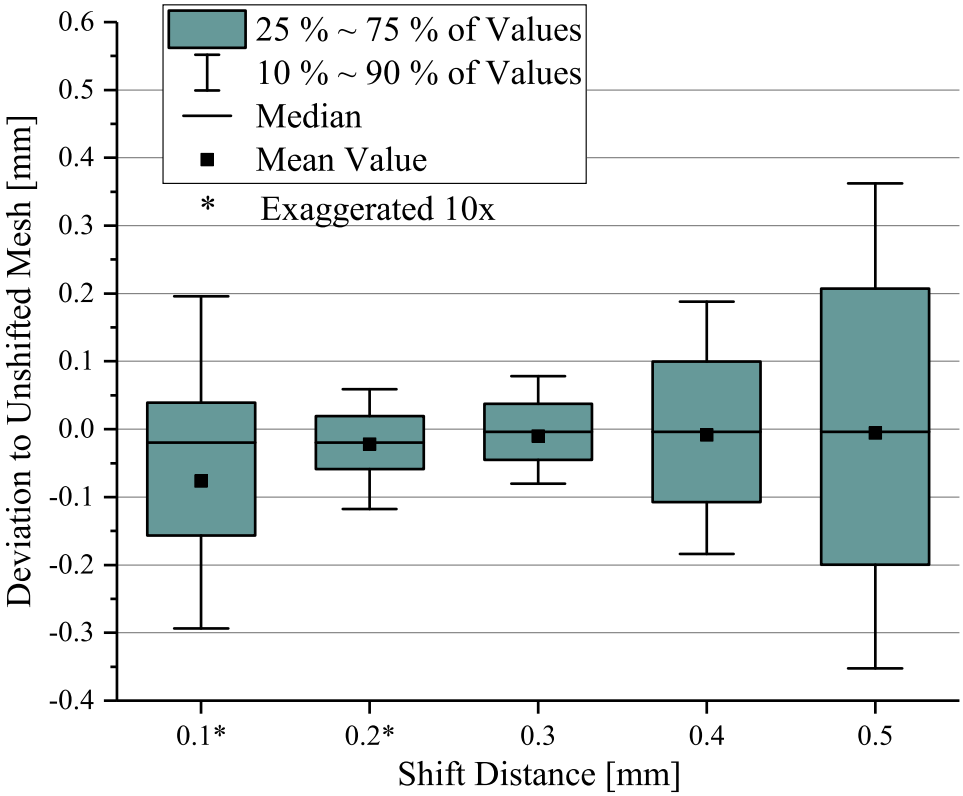

Figure 7.5.: Investigation for robustness concerning geometry shifts. For improved visibility the shifts for 0.1 mm and 0.2 mm are depicted ten times larger than they are. Values are given in tab. 7.2.

Table 7.2.: Mean values and standard deviation for the investigation depicted in fig. 7.5.

Shift Distance	Mean (M)	Standard Deviation (SD)
0.1 mm	−7.6 µm	50.8 µm
0.2 mm	−2.2 µm	17.1 µm
0.3 mm	−9.9 µm	93.3 µm
0.4 mm	−8.6 µm	158.2 µm
0.5 mm	−5.3 µm	256.2 µm

any additional information of the scan that is to segment. Under normal operating conditions this effect is desirable since potential gaps (e.g. such introduced by insufficient data of the 225 keV-scan) are automatically bridged.

We want to stress that this examination is by no means sufficient or even exhaustive to prove absolute stability or fidelity under all circumstances. The investigation given in this section is rather a rough check of robustness and significantly more analysis is necessary for a reliable and airtight statement. Furthermore, we assume the results given in this section to be highly dependent on the chosen search distance.

8. Destructive Testing

One of the simplest possibilities to overcome the problem of penetrability that we encountered, is to reduce the wall thickness of the part of investigation by cutting it in pieces. Considering eq. 2.5 we can see that the measured intensity would increase greatly with a smaller pathway to penetrate. As a matter of course, this procedure cannot be called nondestructive by any means and is therefore only applicable in special cases. For instance, this can be the case if several complete turbines are replaced and the built-in blades are afterwards not needed anymore. Within this section we show that a destructive testing method would be sufficient to undertake proper measurements due to a great reduction of artifacts originating from insufficient penetrability (see also sec. 2.2.7).

Since we cannot afford to destroy the blade at this point, all consideration are based on simulations performed by aRTist. First, we modelled the blade's material in order to yield the attenuation coefficient μ in dependence of the photon energy E. The exact composition as well as the attenuation graph are provided in the appendix in sec. B.1. Usually, slight variations concerning the material composition can be neglected for this kind of investigation [Ehrig et al. 2010]. Next, we used the CAD model in order to create a STL-file for the geometry. In order to investigate the influence of our destructive approach, we also generated two additional files with the geometry cutted 45° and 315° in clockwise direction like depicted in fig. 8.2c and 8.2d. The first one was chosen to split the blade in two approximately equal-sized parts, the latter was an approach to do a more practical cutting, since the way through the foil section was kept as short as possible. We assume the latter attempt to be more practically feasible, since only few details are destroyed by the cutline and the cutting path is minimized to reduce the necessary handling time.

Also, we are unable to model all possible influences in its entirety. Because of that, we undertook a parameter optimization until we obtained slices for the full part of similar appearance than we got in the real CT. Such a slice is exemplarily shown in fig. 8.2a. Tab. 8.1 provides the parameters needed for the simulations. We used the same values to undertake a CT simulation of

Table 8.1.: Simulation parameters for the destructive testing approach.

Acceleration Voltage	140 keV
Source Material	1 mm Diamond + 5.5 µm Tungsten
Focal Spot Size	Point Source
Filter	1 mm Copper
SOD	195 mm
SDD	780 mm
Magnification	4.00
Voxel Size	50 µm
Number of Projections for Scan	1500

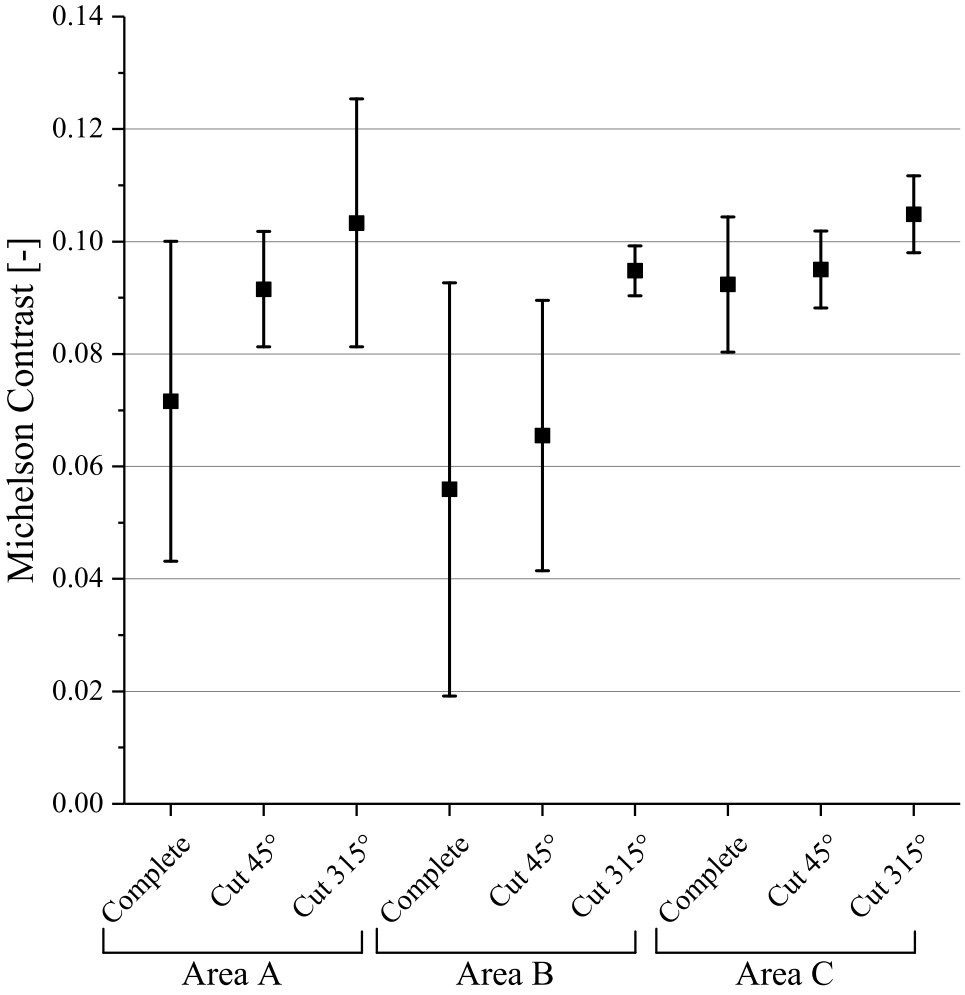

Figure 8.1.: Comparison of the Michelson Contrast in different areas of interest. Values for mean and standard deviation are provided in tab. 8.2.

all four cutted half pieces; subsequently the associated ones were fittingly arranged for better visualization (fig. 8.2c and 8.2d).

We can already see clearly that the severe artifacts of the original part have vanished completely. In order to analyze our data quantitatively, we defined three regions of interest like shown in fig. 8.2b for further analysis. They have been chosen at different material-air-transitions at the outer or inner part of the socket and with different amount of material in the nearer surrounding. At each of these regions we took three points at the border between material and air and calculated the so called Michelson-Contrast for them. The Michelson Contrast MC quantifies the relative distinguishability of an object to the related background and is defined according to $MC = \frac{L_{max}-L_{min}}{L_{max}+L_{min}}$ with L_{min} being the minimum and L_{max} the maximum luminance, respectively [Pelli and Bex 2013]. Alternative quality metrics are available in the literature (see e.g. Crété-Roffet et al. (2007) for a short overview). The results are provided in fig. 8.1 and tab. 8.2. We can see clearly that the cutted parts achieve significantly higher contrast values and therefore an improved edge detectability. The highest contrast values are achieved by the 315°-cut. This is not surprising if we look at the cutting lines: since the socket geometry is not

Table 8.2.: Mean and standard deviation for the contrast comparison of complete turbine blade and two cutted parts. The respective graph is depicted in fig. 8.1.

		Mean Value	Standard Deviation
Area A	Complete	0.07160	0.02843
	Cut 45°	0.09153	0.01026
	Cut 315°	0.10332	0.02202
Area B	Complete	0.05591	0.03677
	Cut 45°	0.06551	0.02403
	Cut 315°	0.09480	0.00443
Area C	Complete	0.09236	0.01202
	Cut 45°	0.09501	0.00683
	Cut 315°	0.10486	0.00682

exactly a rectangle but a trapezoid, there needs to be a longer diagonal line. The 45°-cutted piece is cutted in such a way that it owns this longer line – and since a longer penetration way length is linked to a decreased image quality we can expect lower values of *MC* for this geometry, which is indeed the case.

In summary, it can be seen that the destructive approach seems to be well suited to suppress any artifacts caused by insufficient X-ray penetration completely. Furthermore, we obtain better contrast values that come with an improved edge detection. Anyhow, in most cases we cannot afford a destructive testing, since the loss of the original part is usually not acceptable. Additionally, other tests or measurements (i.e. optical scans) have to be carried out before cutting the workpiece, which can cause problems due to the less flexible workflow and insufficient machine scheduling capabilities.

(a) Simulated Socket Slice

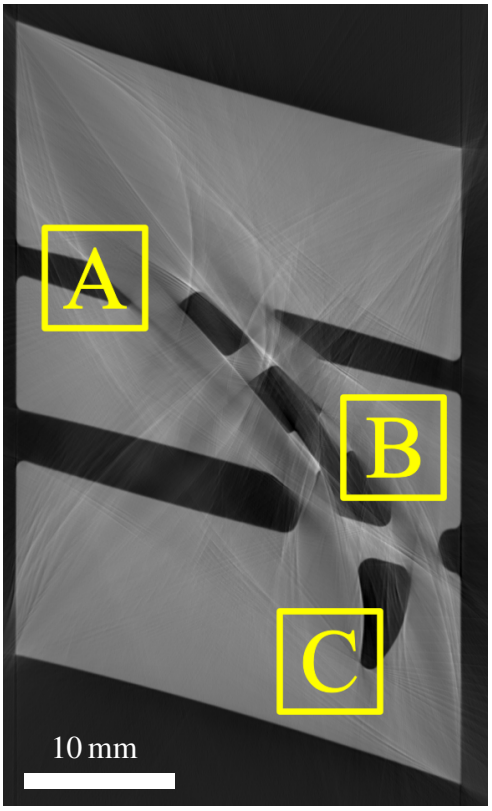

(b) Definition of ROIs for Investigation

(c) 45°-cutted Slice

(d) 315°-cutted Slice

Figure 8.2.: Typical slices of the socket part for our destructive approach. Fig. 8.2a shows the simulated appearance of the entire foil after a CT, while fig. 8.2c and 8.2d show the same geometry for cutted halfs (parts were reassembled after simulation). Fig. 8.2b shows the ROIs we used for subsequent analysis.

9. Entire Replication Workflow for the Considered Turbine Blade

In this chapter we will finally consider the whole replication chain and assess occurring errors and inaccuracies. For a more detailed analysis, we will consider each ROI like defined in sec. 5 separately.

9.1. General Procedure for Reverse Engineering and Analysis

In order to assess our RE-approach, we conducted two CT-scans of blade I with acceleration voltage of 225 keV and 450 keV, respectively. From these we were able to determine the inner surface via DECT, like described in sec. 7.2. For the outside, an optical scan was made (these are the same scan data that have previously been described in sec. 4). From all determined surfaces a mesh was calculated, which was produced subsequently by use of AM. The resulting workpiece is called blade III from now on; in order to avoid confusions, all blades that are examined in this thesis and their relations are depicted in fig. 9.1. Like the original piece, the blade was manufactured from ”EOS NickelAlloy HX” (see sec. B.1) by a layer thickness of 20 µm, but without subsequent sand blasting. We assume that the missing post-processing step is not likely to change the geometry significantly, even though the optic appearance was altered.

Table 9.1.: Used parameters for the CT scan of blade III. Instead of a rod calibration an automatic alignment algorithm was used, which is not assumed to change the scan quality recognizably.

Acceleration Voltage	210 keV
Filament Current	250 µA
Power	52.5 W
Filter	1 mm Copper
SOD	200 mm
SDD	800 mm
Magnification	4.00
Voxel Size	50 µm
Exposure Time	500 ms
Number of Images for Adjustment Averaging	128
Number of Images for Scan Averaging	16
Number of Projections for Scan	2500
Duration of Complete Scan	ca. 5 h 30 min

The replicated part was manufactured with a closed air outlet at the side, which we assume might be caused by inappropriate merging of both – the inner and the outer – meshes. Unfortunately, this issue does not permit powder rests within the blade to exit, so that we obtain a replica that is almost entirely filled with metal dust. This way, the material thickness increases significantly and decreases the image quality for the CT scanning of the replica due to an increased penetration path length. Nevertheless, since we do not have the possibility to remove the dust in a sufficient extent, we performed a low energy CT scan (see tab. 9.1 for scan parameters). We used this CT together with the medium energy scan of blade I to obtain a new inner geometry for investigation

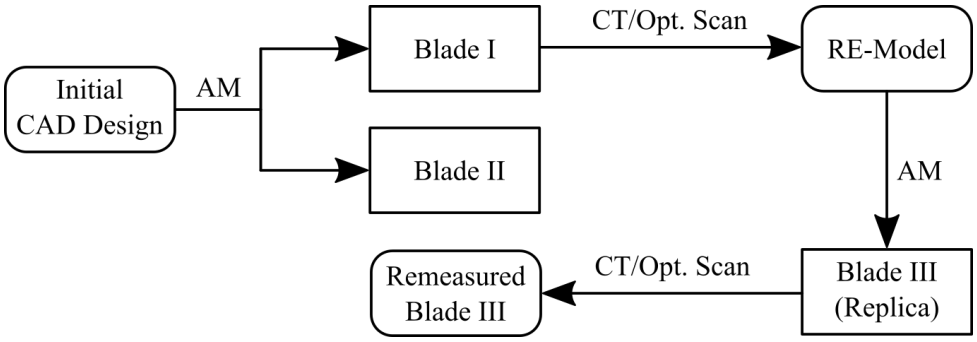

Figure 9.1.: Overview of all three manufactured blades and their position in the replication chain.

via DECT. This measurement was performed in order to reduce the dependence from the 450 keV, i.e. to minimize any influence originating from blade I. The search distance was adjusted to 0.30 mm, which is still significantly higher than any aberration we expect and iterative surface determination was enabled to obtain usable results. The outside geometry was again determined by via optical scanning; the result is also shown in fig. 9.1 as remeasured blade III.
We subsequently compared all derived geometries against each other according to the scheme proposed in section 9.2 and derive error estimations in sec. 9.3.

9.2. Error Considerations for Entire Replication Chain

The complete replication chain is depicted in fig. 9.2. We start with the initially desired geometry and end with the replicated part, like described analogously in sec. 2.3.3. Since our goal is a comprehensive investigation we also have to measure our replica, which is basically the same step like the RE before. This way, we split our whole chain in four separate pieces: the original manufacturing process M (resulting in the original workpiece O), the actual reverse engineering process RE, the Additive Manufacturing step AM (results in the replica Rep) and our final remeasurements for comparison RM. We splitted the Reverse Engineering into the subprocesses of performing the actual measuring (with introduced error α_{RE}) and the mesh generation (with error β_{RE}). The remeasurement part is made up analogously. Usually we would also have the additional error γ_{RE}, which is caused by the generation of an CAD file and holds significant simplifications of the originally measured geometry. Nevertheless, in general we expect this step to actually improve the quality and shift the error distribution back towards the initial design. This is due to the fact that the CAD generation can draw on already known *a priori* information or boundary conditions (see also [Mohaghegh et al. 2007] for deeper considerations concerning this topic). Similar holds for the meshing error β_{RE}, since it might smoothen the surfaces in such an extent that it suits the original geometry better. Since all measurements do possess an inevitable, inherent error, we can only compare the indicated entries C_0 to C_4 directly with each other. For this purpose, we introduce in the following considerations the notation C_{xy} for a comparison of part x with the nominal part y. Still, due to eq. 2.22, we are able to estimate the remaining error sources.

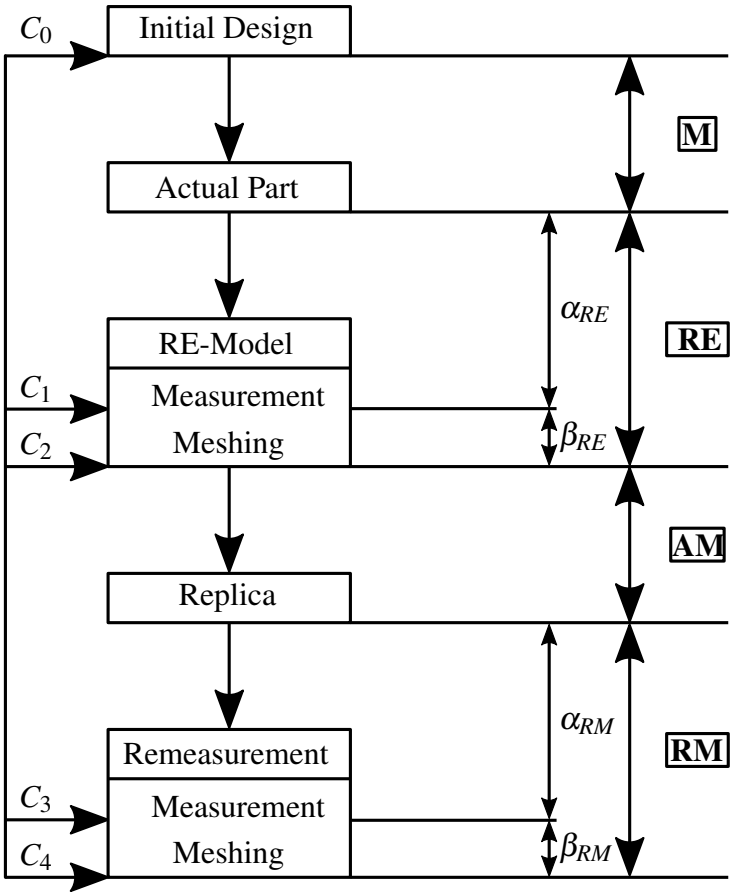

Figure 9.2.: Overview of the entire replication chain. On the left the values are depicted that can be measured and compared to each other. The right side shows occurring errors and their composition.

We want to stress that this approach is still simplified to some degree. Each error distribution is supposed to be approximately Gaussian shaped and symmetric, which is in fact not exactly the case. For the sake of simplification, we will still assume them to form a Gaussian, since the superposition of many distributions tend towards a Gaussian according to the central limit theorem [Buzug 2008, p. 71f].

9.3. Quantitative Analysis of the Error Chain for the Turbine Blade

For our investigation we split the blade again into four ROIs. Since the optical scans are only available as mesh, comparisons C_{1x} and C_{3x} are not possible as well as comparisons C_{x1} and C_{x3}. For the CT-scans, the errors α_{RE} and α_{RM} can be assessed via a comparison of the optical and the X-ray scan of both outside ROIs. For this purpose, we assume that the optical scan is able to capture the outer geometry without any errors; this is reasonable since we already investigated in sec. 5 that the optical scan features a significantly improved accuracy, which is even better than the surface roughness. This investigation has already been performed for blade I in sec. 7.2 (see also fig. 7.2). Therefore, we can use the values given in tab. 7.1 for the foil directly for α_{RE} and $\sigma_{\alpha_{RE}}$. Unfortunately, due to the poor penetrability of the socket, artifacts occur especially at the outside that let the outcome of the comparison appear much

Table 9.2.: Calculated comparisons for the error investigation of all four ROIs. Not all comparisons are necessary for calculation; these are given for completeness only. Results of our comparisons of DECT to optical data at the outer surface are given as well (i.e. difference between CT scan to optical scan at the blade surface). Entries marked with (*) were calculated with a reduced but more representative ROI.

	Inner Socket	Inner Foil	Outer Socket	Outer Foil
C_{10}	$7\,\mu m \pm 55\,\mu m$	$7\,\mu m \pm 45\,\mu m$	–	–
C_{20}	$5\,\mu m \pm 54\,\mu m$	$5\,\mu m \pm 54\,\mu m$	$-40\,\mu m \pm 64\,\mu m$	$-17\,\mu m \pm 25\,\mu m$
C_{21}	$-3\,\mu m \pm 26\,\mu m$	$-3\,\mu m \pm 26\,\mu m$	–	–
C_{30}	$22\,\mu m \pm 73\,\mu m$	$10\,\mu m \pm 87\,\mu m$	–	–
C_{31}	$13\,\mu m \pm 51\,\mu m$	$2\,\mu m \pm 75\,\mu m$	–	–
C_{32}	$13\,\mu m \pm 60\,\mu m$	$2\,\mu m \pm 74\,\mu m$	–	–
C_{40}	$23\,\mu m \pm 74\,\mu m$	$2\,\mu m \pm 70\,\mu m$	$-35\,\mu m \pm 136\,\mu m$	$14\,\mu m \pm 65\,\mu m$
C_{41}	$14\,\mu m \pm 53\,\mu m$	$-7\,\mu m \pm 57\,\mu m$	–	–
C_{42}	$14\,\mu m \pm 52\,\mu m$	$-7\,\mu m \pm 57\,\mu m$	$18\,\mu m \pm 87\,\mu m$	$29\,\mu m \pm 55\,\mu m$
C_{43}	$-1\,\mu m \pm 3\,\mu m$	$-1\,\mu m \pm 2\,\mu m$	–	–
RE-Accuracy	–	–	$42\,\mu m \pm 38\,\mu m$ (*)	$25\,\mu m \pm 33\,\mu m$
RM-Accuracy	–	–	$-41\,\mu m \pm 43\,\mu m$ (*)	$-38\,\mu m \pm 36\,\mu m$

worse than it actually is. Since the inner geometry is less artifact-afflicted, we choose only a restricted ROI, precisely the part between the first and second stage of the fir tree root, for accuracy comparisons. This area shows at the outside a comparable imaging quality like we expect to find at the inside. Values originating from comparisons with reduced ROI are marked with a (*). We performed all comparisons depicted in fig. 9.2; numerical values are shown in tab. 9.2. For this purpose, the geometries to compare were separately registered to each other for every ROI; as consequence, very slight differences in the outcome compared to the results of sec. 6 and 7 occurred, which can be neglected. For the comparisons of CT and optical scans of the foil sections, error corrections according to sec. A.1 were performed with threshold $-0.25\,\mu m$ and $-0.3\,\mu m$, respectively. Figure 9.3 shows the deviations of the CT-scans of the original blade and the replica in comparison to the optical scans of their surfaces. Values are also provided in tab. 9.2 as accuracy of RE and remeasurement (RM). We can see that the CT of the original blade seems to overestimate the amount of material, while the replica scan has deviations in the other direction. This is probably caused by artifacts due to insufficient penetrability, that make it hard to determine the border of the workpiece accurately.

Outer Geometries For the outer geometries, the scheme of fig. 9.2 simplifies, since no unmeshed surfaces are available for comparison. Therefore, the Reverse Engineering and the remeasurement errors cannot be split into the parts α and β. Like already mentioned before, we assume the accuracy of these to be absolutely precise (i.e. $RE = RM = 0$ and $\sigma_{RE} = \sigma_{RM} = 0$), so we can calculate directly:

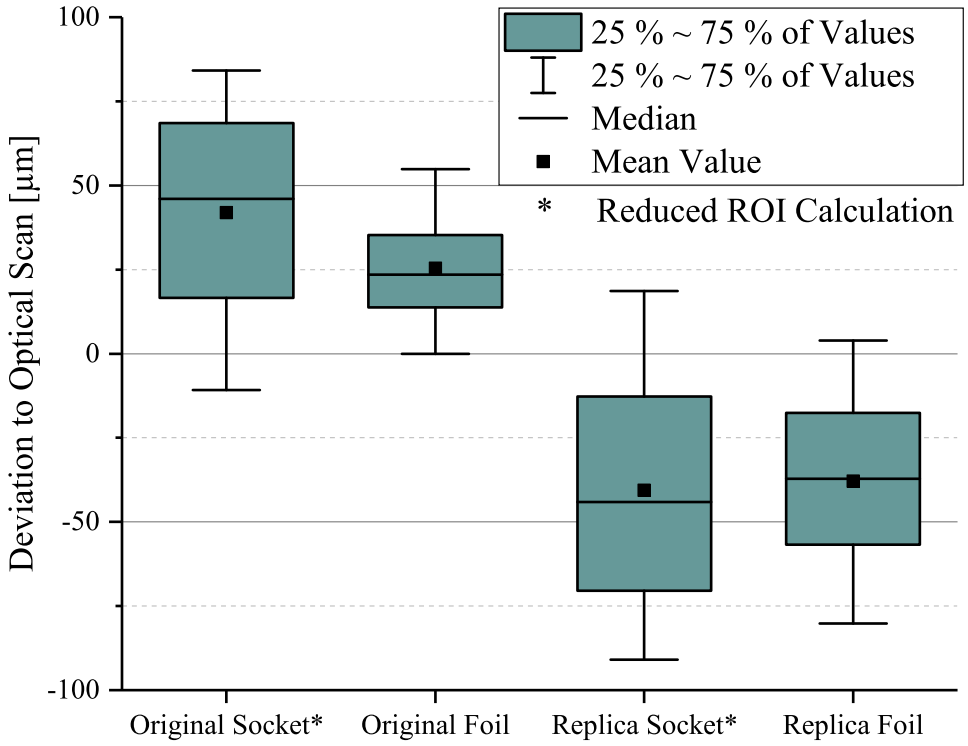

Figure 9.3.: Comparison of the surface of the CTs to the optical scans for both blades. Socket parts were calculated with only the intermediate stage of the fir tree root as considered ROI in order to obtain more meaningful data. Numerical values are given in tab. 9.2.

$$C_{20} = M + RE = M \tag{9.1}$$

$$C_{42} = RM + AM = AM \tag{9.2}$$

$$\sigma_M = \sigma_{C_{20}} \tag{9.3}$$

$$\sigma_{C_{40}} = \sqrt{\sigma_M^2 + \sigma_{AM}^2} \tag{9.4}$$

$$\rightarrow \sigma_{AM} = \sqrt{\sigma_{C_{40}}^2 - \sigma_{C_{20}}^2}\,. \tag{9.5}$$

Results are given in tab. 9.3 and figures 9.4 and 9.5. Remanufacturing fidelity for the outside geometry is given with $5\,\mu m \pm 120\,\mu m$ for the foil and $31\,\mu m \pm 60\,\mu m$ for the socket section of the blade. For the original manufacturing we state an accuracy of $-40\,\mu m \pm 64\,\mu m$ and $-17\,\mu m \pm 25\,\mu m$, respectively. We observe that the remanufacturing process accounts for approximately two third of the overall deviations when speaking of distribution broadening. This is likely caused by the fact that the mesh was printed directly without smoothing surfaces or optimizing the geometry in order to make it more suitable for printing. The original manufacturing method disposes less material than actually needed, causing aberrations of up to $-40\,\mu m$ in average, while the remanufacturing leaves more material than needed (up to $31\,\mu m$ in average). We assume this is caused partly by inaccuracies of the optical sensor, which we expect to rather overestimate the

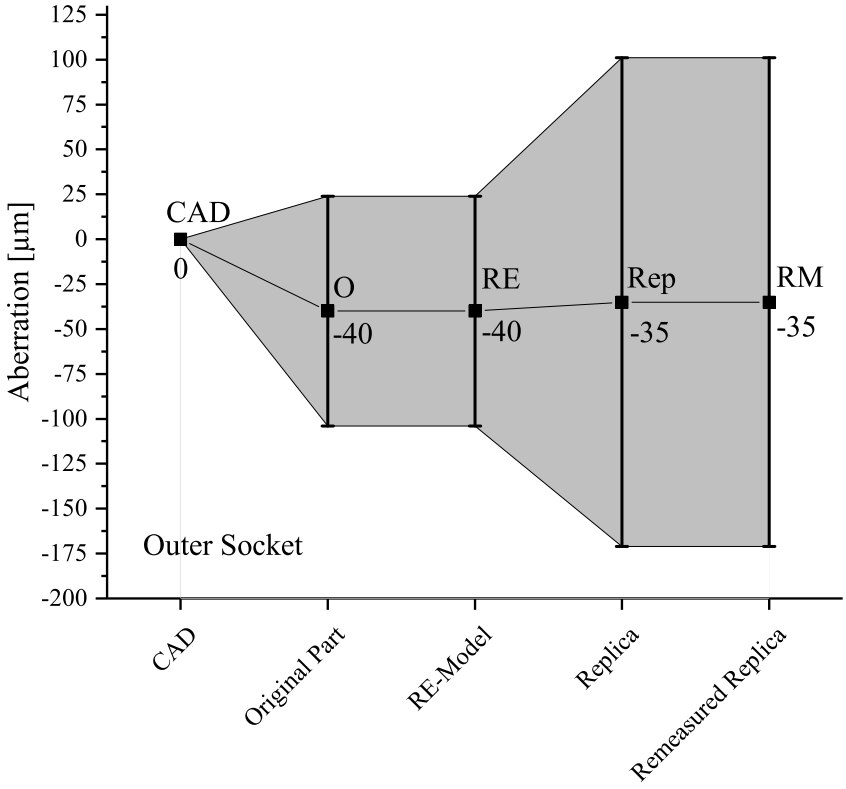

Figure 9.4.: Complete error chain for the outer part of the socket. The accuracy of the replica (AM) is given with $-35\,\mu m \pm 136\,\mu m$.

material amount than underestimate it. These errors accumulates, since the geometry is scanned with overhang, produced this way and scanned with positive derivation afterwards as well.

Inner Geometries Calculating accuracies for the inner geometries is more demanding, since we have separate comparisons for surface and mesh available and possess no detailed knowledge about the accuracy of the method. In order to determine the latter, we previously performed comparisons at the outside of CT and optical measurement (see sec. 9.1). We start our calculations by determining the offsets:

$$C_{20} = M + RE = M + \alpha_{RE} + \beta_{RE} \tag{9.6}$$

$$C_{21} = \beta_{RE} \tag{9.7}$$

$$\rightarrow M = C_{20} - C_{21} - \alpha_{RE} \tag{9.8}$$

$$\rightarrow RE = C_{20} - M = \alpha_{RE} + C_{21} \tag{9.9}$$

$$C_{42} = AM + RM = AM + \alpha_{RM} + \beta_{RM} \tag{9.10}$$

$$C_{43} = \beta_{RM} \tag{9.11}$$

$$\rightarrow AM = C_{42} - C_{43} - \alpha_{RM} \tag{9.12}$$

$$\rightarrow RM = C_{42} - AM = \alpha_{RM} + C_{43}\ . \tag{9.13}$$

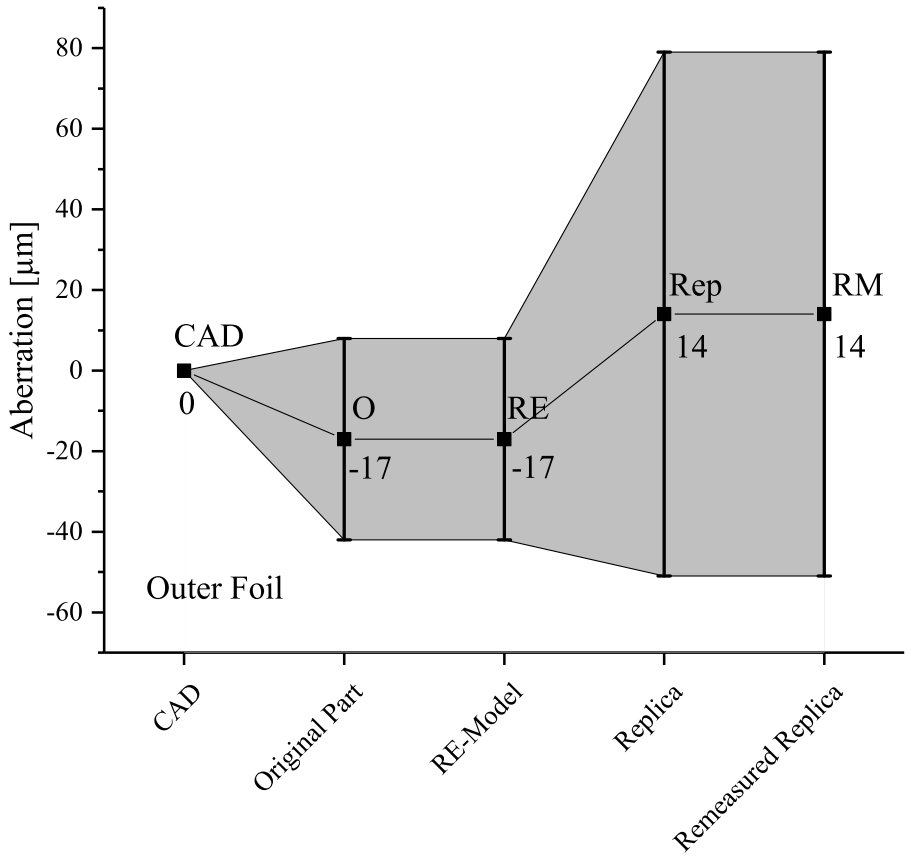

Figure 9.5.: Complete error chain for the outer part of the foil. The accuracy of the replica (AM) is given with 14 µm ± 65 µm.

For the standard deviations we obtain:

$$\sigma_{C_{20}} = \sqrt{\sigma_M^2 + \sigma_{\alpha_{RE}}^2 + \sigma_{\beta_{RE}}^2} \tag{9.14}$$

$$\rightarrow \sigma_M = \sqrt{\sigma_{C_{20}}^2 - \sigma_{C_{21}}^2 - \sigma_{\alpha_{RE}}^2} \tag{9.15}$$

$$\sigma_{C_{20}} = \sqrt{\sigma_{RE}^2 + \sigma_M^2} \tag{9.16}$$

$$\rightarrow \sigma_{RE} = \sqrt{\sigma_{C_{20}}^2 - \sigma_M^2} \tag{9.17}$$

$$\sigma_{C_{42}} = \sqrt{\sigma_{AM}^2 + \sigma_{\alpha_{RM}}^2 + \sigma_{\beta_{RM}}^2} \tag{9.18}$$

$$\rightarrow \sigma_{AM} = \sqrt{\sigma_{C_{42}}^2 - \sigma_{C_{43}}^2 - \sigma_{\alpha_{RM}}^2} \tag{9.19}$$

$$\sigma_{C42} = \sqrt{\sigma_{AM}^2 + \sigma_{RM}^2} \tag{9.20}$$

$$\rightarrow \sigma_{RM} = \sqrt{\sigma_{C_{42}}^2 - \sigma_{AM}^2}\,. \tag{9.21}$$

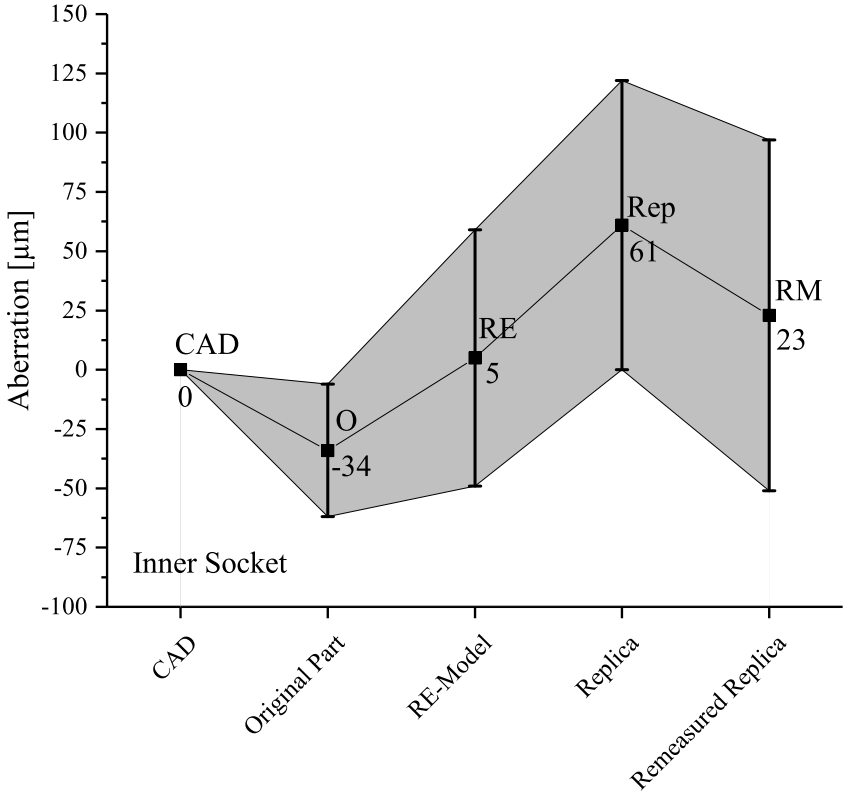

Figure 9.6.: Complete error chain for the inner socket of the blade. The accuracy of the replica (AM) is given with 61 µm ± 61 µm and the final remeasurement distribution (RM) with 23 µm ± 74 µm.

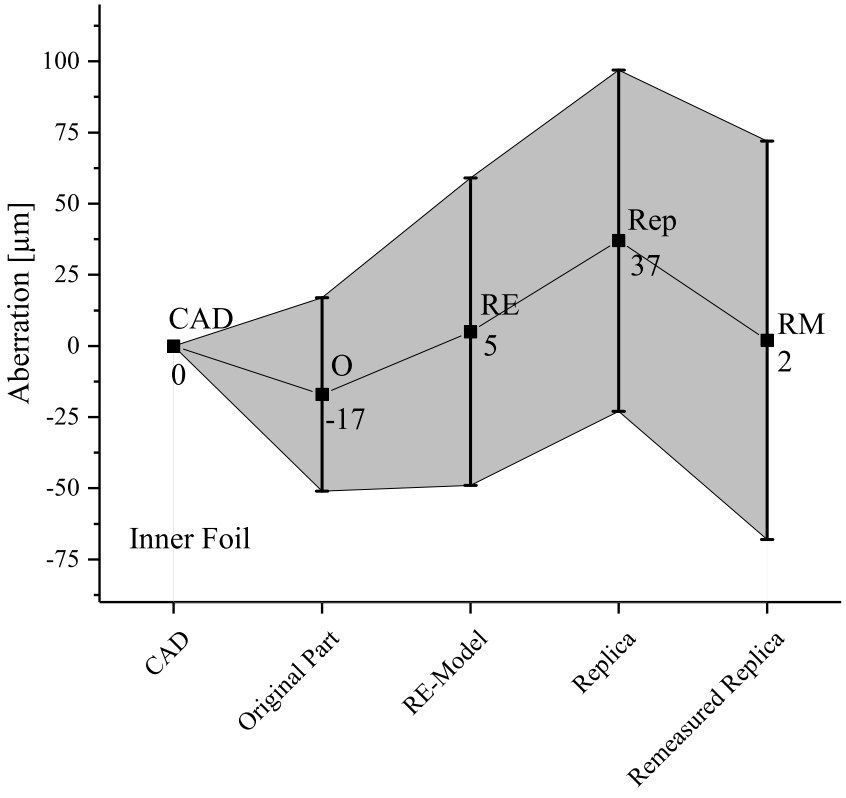

Figure 9.7.: Complete error chain for the inner foil of the blade. The accuracy of the replica (AM) is given with 37 µm ± 60 µm and the final remeasurement distribution (RM) with 2 µm ± 70 µm.

Results are also given in tab. 9.3 as well as figures 9.6 and 9.7. For the inner geometries the manufacturing errors of the original workpiece and the replica exhibit the same tendency like for the outer geometries: in the first production step, too few material has been deposited, while manufacturing the replica leaves too much material at the workpiece. While these derivations seem comparable for the foil sections, the inner socket exhibit – though having a less complex geometry – higher aberrations than its outside. Also, in general the deviations are higher than for the outer side of the blade. This could pose a problem, since the cooling channel diameter is affected, which can diminish the ability to keep the blade within temperature tolerances since less cooling fluid can pass through the channels.

We provide an overview for each ROI of the deviations that occur in comparison to the overall chain deviation $\sigma_{C_{40}}$ in figure 9.8. We want to stress that the percentages given is just a rough value for orientation, calculated via $\sigma_{xy}/\sum\sigma_{xy}$. Since the values are not summing up linearly, these numbers are not exactly correct, but form an evaluation method that is more intuitive to grasp. We do only investigate for the origin of evolving standard deviation, since these errors are most relevant for the accuracy of the part, whereas mean value shifts can be compared for more easily.

We can see clearly that the manufacturing of the replica is much more affected by errors than the original production of the workpiece (65 % and 71 % of deviations originate from replica manufacturing), though production method and slice thickness was identical. This trend holds as well for the inner geometry, but to a much lesser extent. We observed also that the errors are almost equally distributed to all four considered origins of error.

Surprisingly, the remeasurement quality is better than the RE accuracy, even though more artifacts occurred. Also, when considering the composition of the RE and RM errors (see tab. 9.3), we can see that the errors introduced via meshing become significantly smaller (44 % and 41 % for the RE in comparison to only 5 % and 7 % of the remeasurement). We assume that both issues are linked: due to the poor remeasurement scan quality, the meshing algorithm relies more on the 450 keV-scan of the DECT approach than on the low energy scan. We already showed in sec. 7.3 that for such issues the medium energy scan is taken for the respective part of the geometry, while the low energy scan is completely ignored. The surface geometry we obtain by this approach is simpler (due to the reduced precision of the 450 keV-CT), which also causes the meshed surface to exhibit smaller derivations than a more detailed scan. The result shows also that the meshing quality seems to be crucial for obtaining accurate meshes of high-precision scans, since approx. half of the evolving standard deviation can be traced back to them. We want to stress that for productive use of the blades, the remeasurement must not necessarily be considered since it does not affect the quality of the reprint. But if the replicated part needs to be checked for tolerances or quality issues, the remeasurement precision becomes crucial.

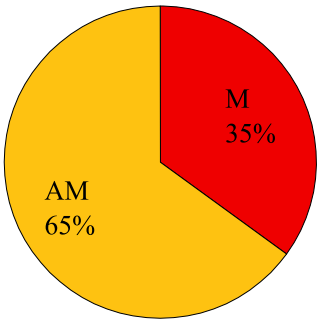

Outer Socket

(a) Deviation Composition for the Outer Socket

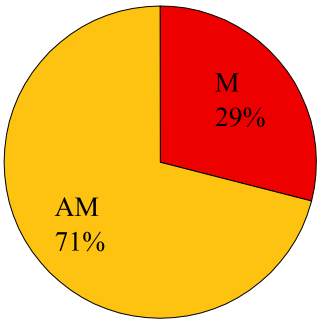

Outer Foil

(b) Deviation Composition for the Outer Foil

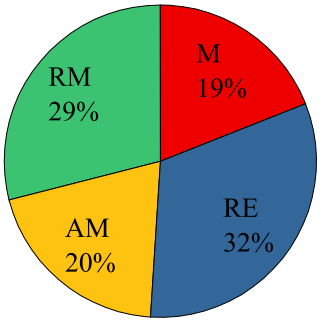

Inner Socket

(c) Deviation Composition for the Inner Socket

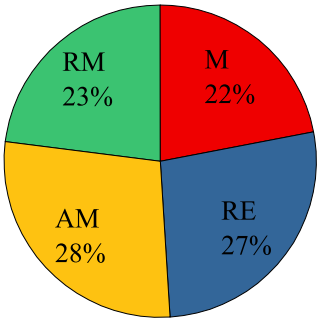

Inner Foil

(d) Deviation Composition for the Inner Foil

Figure 9.8.: Composition of the standard deviation of the remeasured blade.

When considering all CT scans, we can see that these are broadening the distribution only to a small degree (i.e. small standard deviation), but exhibit a high mean shift. We conclude that the scans are very well suited for RE, but need to be compensated for an offset value for more accurate results. We assume that the offset results of an interplay between several factors: the often inappropriate iso-50 % approach (see also sec. 2.3.2) accounts probably as well as insufficient beam hardening correction and other superposing artifacts. These issues must be addressed and artifacts suppressed in order to enhance image and RE quality of the procedure.
We can also calculate a value for the replication quality, i.e. the deviations between the replica and the original workpiece. In our case these are given directly with the comparisons C_{42} for the outer section and are $18\,\mu m \pm 87\,\mu m$ for the outer socket and $29\,\mu m \pm 55\,\mu m$ for the outer foil, respectively. For the inner geometries this error E_{Rep} is basically a composition of RE and AM, which can easily be calculated via $E_{Rep} = RE + AM$ and $\sigma_{E_{Rep}} = \sqrt{\sigma_{RE}^2 + \sigma_{AM}^2}$. Therefore, we state a replication accuracy of $95\,\mu m \pm 54\,\mu m$ for the inner socket and $54\,\mu m \pm 61\,\mu m$ for the inner foil.

Table 9.3.: Results of the error calculation for the entire replication workflow for each ROI. Depicted are shift of mean, distribution broadening by additional standard deviation *SD* and share of the final standard deviation. Numbers are rounded.

	Error Source	Mean Shift	Additional *SD*	Fraction of End-*SD*
Inner Foil	Original Manufacturing	−17 µm	34 µm	ca. 22 %
	Reverse Engineering (RE)	22 µm	42 µm	ca. 27 %
	Additive Manufacturing	32 µm	44 µm	ca. 28 %
	Remeasurement (RM)	−39 µm	36 µm	ca. 23 %
	α_{RE}	25 µm	33 µm	ca. 56 % of RE
	β_{RE}	−3 µm	26 µm	ca. 44 % of RE
	α_{RM}	−38 µm	36 µm	ca. 95 % of RM
	β_{RM}	−1 µm	2 µm	ca. 5 % of RM
Inner Socket	Original Manufacturing	−34 µm	28 µm	ca. 19 %
	Reverse Engineering (RE)	39 µm	46 µm	ca. 32 %
	Additive Manufacturing	56 µm	29 µm	ca. 20 %
	Remeasurement (RM)	−42 µm	43 µm	ca. 29 %
	α_{RE}	42 µm	38 µm	ca. 59 %of RE
	β_{RE}	−3 µm	26 µm	ca. 41 % of RE
	α_{RM}	−41 µm	43 µm	ca. 93 % of RM
	β_{RM}	−1 µm	3 µm	ca. 7 % of RM
Outer Foil	Original Manufacturing	−40 µm	64 µm	ca. 35 %
	Reverse Engineering (RE)	0 µm	0 µm	0 %
	Additive Manufacturing	5 µm	120 µm	ca. 65 %
	Remeasurement (RM)	0 µm	0 µm	0 %
O. Socket	Original Manufacturing	−17 µm	25 µm	ca. 29 %
	Reverse Engineering (RE)	0 µm	0 µm	0 %
	Additive Manufacturing	31 µm	60 µm	ca. 71 %
	Remeasurement (RM)	0 µm	0 µm	0 %

10. Additional Test Cases and Examples

The replication workflow used in previous chapters is not only applicable for turbine blade manufacturing, but can be used in many other fields to produce replicas or assess production quality of parts. Therefore, we examine in this chapter two additional test examples in order to illustrate other application scenarios.

10.1. Test Pieces and Reverse Engineering Process

For our demonstration we choose two different test pieces. The first one is a scaled polymer model of a high temperature burner tip with internal cooling system and several feeders for different reactants (diameter ca. 115 mm, height 135 mm). The second is also a scaled plastic model in the shape of one of the flow swirler lines (diameter ca. 90 mm, height 150 mm) of the burner tip. Both objects were produced via FDM with initially unknown print quality and are shown in fig. 10.1. The parts themselves are highly complex – featuring, for instance, free-form surfaces and rips – and the result of intensive fluid dynamic optimizations. More details concerning the test pieces can be found at Biedermann (2017). The parts were chosen due to the following reasons:

- Since we are not going to use any other RE method than CT, we do not want artifacts to occur. Consequently, the material needs to be uncomplicated to probe.
- The parts can be reproduced easily by use of a simple FDM system.
- Parts must be manufactured from a monomaterial, no elements with significantly higher or lower attenuation coefficients are permitted.
- Complex internal features should be included to show capabilities of our RE method, but they are supposed to be arranged in such a way that still allows reprinting via FDM.

We performed a CT of each part, determined the surface via VGStudio and generated a mesh. Subsequently, the mesh was directly printed without any further processing steps. For the flow swirler the printer was a MakerBot Replicator 2 (*MakerBot Industries, LCC*, New York City, USA) and the time for printing took 33 h 25 min. Due to limitations of the building plate, we had to remove ca. 2 cm from the top of the STL-file before printing. For all further considerations we will only investigate this smaller printed part.
The burner tip workpiece was scanned as well. Slight cone beam artifacts occurred, especially in the plane lower side of the piece, but did not surpass acceptable magnitudes. Since this part is more complex, we produced two replicas: the first one (termed replica or burner tip I) was manufactured via Replicator 2 (print time ca. 35 h), i.e. the same system as the flow swirler replica. A better quality print was achieved by use of an Ultimaker 2+ printer (*Ultimaker B.V.*, Geldermalsen, Netherlands) with a print time of ca. 5 d 16 h. Unfortunately, due to a misprint

Figure 10.1.: Test pieces for our exemplary RE process. Left: a single flow swirler line, which is part of the burner tip (depicted cutted open on the right, models not to scale). The burner tip itself is highly complex and features several filigrane structures on the inside.

one of the supply pipes of the part was destroyed entirely, with the second one having strong aberrations; VGStudio was adjusted to ignore these destroyed structures entirely, so that only the rest of the piece is investigated. This part is named replica II from now on.

Next, the parts were scanned via CT and the steps for the mesh generation were repeated. The complete workflow has already been described with focus on error propagation in sec. 9.2. Parameters for all CTs are given in tab. 10.1. We did not perform rod calibrations, but used an automatic alignment algorithm instead. We expect potential inaccuracies caused by that procedure to be negligible. We analyzed all gathered data and performed estimations on part and process accuracy, like described in the next section 9.2. Examples were calculated in sec. 10.2 and 10.3, respectively.

Table 10.1.: Parameters for CT of the test pieces. The scan for the original burner tip and original swirler were made first, subsequently the target was replaced completely. As consequence, current values of later CTs are not comparable directly anymore. No rod calibration was performed, instead we used an automatic alignment algorithm.

	Burner Tip	Burner Tip Replica I	Burner Tip Replica II	Swirler	Swirler Replica
Acceleration Voltage	180 V	180 V	190 V	140 V	180 V
Filament Current	450 µA	420 µA	350 µA	650 µA	400 µA
Power	81 W	91 W	66.5 W	91 W	72 W
Filter	2 mm Cu	2 mm Cu	2 mm Cu	2 mm Cu	2 mm Cu
SOD	400 mm	400 mm	400 mm	400 mm	400 mm
SDD	800 mm	800 mm	800 mm	800 mm	800 mm
Magnification	2.00	2.00	2.00	2.00	2.00
Voxel Size	100 µm	100 µm	100 µm	100 µm	100 µm
Exposure Time	500 ms	500 ms	500 ms	500 ms	500 ms
Number of Images for Adjustment Averaging	32	64	64	32	64
Number of Images for Scan Averaging	8	8	8	8	8
Number of Projections for Scan	2000	2000	2000	1500	1500
Duration of Scan	2 h 15 min	2 h 15 min	2 h 15 min	1 h 40 min	1 h 40 min

10.2. Example 1: Flow Swirler

Now we want to perform a first exemplary error calculation of the chain proposed in sec. 9.2 with the flow swirler part, which was introduced in sec. 10.1. For the sake of simplification, we do not consider each entire error distribution, but only calculate the standard deviation and mean value. All comparisons C_{xy} are listed in tab. 10.2. Since the production via FDM requires an internal support structure and a fill density $\ll 100\,\%$ we get huge additional errors for all comparisons. Therefore, we pre-filtered our data and used only a certain amount of them, which is given as percentage value in the table. Since the support structure is partially the same for both test pieces, these percentage values are higher for comparisons C_{32} and C_{42}. For the mesh comparisons we used all values, since we previously applied the command ”remove isolated components” on both of them, which removed most of the undesired support geometries. The detailed correction protocol is explained in sec. A.2 in the appendix.

Since no optical scan was made, an assessment of the error α_{RE} is directly not possible. The error that comes possibly next to this, is described in fig. 5.10 where we compared the convex and concave surfaces obtained by via CT. We assume that the value for the convex blade side of the low energy scan fits our considerations best, since we will use the same energy but without occurring artifacts; this was also the case for the convex side. From tab. 5.3 we can derive an approximate value for $RE = \alpha_{RE} + \beta_{RE} \approx 21\,\mu\text{m}$ and $\sqrt{\sigma^2_{\beta_{RE}} + \sigma^2_{\alpha_{RE}}} \approx 14\,\mu\text{m}$. We also assume that the measurement error is approximately identical for the reverse engineering and

the remeasurement process, i.e. $\alpha_{RE} = \alpha_{RM}$ and $\sigma_{\alpha_{RE}} = \sigma_{\alpha_{RM}}$ holds. Since we are investigating the same part with the same measurement technique and even very similar parameters, this assumption seems to be reasonable. Due to easier handling, we will prefer to compare meshes from now on, as far as their accuracy is acceptable.
For our comparisons we can calculate the desired mean shifts by:

$$RM = \alpha_{RM} + \beta_{RM} = RE = \alpha_{RE} = \beta_{RE} = 21\,\mu\text{m} \tag{10.1}$$
$$C_{20} = RE + M = \alpha_{RE} + \beta_{RE} + M \tag{10.2}$$
$$\rightarrow M = C_{20} - 21\,\mu\text{m} \tag{10.3}$$
$$C_{40} = M + RE + AM + RM = M + 2RE + AM \tag{10.4}$$
$$\rightarrow AM = C_{40} - M - 2RE\ . \tag{10.5}$$

For the deviations we obtain

$$\sigma_{RM} = \sigma_{RE} = \sqrt{\sigma_{\alpha_{RE}}^2 + \sigma_{\beta RE}^2} = 14\,\mu\text{m} \tag{10.6}$$
$$\sigma_{20} = \sqrt{\sigma_M^2 + \sigma_{RE}^2} \tag{10.7}$$
$$\rightarrow \sigma_M = \sqrt{\sigma_{20}^2 - (\sigma_{\alpha_{RE}}^2 + \sigma_{\beta RE}^2)} = \sqrt{\sigma_{20}^2 - (14\,\mu\text{m})^2} \tag{10.8}$$
$$\sigma_{C_{40}} = \sqrt{\sigma_M^2 + \sigma_{RE}^2 + \sigma_{AM}^2 + \sigma_{RM}^2} \tag{10.9}$$
$$\rightarrow \sigma_{AM} = \sqrt{\sigma_{40}^2 - \sigma_M^2 - 2\sigma_{RE}^2}\ . \tag{10.10}$$

Tab. 10.3 provides an overview of each part of the chain and its share at the combined RE-AM-error. Mind that the calculation above differs slightly from the calculations performed in sec. 9.3 and has stronger aberrations towards the end of the chain as if it were calculcated with the former method. Nevertheless, the differences are negligible but give us the opportunity to provide an alternative calculation method. As before, values do not take the nonlinearity of the error propagation into account, but is more intuitive to grasp. Also depicted is the origin of evolving standard deviation, since this value is more important than the mean shift, which can be compensated more easily. We can see clearly that the part manufacturing errors are significantly larger than all errors introduced by measurement. The chart also reveals that our AM system, which was used to produce the replica, provides results that are remarkably worse in comparison to the AM machine used to generate the original part. For the given example we would be able to produce a replica of the original part with a tolerance of ca. $96\,\mu\text{m} \pm 831\,\mu\text{m}$.

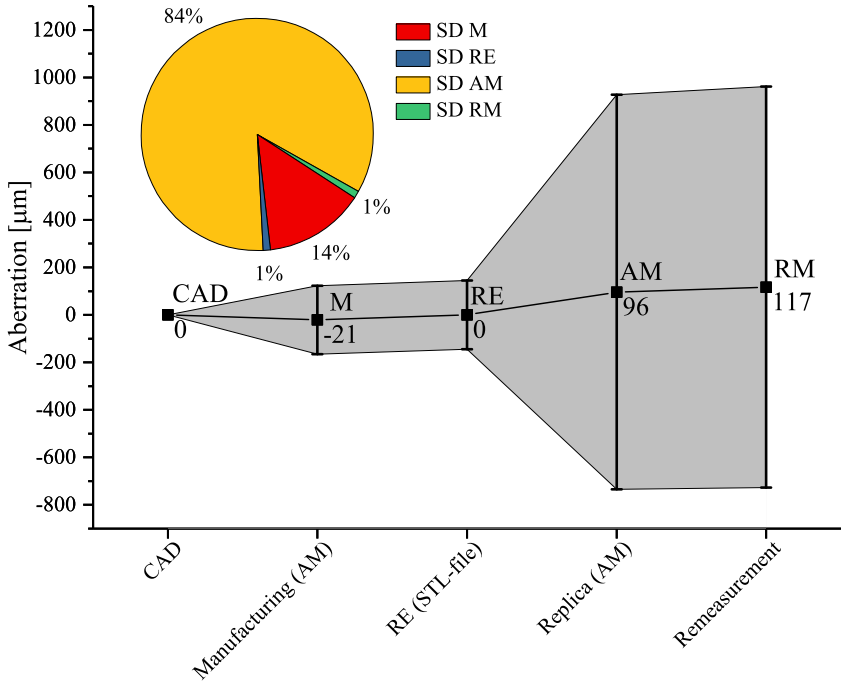

Figure 10.2.: The entire error chain for the swirler part. Depicted is the aberration to the originally desired geometry (i.e. CAD) together with the spread of the distribution after each step. First manufacturing process was accomplished by a different AM system and the outcome of the RE was a STL file. The pie chart shows the source of standard deviations, splitted into each step.

Table 10.2.: Comparisons for the error investigation for the flow swirler. Comparison C_{30} and conventional calculations for C_{30} and C_{40} and are given for completeness only. Values indicated with "*" have been determined via alternative calculation method, see sec. A.2.

Comparison	Mean Value	Standard Deviation	Share Used
C_{10}	0 µm	145 µm	76 %
C_{20}	0 µm	145 µm	76 %
C_{32}	79 µm	417 µm	88 %
C_{21}	0 µm	3 µm	88 %
C_{42}	99 µm	460 µm	100 %
C_{43}	0 µm	5 µm	100 %
C_{40}	117 µm	844 µm	47 %*
C_{40}	−190 µm	707 µm	87 %
C_{30}	133 µm	817 µm	47 %*
C_{30}	−183 µm	705 µm	87 %

Table 10.3.: Overview of the error propagation for the entire flow swirler RE and AM.

Error Source	Mean Shift	Additional *SD*	Fraction of End-*SD*
Original Manufacturing	–21 µm	144 µm	ca. 12 %
Reverse Engineering	21 µm	14 µm	ca. 1 %
Additive Manufacturing	96 µm	831 µm	ca. 85 %
Remeasurement	21 µm	14 µm	ca. 2 %

10.3. Example 2: Burner Tip

Contrary to the previous examination in sec. 10.2, we produced two different replicas by use of two different printing systems of our second test piece, the burner tip (see also sec. 10.1). Both parts were scanned and investigated separately, but originate from the same reverse engineered model. Figure 10.3 provides an overview of the burner tip workflow.

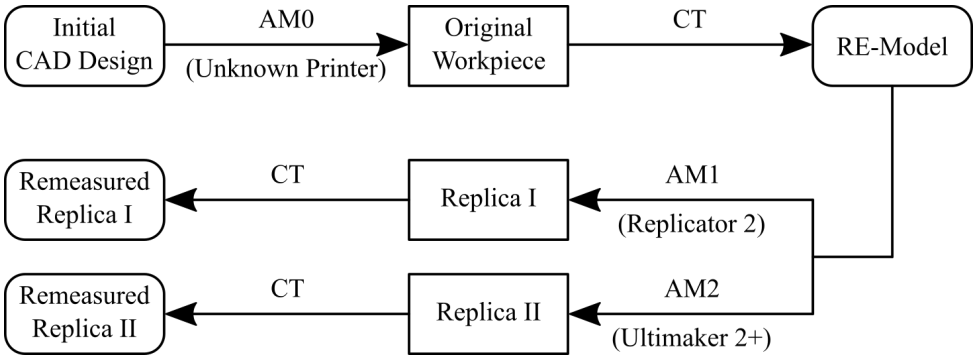

Figure 10.3.: Workflow for the burner tip replication investigations. We have an original workpiece given and derive a RE model from it. By use of two different AM systems, two replicas have been produced subsequently and remeasured by use of CT separately, so the final datasets can be compared with the original design.

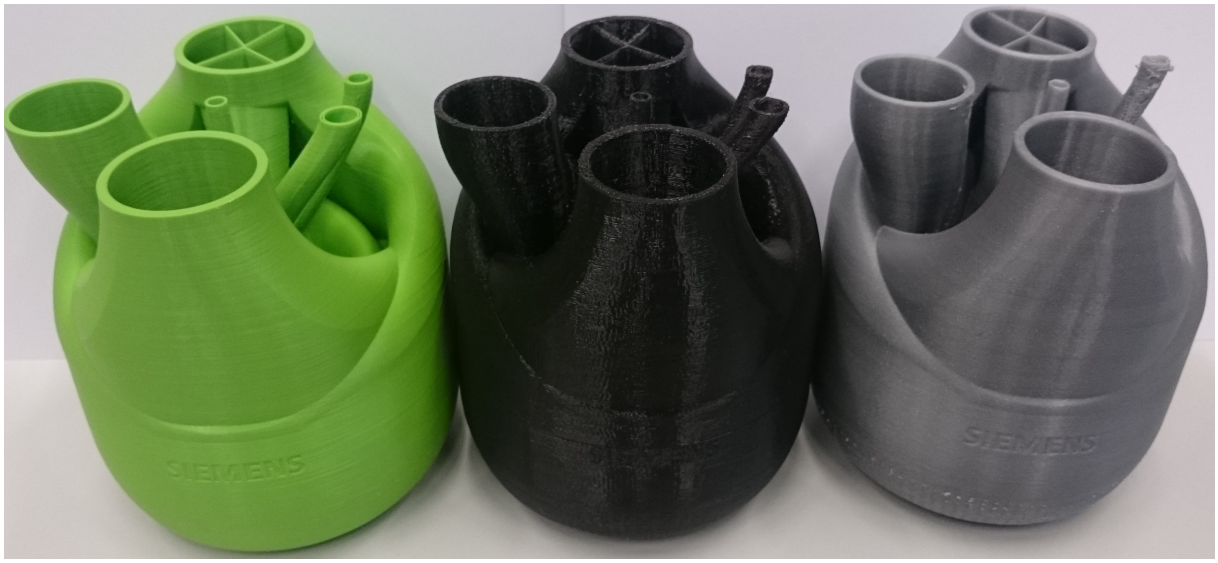

Figure 10.4.: Burner tip and manufactured replicas. From left to right: original part, low-quality print by Replicator 2 (replica I), good-quality print by Ultimaker 2+ (replica II).

We start the calculations for the burner tip test piece analogous to sec. 10.2. Original burner tip and replicas are depicted in fig. 10.4. We assume again the same errors for reverse engineering, which are given by $\alpha_{RE} + \beta_{RE} \approx 21\,\mu\text{m}$ and $\sqrt{\sigma^2_{\beta_{RE}} + \sigma^2_{\alpha_{RE}}} \approx 14\,\mu\text{m}$. For comparison C_{20}, we had to apply a correction for the filling structure again (values below $-0.5\,\mu\text{m}$ are ignored). Here we found that the amount of usable data points lies only at 68 % compared to 76 % of the same comparison for the flow swirler (see table 10.4). This is probably caused by the greater material volume-surface ratio of the object, which makes more filling necessary. Other values

Table 10.4.: Comparisons for the error investigation of the burner tip. For comparisons C_{10}, C_{20}, C_{21} only values higher than 0.7 mm were used. Deviations of replica I were calculated with a lower cutoff of −0.9 mm and −0.7 mm for replica II.

	Comparison	Mean Value	Standard Deviation	Share Used
	C_{10}	72 µm	288 µm	68 %
	C_{20}	62 µm	291 µm	98 %
	C_{21}	1 µm	47 µm	100 %
Replica I	C_{30}	23 µm	521 µm	85 %
Replica I	C_{32}	43 µm	582 µm	85 %
Replica I	C_{40}	21 µm	522 µm	85 %
Replica I	C_{42}	−45 µm	443 µm	85 %
Replica I	C_{43}	−3 µm	11 µm	100 %
Replica II	C_{30}	87 µm	327 µm	87 %
Replica II	C_{32}	14 µm	170 µm	87 %
Replica II	C_{40}	87 µm	328 µm	87 %
Replica II	C_{42}	19 µm	205 µm	87 %
Replica II	C_{43}	−3 µm	8 µm	100 %

Table 10.5.: Overview of the error propagation for the entire burner tip RE and AM.

Error Source	Mean Shift	Additional *SD*	Fraction of End-*SD*
Original Manufacturing	41 µm	291 µm	Rep. I: 39 %, Rep. II: 62 %
Reverse Engineering	21 µm	14 µm	Rep. I: 2 %, Rep. II: 3 %
Additive Manufacturing (Replica I)	−62 µm	433 µm	57 %
Additive Manufacturing (Replica II)	4 µm	151 µm	32 %
Remeasurement (Replica I)	21 µm	14 µm	2 %
Remeasurement (Replica II)	21 µm	14 µm	3 %

were calculated analogously and can be found in tab. 10.5. Since the distribution changes with comparisons later in the chain we had to adjust our cut-off-value accordingly. For comparisons C_{30} to C_{43} of replica I only values higher than −0.9 µm and for replica II higher than −0.7 mm were used to compare for errors introduced by the missing material filling of the walls.

The results of our calculation are shown in fig. 10.5a and 10.5b, respectively. We can see immediately that – unlike the swirler tip – the original manufacturing and our reverse-engineered manufacturing quality is comparably good. Nevertheless, measurement errors are negligible again, making up between 4 % to 6 % of the overall standard deviation. We also found that the printing results of the Replicator 2 are inferior to the Ultimaker 2. In fact, this is in agreement with the appearance of all parts, where the Replicator-part featured a less smooth surface, and the Ultimaker-part a better quality than the original workpiece. For the overall replication quality we would be able to reach 0 µm ± 522 µm for the Replicator and 66 µm ± 328 µm for the Ultimaker chain. Again, for improvements the AM accuracy, but also the original manufacturing quality should be improved.

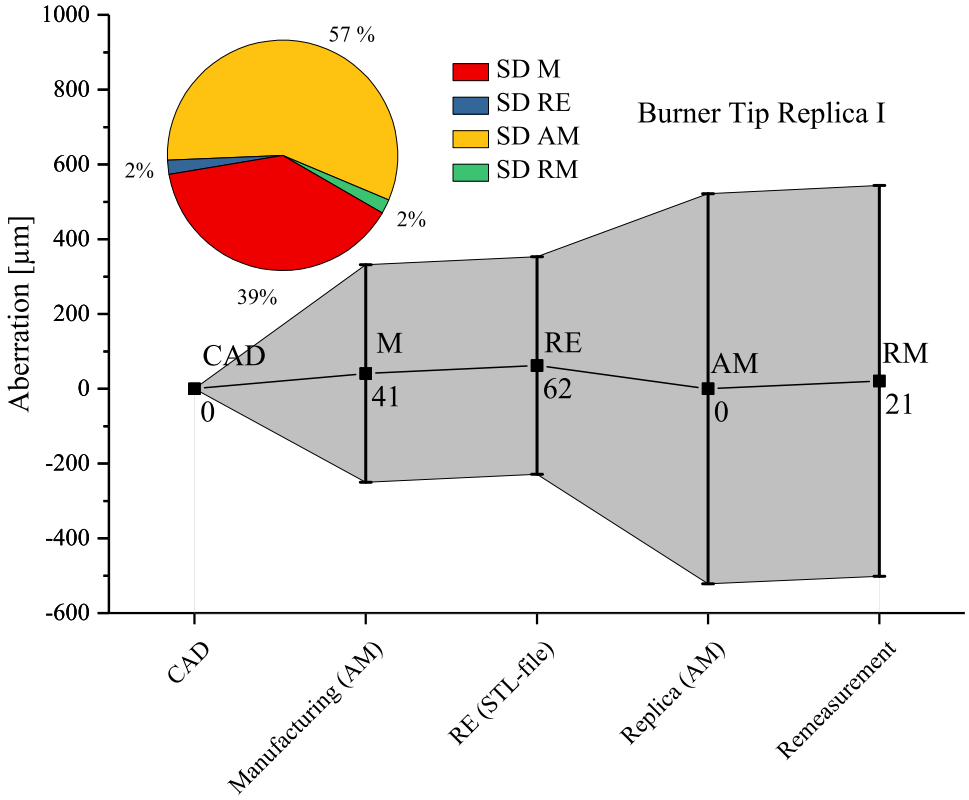

(a) Complete Error Chain for Burner Tip I

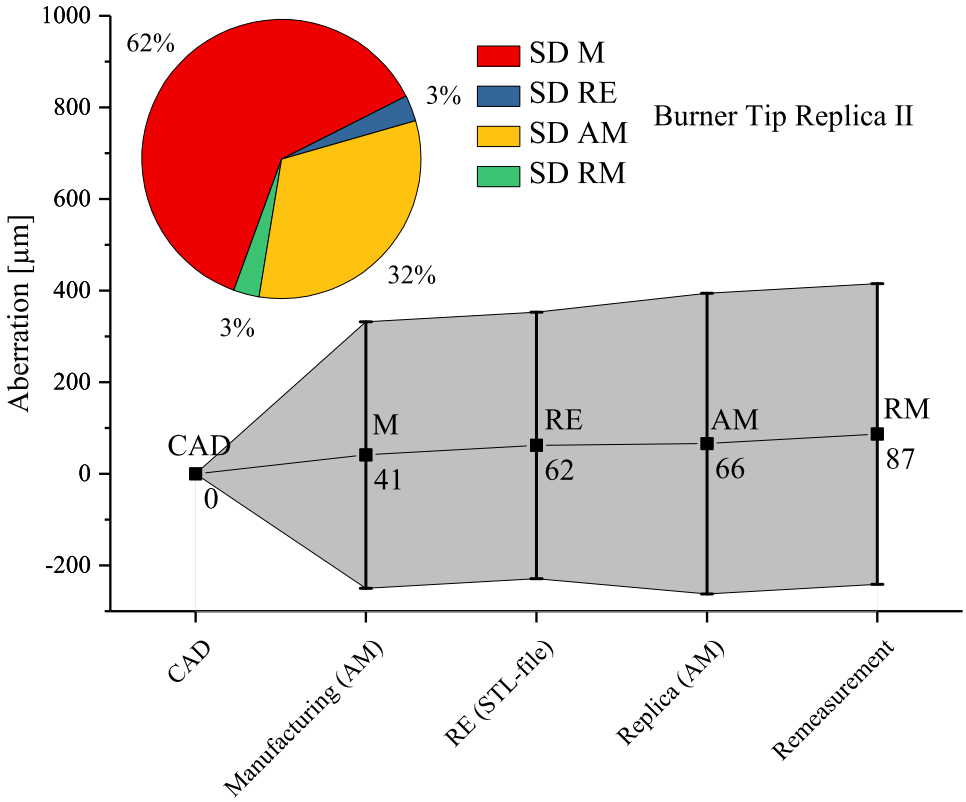

(b) Complete Error Chain for Burner Tip II

Figure 10.5.: Complete error chain for burner tip, analogous to fig. 10.2 for the flow swirler part.

11. Discussion

In this chapter, we summarize the content of this thesis and propose possibilities for future improvements. We show benefits and disadvantages of our framework and assess its suitability for practical application.

11.1. Summary of Work

We started this thesis with a short introduction of necessary basics in section 2, which comprised fundamentals of Computed Tomography, including physical and methodical aspects. We also explained the foundations of Reverse Engineering and named some important methods for Additive Manufacturing of metallic materials. In section 3, we subsequently named some preliminary studies and ideas that are similar to our work.

After an explanation of our framework and the measurement chain in sec. 4, we continued our actual work with a first comparison of different procedures available for RE (sec. 5). We were able to conclude that optical scans are significantly better suited to acquire geometric information for areas of the blade of investigation, wherever access is possible. We also showed that Linac-based CTs lack resolution, while low-energetic scans exhibit severe problems to penetrate the material of the blade but enable precise measurements. As a consequence, we splitted the blade into four regions of interest and defined optimal methods for the outer two of them.

Next, we turned to the manufacturing technology of the turbine blade in sec. 6. We investigated the production accuracy and identified critical areas at the surface of the part. We also examined the influence of the layer thickness of the process on the final workpiece. Depending on the manufacturing properties and the region at the final part, we state an approximate production accuracy between $12.7\,\mu m \pm 29.0\,\mu m$ and $54.0\,\mu m \pm 78.1\,\mu m$ (deviation between nominal CAD geometry and results of metrological investigations via optical and CT scan, see sec. 6).

In order to overcome drawbacks for the imaging of inner features of our blade, we suggested two different approaches. Generally, we wish to optimize the signal intensity, which is expressed by the formula of Lambert-Beer (see eq. 2.5):

$$I(\eta) = I_0\, e^{-\mu\eta}\ . \tag{11.1}$$

Since we assume the noise to scale with the intensity at the beginning I_0, it makes no sense to change this value. Instead, an option is to reduce the linear attenuation coefficient μ, which can be accomplished by adjusting photon energy, atomic number or mass density (see sec. 2.2.4). While the latter two imply a change of material – which is practically not feasible – our first approach aims to increase the photon energy while still maintaining a sufficient image resolution. For this, we proposed a DECT method, based on two different CT-scans, that is able

to penetrate even unfavorable materials with sufficient accuracy (see sec. 7; assumed accuracy ranges between 6.3 µm ± 51.8 µm and 34.6 µm ± 88.3 µm in the given example, depending on ROI). An alternative was introduced in sec. 8, where we tried to reduce the X-ray pathway in the workpiece by cutting it into pieces and probing them separately. Our investigation is based on simulations and also revealed sufficient results. While both methods are able to acquire the desired information, neither of them is optimal: in the first case, the price is a prolonged scan time with additional instruments needed and consequently also increased costs. In the second case, the workpiece is destroyed, which is not always feasible in practice.

In section 9, we finally combined our knowledge of former chapters and investigated the complete replication process as such. We used our workflow to generate an accurate mesh of the geometry, manufactured a replica, and subsequently measured it. We assessed the process and potential error sources in detail, quantitatively determined the quality of the replica as well as the original manufacturing method, and identified the most important influence factors. The obtainable quality reaches from 14 µm ± 65 µm for the outer foil to 61 µm ± 61 µm for the inner socket (compared to originally intended design), while almost two third of the deviations of the outer geometry can be derived to the manufacturing of the replica while all factors (i.e. imaging and production process) seem to be almost equally important for inner geometries. The quality differences between original and reverse-engineered range from ca. to µm.

We also conclude that CT is suited very well for RE, but especially the offset values need to be corrected in future. Points of particular interest are better adjustments of the iso-50 % surface determination (or using different percentage values, if necessary) and the suppression of beam hardening and other artifacts. Also, meshing algorithms for precise measurements need to be optimized, since they account for almost half of inaccuracies caused by the Reverse Engineering. In order to show the possibilities and chances of this workflow, we repeated the replication procedure for two additional test pieces in section 10 and again characterized the replication process quantitatively.

In this thesis, we were able to develop and access a replication framework consisting of different RE and AM methods, which is able to fulfill the desired function. Nevertheless, the process is only applicable with certain limitations and can naturally reach a limited but usually sufficient precision, so that future developments are necessary to optimize the workflow.

11.2. Future Prospects

As a matter of fact, the framework proposed in this thesis is not perfect. Further optimizations are beyond the scope of this thesis and need to be addressed in further investigations and studies. Also, many simplifications and reductions were necessary. In the following, we will critically summarize the drawbacks of our method and propose points for further work and improvements.

Also, we want to point out possible limitations and additional areas of application that have not been mentioned so far.

First of all, one needs to bear in mind that all blades of investigation in this thesis are manufactured from a single monomaterial, which is not necessarily the case in reality. Foils are often manufactured from different alloys or coated with a ceramic protection layer. Surface determination of multi-material pieces is a demanding task that has not been investigated for our application so far. We expect that DECT and similar multi-energy scan approaches will prove to be very valuable for such workpieces.

When speaking of surface determination, we have already mentioned problems and drawbacks of the iso-50 % approach in sec. 2.3.2. Depending on the material, adjustments between 35 % and 90 % are better suited for a proper outcome [Kruth et al. 2011]. A common option to determine the ideal iso-value is to adjust it in such a way that it fits the optical scan of the outside where the ideal geometry is precisely known. Nevertheless, such an approach can cause an offset for inner structures (or where no reference measurements are possible) in the object of investigation due to beam hardening, which can cause incorrect results for inner structures. Another possibility – especially for automated scanning lines – is to determine the material in advance and use the iso-value of a test artifact of similar material and geometry that has been previously measured. This approach requires great effort beforehand, since a multitude of different artifacts need to be probed before the surface determination can take place. Since alternatives to the iso-50 %-segmentation are available (for instance a two-step approach that has been proposed by Kasperl et al. (2002)), further investigations in this direction seem reasonable.

In this thesis, only geometric deviations have been investigated. Nevertheless, there are many other parameters that render a turbine blade suitable or not. Such are, for instance, the surface quality (e.g. for fluid- and aerodynamic considerations), manufacturing costs, strength and ductility in service and long-term stability. Also, for the inner structure, the cooling capacity seems more important than fidelity to the original geometry. Even though studies concerning the material properties are available for AM-printed turbine alloys and such blades have been tested before, newly produced replicas does not necessarily exhibit the same properties as the original parts and need to be observed carefully [Ding et al. 2015; Jia and Gu 2014; Kanagarajah et al. 2013; Rickenbacher et al. 2013; Trosch et al. 2016; Wang et al. 2012]. For instance, if several blades of different manufactures are used, displacements of the turbine mass center can be the result, which can lead to undesired side effects up to static failure [Dewangan et al. 2015]. Also, in order to simplify calculations, only the mean shift and standard deviations were considered. Since the distributions are not necessarily perfect Gaussian-shaped, some errors are introduced this way as well. Even though we consider them to be negligible, one needs to bear in mind that the reality can be more complex, especially if smaller ROIs are considered.

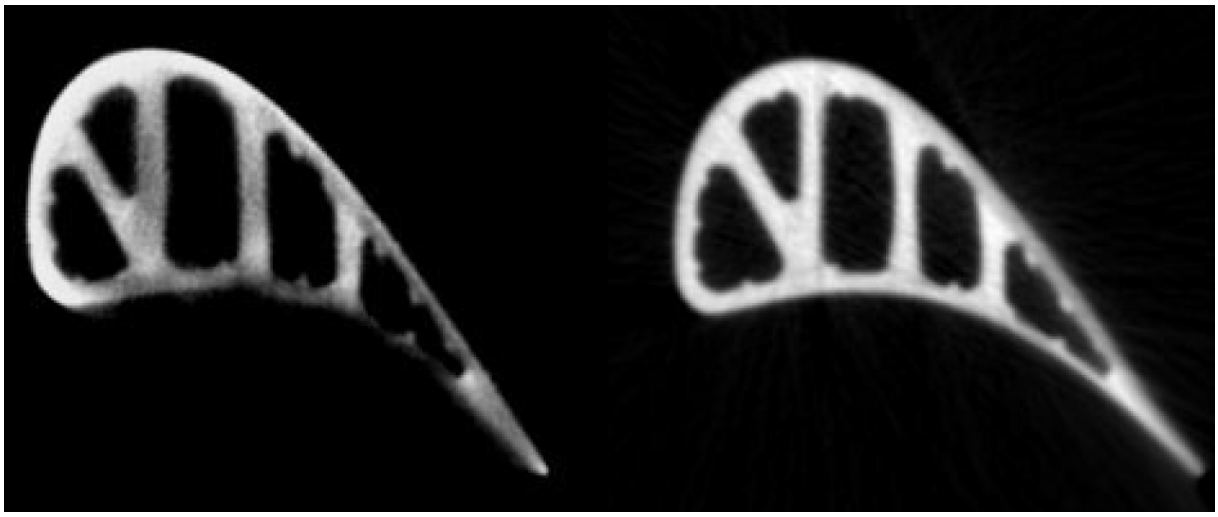

Figure 11.1.: Comparison of two CT slices of a turbine blade, acquired via cone beam (left) and fan beam (right). The image quality of the latter is significantly increased due to reduced influence of scatter radiation [Allen et al. 2005].

The greatest disadvantages of our CT is the evolving scatter radiation and the low acceleration voltage. It has been shown that the results of cone beam systems for aerofoils are relatively poor, especially for the concave side, and that collimated 2D CTs with higher acceleration voltages of ca. 300 keV to 450 keV are capable of obtaining significantly better results (see fig. 11.1). Generally, the reduction of unwanted scatter radiation, for instance, by use of line detector arrays (LDAs) can improve the CNR and image quality considerably. If we take a closer look at the linear attenuation coefficient μ in eq. 11.1, this effect becomes obvious: According to sec. 2.2.4, the coefficient is made up of a fixed material dependent absorption parameter α and a scattered radiation part μ_S, which can be reduced via collimating the X-ray beam. As a tradeoff, the time for a full CT-scan increases remarkably when a collimated setup is used, as shown in fig. 11.2. Nevertheless, this method seems promising, especially if several multi-energy scans are performed simultaneously to reduce the overall scan time. Further alternative methods to minimize the influence of scattering are available, with each strengths and weaknesses. Many of them are software based and can be implemented comparably easily and without prolonging the scan time significantly. Another possibility to increase the image acquisition rate – also for DECT – is to replace the common start-stop movement of the object during CT with a continuous movement, where no time is lost between the acquisition of separate images. Unfortunately, a smooth movement demands conventional micro stepping devices at low speed, so that low exposure times are necessary [Allen et al. 2005]. In order to obtain a sufficient signal, the X-ray tube current must be increased, which also increases the size of the focal spot and thus decreases the final image quality. We conclude that this method to decrease the CT scan time is a rather unsuited approach. Even though methods to accelerate CTs still pose a point open for optimization in the future, we also want to stress that the impact of two scans can be overrated. In particular, if many similar blades are scanned or comparable CAD geometries are available, a

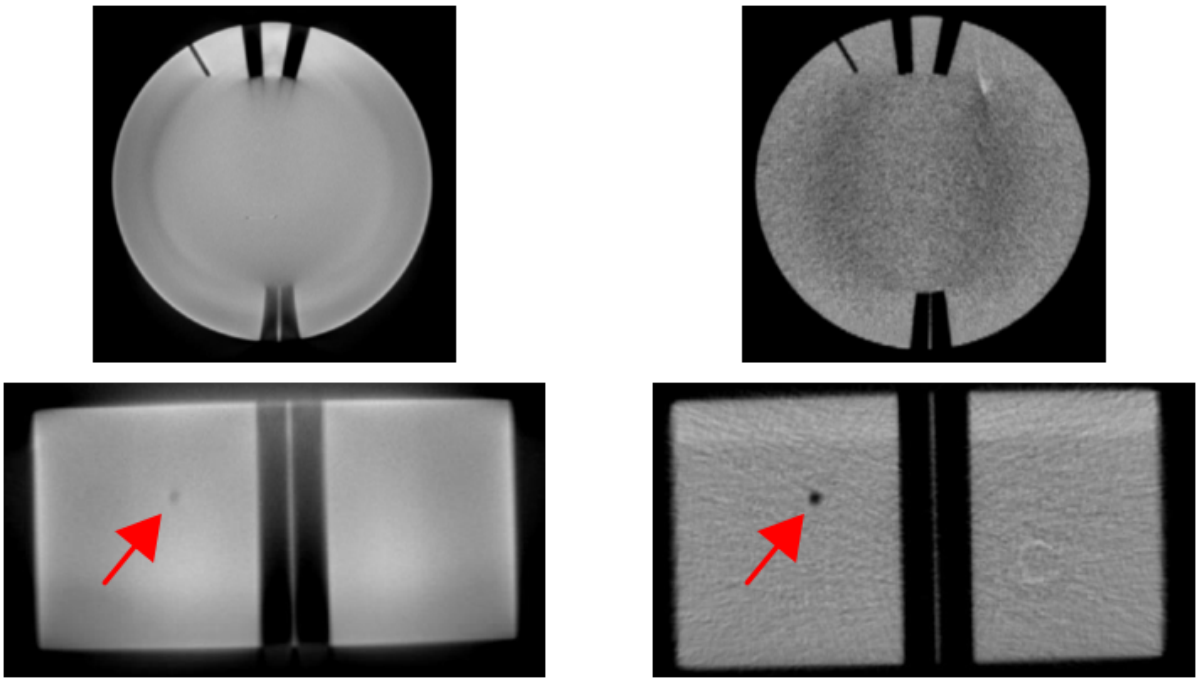

(a) Test Piece Captured via Flat Panel Detector (FPD) With Strong Scatter Artifacts

(b) Test Piece Captured via Line Detector Array (LDA) With Reduced Scatter Artifacts

Figure 11.2.: Top and side view of a test piece obtained by a flat panel detector (fig. 11.2a) and by a line detector array for reduced scattering (fig. 11.2b). The indicated defect is significantly better visible due to improved CNR in the image with fewer scattering. Both images were obtained with 450 keV and 0.4 µm focus spot size. The FPD image features a spatial resolution of 100 µm and a scan time of 54 min while the LDA features a voxel size of 124 µm and a scan time of 5.5 h.

single medium-energy scan can be sufficient to carry out a DECT image fusion for a series of blades, so that only a single scan is necessary for these. Nevertheless, how much these parts are allowed to differ for a proper result is still up to future investigations.

Even though all distance parameters like SOD or SDD are remeasured and calibrated regularly, slight errors cannot be excluded. A method well suited for automatic scanning to decrease the influence of errors, is to scan an artifact simultaneously with each scan whenever enough place is available. Due to the well-known geometry of the artifact, positions and distances at the object of interest can be determined with higher precision.

During our analysis, the finally obtained RE-mesh was not further treated, but printed directly. This will probably also stay the *modus operandi* for easier parts in the future, but for more demanding objects – such as turbine blades – an additional step might be beneficial. Further handling by hand, like for instance, fitting planes or spheres to the geometry may improve fidelity of the final model significantly. Further analysis is necessary to confirm and quantitatively express this assumption. We already showed in sec. 5.6, that the generation of a mesh is linked to a loss of accuracy related to the determined surface. It is also possible that the generated mesh is not watertight enough for subsequent printing and needs to be repaired by additional tools; typical software packages available are, for instance, Netfabb (*Autodesk Corp.*, San Rafael,

USA), Meshlab (developed by *National Research Council*, Italy) or graphite (*Inria Research Institute*, France). Also, the final result of our work is supposed to be a parametrized CAD model, so that the intermediate step of generating a mesh appears to be obsolete. It is more desirable to delegate the calculation of meshes to future improvements. This would slightly improve the accuracy of our outcome, but also decrease the overall processing time and ease the file handling (see also sec. 5.6). So far, no software package (to our knowledge) is able to handle or convert CT-datasets directly into CAD, but further developments might allow this in the future.

Bibliography

AIO Robotics, Inc. (2017): Web Page of Manufacturer, Accessed on 19.5.2017, Available from: http://www.zeus.aiorobotics.com/hardware-features.

Allen, M., Ramsey, A. T., and Asme (2005): Advances in the Computed Tomography of Turbine Blades, Proceedings of the ASME Turbo Expo 2005, Vol 2. Amer Soc Mechanical Engineers, New York.

Angel, J. and De Chiffre, L. (2014): Comparison on Computed Tomography Using Industrial Items, CIRP Annals - Manufacturing Technology, 63(1):473–476, Available from: http://www.sciencedirect.com/science/article/pii/S0007850614000377.

Appleby, J., Mitchell, P. D., Robinson, C., Brough, A., Rutty, G., Harris, R. A., Thompson, D., and Morgan, B. (2014): The Scoliosis of Richard III, last Plantagenet King of England: Diagnosis and Clinical Significance, The Lancet, 383(9932):1944–1945, Available from: http://dx.doi.org/10.1016/S0140-6736(14)60762-5.

Aranda, J. L., Jiménez, M. F., Rodríguez, M., and Varela, G. (2015): Tridimensional Titanium-printed Custom-made Prosthesis for Sternocostal Reconstruction, European Journal of Cardio-Thoracic Surgery, 48(4):e92–e94, Available from: http://dx.doi.org/10.1093/ejcts/ezv265.

Arens, T., Hettlich, F., Karpfinger, C., Kockelkorn, U., Lichtenegger, K., and Stachel, H. (2012): Mathematik, Spektrum Akademischer Verlag, Heidelberg, 2nd edition.

ASTM (2013): American Society for Testing and Materials - ASTM-I F2792 12a - Standard Terminology for Additive Manufacturing Technologies.

Bagci, E. (2009): Reverse Engineering Applications for Recovery of Broken or Worn Parts and Re-manufacturing: Three Case Studies, Advances in Engineering Software, 40(6):407–418, Available from: http://www.sciencedirect.com/science/article/pii/S0965997808001312.

Bardell, D. (2005): The Dawn of Microscopy, The American Biology Teacher, 67(7):392–398, Available from: http://abt.ucpress.edu/content/67/7/392.

Ben, V. and Jean-Pierre, K. (2007): Selective Laser Melting of Biocompatible Metals for Rapid Manufacturing of Medical Parts, Rapid Prototyping Journal, 13(4):196–203, Available from: http://dx.doi.org/10.1108/13552540710776142.

Bi, G. J. and Gasser, A. (2011): Restoration of Nickel-Base Turbine Blade Knife-Edges with Controlled Laser Aided Additive Manufacturing, volume 12 of Physics Procedia, pages 402–409, Elsevier Science Bv, Amsterdam.

Bidanda, B. and Geng, Z. H. (2016): Emerging Trends in Reverse Engineering, pages 2–7, Proceedings of the International Conference on Progress in Additive Manufacturing. Research Publishing Services, Singapore.

Biedermann, M. (2017): Simulation-driven Design for Additive Manufacturing, Master's Thesis, Technical University of Munich, Institut für Werkzeugmaschinen und Betriebswissenschaften, Fakultät für Maschinenwesen.

Bremen, S., Meiners, W., and Diatlov, A. (2012): Selective Laser Melting, Laser Technik Journal, 9(2):33–38, Available from: http://dx.doi.org/10.1002/latj.201290018.

Buzug, T. M. (2008): Computed Tomography, Springer-Verlag, Berlin, Heidelberg, 1st edition, ISBN:978-3-540-39407-5.

Calignano, F., Lorusso, M., Pakkanen, J., Trevisan, F., Ambrosio, E. P., Manfredi, D., and Fino, P. (2017): Investigation of Accuracy and Dimensional Limits of Part Produced in Aluminum Alloy by Selective Laser Melting, International Journal of Advanced Manufacturing Technology, 88(1-4):451–458.

Capture 3D (2017): Web Page of Manufacturer, Accessed on 24.5.2017, Available from: http://www.capture3d.com/3d-metrology-solutions/3d-scanners/atos-triple-scan.

Carter, T. J. (2005): Common Failures in Gas Turbine Blades, Engineering Failure Analysis, 12(2):237–247.

Chotas, H. G., Dobbins, J. T., and Ravin, C. E. (1999): Principles of Digital Radiography with Large-Area, Electronically Readable Detectors: A Review of the Basics, Radiology, 210(3):595–599, Available from: http://dx.doi.org/10.1148/radiology.210.3.r99mr15595.

Cooper, D., Thornby, J., Blundell, N., Henrys, R., Williams, M. A., and Gibbons, G. (2015): Design and Manufacture of High Performance Hollow Engine Valves by Additive Layer Manufacturing, Materials & Design, 69:44–55, Available from: http://www.sciencedirect.com/science/article/pii/S0261306914009376.

Crété-Roffet, F., Dolmiere, T., Ladret, P., and Nicolas, M. (2007): The Blur Effect: Perception and Estimation With a New No-reference Perceptual Blur Metric, SPIE Electronic Imaging Symposium Conf Human Vision and Electronic Imaging, 12:EI–6492.

Curodeau, A., Sachs, E., and Caldarise, S. (2000): Design and Fabrication of Cast Orthopedic Implants with Freeform Surface Textures from 3D Printed Ceramic Shell, Journal of Biomedical Materials Research, 53(5):525–535, Available from: http://dx.doi.org/10.1002/1097-4636(200009)53:5<525::AID-JBM12>3.0.CO;2-1.

De Chiffre, L., Carmignato, S., Kruth, J. P., Schmitt, R., and Weckenmann, A. (2014): Industrial Applications of Computed Tomography, CIRP Annals - Manufacturing Technology, 63(2):655–677, Available from: http://www.sciencedirect.com/science/article/pii/S0007850614001930.

De Laurentis, Kathryn, J. and Mavroidis, C. (2002): Mechanical Design of a Shape Memory Alloy Actuated Prosthetic Hand, Technology and Health Care, 10(2):91–106.

Dewangan, R., Patel, J., Dubey, J., Sen, P. K., and Bohidar, S. K. (2015): Gas Turbines Blades —- a Critical Review of Failure on First and Second Stages, Int. J. Mech. Eng. Robot. Res, 4:216–232.

Dewulf, W., Tan, Y., and Kiekens, K. (2012): Sense and Non-sense of Beam Hardening Correction in CT Metrology, CIRP Annals - Manufacturing Technology, 61(1):495–498, Available from: http://www.sciencedirect.com/science/article/pii/S0007850612000157.

Ding, R. G., Huang, Z. W., Li, H. Y., Mitchell, I., Baxter, G., and Bowen, P. (2015): Electron Microscopy Study of Direct Laser Deposited IN718, Materials Characterization, 106:324–337, Available from: http://www.sciencedirect.com/science/article/pii/S1044580315002235.

Eden, K. and Gebhard, H. (2014): Dokumentation in der Mess- und Prüftechnik, Springer Vieweg, Wiesbaden, 2nd edition, ISBN: 978-3-658-06113-5.

Ehrig, K., Staude, A., Goebbels, J., Bartscher, M., Koch, M., and Neukamm, M. (2010): Evaluierung von Testkörpern zur Strahlaufhärtungskorrektur beim dimensionellen Messen mit Computertomographie, Industrielle Computertomografie Tagung (Proceedings), pages 181–186, Available from: https://opus4.kobv.de/opus4-bam/frontdoor/index/index/docId/22033.

Eiríksson, E. R., Wilm, J., Pedersen, D. B., and Aanæs, H. (2015): Precision and Accuracy Parameters in Structured Light 3-D Scanning, International Archives of the Photogrammetry, Remote Sensing & Spatial Information Sciences, Volume XL-5/W8.

Encyclopædia Britannica (2017): Electromagnetic Spectrum, Accessed on 15.5.2017, Available from: https://www.britannica.com/science/electromagnetic-spectrum.

Fan, H., Fu, J., Li, X., Pei, Y., Li, X., Pei, G., and Guo, Z. (2015): Implantation of Customized 3D Printed Titanium Prosthesis in Limb Salvage Surgery: a Case Series and Review of the Literature, World Journal of Surgical Oncology, 13:308, Available from: http://www.ncbi.nlm.nih.gov/pmc/articles/PMC4632365/.

Fischer, A. (2000): Multi-level Models for Reverse Engineering and Rapid Prototyping in Remote CAD Systems, Computer-Aided Design, 32(1):27–38.

FLUX, Inc. (2017): Web Page of Manufacturer, Accessed on 19.5.2017, Available from: https://flux3dp.com/delta-plus/.

Gameros, A., De Chiffre, L., Siller, H. R., Hiller, J., and Genta, G. (2015): A Reverse Engineering Methodology for Nickel Alloy Turbine Blades with Internal Features, CIRP Journal of Manufacturing Science and Technology, 9:116–124, Available from: http://www.sciencedirect.com/science/article/pii/S1755581714000613.

Geng, Z. and Bidanda, B. (2017): Review of Reverse Engineering Systems -– Current State of the Art, Virtual and Physical Prototyping, pages 1–12, Available from: http://dx.doi.org/10.1080/17452759.2017.1302787.

Ghani, S. A. C., Zakaria, M. H., Harun, W. S. W., and Zaulkafilai, Z. (2017): Dimensional Accuracy of Internal Cooling Channel Made by Selective Laser Melting (SLM) And Direct Metal Laser Sintering (DMLS) Processes in Fabrication of Internally Cooled Cutting Tools, volume 90 of MATEC Web of Conferences, E D P Sciences, Cedex A.

Giamei, A. F. (2013): Development of Single Crystal Superalloys: A Brief History, Advanced Materials and Processes, 171(9):26–30.

Giampaolo, T. (2006): Gas Turbine Handbook: Principles and Practices, The Fairmont Press, Inc., Lilburn, 3rd edition, ISBN: 9780881735154.

Girardeau, J., Pailhes, J., Sebastian, P., Pardo, F., and Nadeau, J.-P. (2013): Turbine Blade Cooling System Optimization, Journal of Turbomachinery, 135(6):061020–061020–13, Available from: http://dx.doi.org/10.1115/1.4023466.

Guni, E. (2012): Untersuchung von CdTe als Sensormaterial für die spektroskopische Röntgenbildgebung, PhD Thesis, Friedrich-Alexander-Universität Erlangen-Nürnberg.

Hanke, R. (2010): Computertomographie in der Materialprüfung - Stand der Technik und aktuelle Entwicklungen, DGZfP-Jahrestagung 2010.

Heinzl, C., Kastner, J., and Groller, E. (2007): Surface Extraction From Multi-material Components for Metrology Using Dual Energy CT, IEEE Trans Vis Comput Graph, 13(6):1520–7, Available from: https://www.ncbi.nlm.nih.gov/pubmed/17968105.

Herzog, D., Seyda, V., Wycisk, E., and Emmelmann, C. (2016): Additive Manufacturing of Metals, Acta Materialia, 117:371–392, Available from: http://www.sciencedirect.com/science/article/pii/S1359645416305158.

Hounsfield, G. N. (1973): Computerized Transverse Axial Scanning (Tomography): Part 1. Description of System, The British Journal of Radiology, 46(552):1016–1022, Available from: https://doi.org/10.1259/0007-1285-46-552-1016.

Hunter, A. K. and McDavid, W. D. (2012): Characterization and Correction of Cupping Effect Artefacts in Cone Beam CT, Dentomaxillofacial Radiology, 41(3):217–223, Available from: http://www.ncbi.nlm.nih.gov/pmc/articles/PMC3520295/.

Imanishi, J. and Choong, P. F. M. (2015): Three-dimensional Printed Calcaneal Prosthesis Following Total Calcanectomy, International Journal of Surgery Case Reports, 10:83–87, Available from: http://www.ncbi.nlm.nih.gov/pmc/articles/PMC4429954/.

Jamieson, R. and Hacker, H. (1995): Direct Slicing of CAD Models for Rapid Prototyping, Rapid Prototyping Journal, 1(2):4–12.

Jardini, A. L., Larosa, M. A., Filho, R. M., Zavaglia, C. A. d. C., Bernardes, L. F., Lambert, C. S., Calderoni, D. R., and Kharmandayan, P. (2014): Cranial Reconstruction: 3D Biomodel and Custom-built Implant Created Using Additive Manufacturing, Journal of Cranio-Maxillofacial Surgery, 42(8):1877–1884, Available from: http://www.sciencedirect.com/science/article/pii/S1010518214002303.

Jia, Q. B. and Gu, D. D. (2014): Selective Laser Melting Additive Manufacturing of Inconel 718 Superalloy Parts: Densification, Microstructure and Properties, Journal of Alloys and Compounds, 585:713–721.

Kalender, W. A. (2006): X-ray Computed Tomography, Physics in Medicine and Biology, 51(13):R29, Available from: http://stacks.iop.org/0031-9155/51/i=13/a=R03.

Kanagarajah, P., Brenne, F., Niendorf, T., and Maier, H. J. (2013): Inconel 939 Processed by Selective Laser Melting: Effect of Microstructure and Temperature on the Mechanical Properties Under Static and Cyclic Loading, Materials Science and Engineering a-Structural Materials Properties Microstructure and Processing, 588:188–195.

Kasperl, S., Bauscher, I., Hassler, U., Markert, H., and Schröpfer, S. (2002): Artefaktreduzierung in der industriellen 3D Computertomographie (CT), DGZfP Jahrestagung, Available from: http://www.ndt.net/article/dgzfp02/papers/v38/v38.htm.

Kolkoori, S., Wrobel, N., Deresch, A., Redmer, B., and Ewert, U. (2014): Dual High-Energy X-ray Digital Radiography for Material Discrimination in Cargo Containers, 11th European Conference on Non-Destructive Testing (ECNDT 2014).

Kramme, R. (2011): Medizintechnik, Springer-Verlag, Berlin, Heidelberg, New York, 4th edition, ISBN: 978-3-642-16186-5.

Kruth, J. P., Bartscher, M., Carmignato, S., Schmitt, R., De Chiffre, L., and Weckenmann, A. (2011): Computed Tomography for Dimensional Metrology, CIRP Annals - Manufacturing Technology, 60(2):821–842, Available from: http://www.sciencedirect.com/science/article/pii/S0007850611002083.

Kueh, A., Warnett, J. M., Gibbons, G. J., Brettschneider, J., Nichols, T. E., Williams, M. A., and Kendall, W. S. (2016): Modelling the Penumbra in Computed Tomography, Journal of X-Ray Science and Technology, 24(4):583–597, Available from: http://www.ncbi.nlm.nih.gov/pmc/articles/PMC4969716/.

Kwak, J. S. and Han, J.-C. (2003): Heat Transfer Coefficients and Film Cooling Effectiveness on the Squealer Tip of a Gas Turbine Blade, Journal of Turbomachinery, 125(4):648–657, Available from: http://dx.doi.org/10.1115/1.1622712.

Körner, M., Weber, C. H., Wirth, S., Pfeifer, K.-J., Reiser, M. F., and Treitl, M. (2007): Advances in Digital Radiography: Physical Principles and System Overview, RadioGraphics, 27(3):675–686, Available from: https://doi.org/10.1148/rg.273065075.

Lachmayer, R., Lippert, R. B., and Fahlbusch, T. (2016): 3D-Druck beleuchtet - Additive Manufacturing auf dem Weg in die Anwendung, Springer Berlin Heidelberg, Berlin, Heidelberg.

Langston, L. S. and Opdyke, G. (1997): Introduction to Gas Turbines for Non-Engineers, Global Gas Turbine News, 37(2).

Lee, K. H. and Woo, H. (2000): Direct Integration of Reverse Engineering and Rapid Prototyping, Computers & Industrial Engineering, 38(1):21–38.

Levy, G. N., Schindel, R., and Kruth, J. P. (2003): Rapid Manufacturing and Rapid Tooling with Layer Manufacturing (LM) Technolgies, State of the Art and Future Perspectives, CIRP Annals - Manufacturing Technology, 52(2):589–609, Available from: http://www.sciencedirect.com/science/article/pii/S0007850607602066.

Lorensen, W. E. and Cline, H. E. (1987): Marching Cubes: A high Resolution 3D Surface Construction Algorithm, ACM Siggraph Computer Graphics, 21:163–169.

Lowenthal, G. and Airey, P. (2001): Practical Applications of Radioactivity and Nuclear Radiations, Cambridge University Press, Cambridge, 1st edition.

Ma, D., Lin, F., and Chua, C. K. (2001): Rapid Prototyping Applications in Medicine. Part 2: STL File Generation and Case Studies, International Journal of Advanced Manufacturing Technology, 18(2):118–127.

Magerramova, L., Vasilyev, B., Kinzburskiy, V., and Asme (2016): Novel Designs of Turbine Blades for Additive Manufacturing, Proceedings of the Asme Turbo Expo: Turbine Technical Conference and Exposition, 2016, Vol 5c. Amer Soc Mechanical Engineers, New York.

Mankovich, Nicholas, J., Cheeseman, Andrew, M., and Stoker Noel, G. (1990): The Display of Three-dimensional Anatomy with Stereolithographic Models, Journal of Digital Imaging, 3(3):200–203.

Martelli, N., Serrano, C., van den Brink, H., Pineau, J., Prognon, P., Borget, I., and El Batti, S. (2016): Advantages and Disadvantages of 3-dimensional Printing in Surgery: A Systematic Review, Surgery, 159(6):1485–1500, Available from: http://dx.doi.org/10.1016/j.surg.2015.12.017.

Martz, H. E. J., Glenn, S. M., Smith, J. A., Divin, C. J., and Azevedo, S. G. (2016): Poly- versus Mono-energetic Dual-spectrum Non-intrusive Inspection of Cargo Containers, IEEE Transactions on Nuclear Science, PP(99).

Mazur, Z., Luna-Ramírez, A., Juárez-Islas, J. A., and Campos-Amezcua, A. (2005): Failure Analysis of a Gas Turbine Blade made of Inconel 738LC Alloy, Engineering Failure Analysis, 12(3):474–486, Available from: http://www.sciencedirect.com/science/article/pii/S135063070400113X.

Medellin-Castillo, H. I., Torres, J. E. P., and Asme (2010): Rapid Prototyping and Manufacturing: A Review of Current Technologies, Imece 2009, Vol 4. Amer Soc Mechanical Engineers, New York, ISBN: 978-0-7918-4377-2.

Mendricky, R. (2015): Analysis of Measurement Accuracy of Contactless 3D Optical Scanners, MM Science Journal, 2015:1565–1572.

Mohaghegh, K., Sadeghi, M. H., and Abdulla, A. (2007): Reverse Engineering of Turbine Blades Based on Design Intent, International Journal of Advanced Manufacturing Technology, 32(9-10):1009–1020.

Mok, S.-W., Nizak, R., Fu, S.-C., Ho, K.-W. K., Qin, L., Saris, D. B. F., Chan, K.-M., and Malda, J. (2016): From the Printer: Potential of Three-dimensional Printing for Orthopaedic Applications, Journal of Orthopaedic Translation, 6:42–49, Available from: http://www.sciencedirect.com/science/article/pii/S2214031X16300031.

Márquez, A., Venturino, P., De Bona, J., and Campetti, G. (2012): Failure Analyses of Two Gas Turbine Wheels, Procedia Materials Science, 1:281–288, Available from: http://www.sciencedirect.com/science/article/pii/S2211812812000399.

NIST (2017): Web Database of the National Institute of Standards and Technology, Accessed on 22.8.2017, Available from: https://physics.nist.gov/PhysRefData/XrayMassCoef/ElemTab/z26.html,https://physics.nist.gov/cgi-bin/Star/compos.pl?matno=026.

Nowotny, S., Thieme, S., Albert, D., Kubisch, F., Kager, R., and Leyens, C. (2013): Generative Manufacturing and Repair of Metal Parts through Direct Laser Deposition Using Wire Material, pages 185–189, Springer Berlin Heidelberg, Berlin, Heidelberg, Available from: http://dx.doi.org/10.1007/978-3-642-41329-2_20.

Overton, T. W. (2014): 3D-Printed Turbine Replacement Parts Could Cut Repair Times by 90 Percent, Power, 158(4):20.

Panos, K. (2007): Kraftwerke, Technik und Kosten, pages 215–282, Springer Berlin Heidelberg, Berlin, Heidelberg, ISBN: 978-3-540-35379-9, Available from: https://doi.org/10.1007/978-3-540-35379-9_7.

Parthasarathy, J. (2014): 3D Modeling, Custom Implants and its Future Perspectives in Craniofacial Surgery, Annals of Maxillofacial Surgery, 4(1):9–18, Available from: http://www.ncbi.nlm.nih.gov/pmc/articles/PMC4073471/.

Pearson, E., Pan, X. C., and Pelizzari, C. (2015): Dual-energy (MV/kV) CT With Probabilistic Attenuation Mapping for IGRT Applications, volume 9412 of Proceedings of SPIE, Spie-Int Soc Optical Engineering, Bellingham.

Pelli, D. G. and Bex, P. (2013): Measuring Contrast Sensitivity, Vision Research, 90:10–14, Available from: http://www.sciencedirect.com/science/article/pii/S0042698913001132.

Philipp, K. and Albert, W. (2010): Multi-energy Image Stack Fusion in Computed Tomography, Measurement Science and Technology, 21(4):045105, Available from: http://stacks.iop.org/0957-0233/21/i=4/a=045105.

Qiu, J., Gu, X.-y., Xiong, Y.-y., and Zhang, F.-q. (2011): Nasal Prosthesis Rehabilitation Using CAD-CAM Technology After Total Rhinectomy: a Pilot Study, Supportive Care in Cancer, 19(7):1055, Available from: https://doi.org/10.1007/s00520-011-1157-1.

Raja, V. and Fernandes, K. J. (2008): Reverse Engineering - An Industrial Perspective, Springer-Verlag, London, 1st edition, ISBN: 978-1-84628-855-5.

Rengier, F., Mehndiratta, A., von Tengg-Kobligk, H., Zechmann, C. M., Unterhinninghofen, R., Kauczor, H. U., and Giesel, F. L. (2010): 3D printing Based on Imaging Data: Review of Medical Applications, International Journal of Computer Assisted Radiology and Surgery, 5(4):335–341, Available from: http://dx.doi.org/10.1007/s11548-010-0476-x.

Rickenbacher, L., Etter, T., Hovel, S., and Wegener, K. (2013): High Temperature Material Properties of IN738LC Processed by Selective Laser Melting (SLM) Technology, Rapid Prototyping Journal, 19(4):282–290.

Saijo, H., Igawa, K., Kanno, Y., Mori, Y., Kondo, K., Shimizu, K., Suzuki, S., Chikazu, D., Iino, M., Anzai, M., Sasaki, N., Chung, U.-i., and Takato, T. (2009): Maxillofacial Reconstruction Using Custom-made Artificial Bones Fabricated by Inkjet Printing Technology, Journal of Artificial Organs, 12(3):200–205, Available from: http://dx.doi.org/10.1007/s10047-009-0462-7.

Salamon, M., Hanke, R., Krüger, P., Uhlmann, N., and Voland, V. (2008): Realization of a Computed Tomography Setup to Achieve Resolutions Below One Micrometer, Nuclear Instruments and Methods in Physics Research Section A: Accelerators, Spectrometers, Detectors and Associated Equipment, 591(1):50–53, Available from: http://www.sciencedirect.com/science/article/pii/S0168900208003999.

Savio, E., De Chiffre, L., and Schmitt, R. (2007): Metrology of Freeform Shaped Parts, CIRP Annals-Manufacturing Technology, 56(2):810–830.

Scarfe, W. C. and Farman, A. G. (2008): What is Cone-Beam CT and How Does it Work?, Dental Clinics of North America, 52(4):707–730, Available from: http://www.sciencedirect.com/science/article/pii/S001185320800044X.

Schiebold, K. (2015): Zerstörungsfreie Werkstoffprüfung - Durchstrahlungsprüfung, Springer Vieweg, Berlin, Heidelberg, 1st edition, ISBN: 978-3-662-44668-3.

Schrapp, M. and Goldammer, M. (2013): Artefaktreduktion in der industriellen Computertomographie mithilfe zusätzlicher Oberflächeninformationen, Berichtsband DGZfP-Jahrestagung, Dresden.

Schrapp, M., Goldammer, M., Schörner, K., and Stephan, J. (2014a): Improvement of Image Quality in Computed Tomography via Data Fusion, In Proceedings of the 5th International Conference on Industrial Computed Tomography (iCT), pages 283–289.

Schrapp, M., Goldammer, M., Stephan, J., Chimenti, D. E., Bond, L. J., and Thompson, D. O. (2014b): Artifact Reduction in Industrial Computed Tomography via Data Fusion, AIP Conference Proceedings, 1581(1):1961–1966, Available from: http://aip.scitation.org/doi/abs/10.1063/1.4865064.

Schrapp, M. J. (2015): Multi Modal Data Fusion in Industrial X-ray Computed Tomography, PhD Thesis, Technical University of Munich.

Schörner, K. (2012): Development of Methods for Scatter Artifact Correction in Industrial X-ray Cone-beam Computed Tomography, PhD Thesis, Technical University Munich.

Sedlmair, M. U. (2009): Dual-Energy CT: Physikalische Modelle und Anwendungen, PhD Thesis, Ludwig-Maximilians-Universität München.

Shafiee, A. and Atala, A. (2016): Printing Technologies for Medical Applications, Trends in Molecular Medicine, 22(3):254–265, Available from: http://dx.doi.org/10.1016/j.molmed.2016.01.003.

Shah, P., Racasan, R., and Bills, P. (2016): Comparison of Different Additive Manufacturing Methods Using Computed Tomography, Case Studies in Nondestructive Testing and Evaluation, 6:69–78, Available from: http://www.sciencedirect.com/science/article/pii/S2214657116300260.

Shitarev, I., Smelov, V., and Sotov, A. (2014): Repair of a Gas Turbine Blade Tip by Impulse Laser Build-Up Welding, Applied Mechanics and Materials, 682(11):96–99.

Shultis, J. K. and Faw, R. E. (2002): Fundamentals of Nuclear Science and Engineering, Marcel Dekker Inc., New York, ISBN: 9780824708344.

Sidwell, C. V., Darmofal, D. L., and Epstein, A. H. (2004): On the Impact of Variability and Assembly on Turbine Blade Cooling Flow and Oxidation Life, Thesis, Massachusetts Institute of Technology, Available from: http://hdl.handle.net/1721.1/17814.

Siemens AG (2015): CERA - User Manual Version 3.0.

Siemens AG (2017): Web Page of Manufacturer, Accessed on 23.6.2017, Available from: https://www.siemens.com/global/en/home/products/energy/power-generation/gas-turbines/sgt5-8000h.html#!/.

Staffa, G., Barbanera, A., Faiola, A., Fricia, M., Limoni, P., Mottaran, R., Zanotti, B., and Stefini, R. (2012): Custom Made Bioceramic Implants in Complex and Large Cranial Reconstruction: A two-year Follow-up, Journal of Cranio-Maxillo-Facial Surgery, 40(3):e65–e70, Available from: http://dx.doi.org/10.1016/j.jcms.2011.04.014.

Stegemann, D. (1995): Zerstörungsfreie Prüfverfahren - Radiografie und Radioskopie, Teubner Verlag, Stuttgart, ISBN: 978-3-519-06355-1.

Subburaj, K., Nair, C., Rajesh, S., Meshram, S. M., and Ravi, B. (2007): Rapid Development of Auricular Prosthesis Using CAD and Rapid Prototyping Technologies, International Journal of Oral and Maxillofacial Surgery, 36(10):938–943, Available from: http://dx.doi.org/10.1016/j.ijom.2007.07.013.

Sun, J. and Zhang, F.-Q. (2012): The Application of Rapid Prototyping in Prosthodontics, Journal of Prosthodontics, 21(8):641–644, Available from: http://dx.doi.org/10.1111/j.1532-849X.2012.00888.x.

Sun, W., Beown, S., and Leach, R. (2012): An Overview of Industrial X-ray Computed Tomography, National Physical Laboratory (NPL) Report ENG 32, Available from: http://www.academia.edu/33366374/An_overview_of_industrial_X-ray_computed_tomography.

Taina, I. A., Heck, R. J., and Elliot, T. R. (2008): Application of X-ray Computed Tomography to Soil Science: A Literature Review, Canadian Journal of Soil Science, 88(1):1–19, Available from: https://doi.org/10.4141/CJSS06027.

Teeter, M. G., Kopacz, A. J., Nikolov, H. N., and Holdsworth, D. W. (2014): Metrology Test Object for Dimensional Verification in Additive Manufacturing of Metals for Biomedical Applications, Proceedings of the Institution of Mechanical Engineers, Part H: Journal of Engineering in Medicine, 229(1):20–27, Available from: http://dx.doi.org/10.1177/0954411914565222.

Thompson, A., Maskery, I., and Leach, R. K. (2016): X-ray Computed Tomography for Additive Manufacturing: a Review, Measurement Science and Technology, 27(7):072001, Available from: http://stacks.iop.org/0957-0233/27/i=7/a=072001.

Trosch, T., Strossner, J., Yolkl, R., and Glatzel, U. (2016): Microstructure and Mechanical Properties of Selective Laser Melted Inconel 718 Compared to Forging and Casting, Materials Letters, 164:428–431.

Tsuji, M., Noguchi, N., Ihara, K., Yamashita, Y., Shikimori, M., and Goto, M. (2004): Fabrication of a Maxillofacial Prosthesis Using a Computer-Aided Design and Manufacturing System,

Journal of Prosthodontics, 13(3):179–183, Available from: http://dx.doi.org/10.1111/j.1532-849X.2004.04029.x.

Turbell, H. (2001): Cone-Beam Reconstruction Using Filtered Backprojection, PhD Thesis, Linköpings Universitet.

Usher, A. P. (1929): A History of Mechanical Inventions, McGraw-Hill Book Company, New York, ISBN: 978-0486255934, Available from: https://archive.org/details/historyofmechani00ushe.

Van Grieken, R. and Markowicz, A. (2001): Handbook of X-Ray Spectrometry, Practical Spectroscopy. CRC Press, 2nd edition, ISBN: 978-0-203-90870-9.

VDI/VDE-2634 (2012): Verein Deutscher Ingenieure/Verband der Elektrotechnik, Elektronik, Informationstechnik: VDI/VDE 2634 - Optische 3-D-Messsysteme, Beuth Verlag.

Várady, T., Martin, R. R., and Cox, J. (1997): Reverse Engineering of Geometric Models —- an Introduction, Computer-Aided Design, 29(4):255–268, Available from: http://www.sciencedirect.com/science/article/pii/S0010448596000541.

Wang, Z. M., Guan, K., Gao, M., Li, X. Y., Chen, X. F., and Zeng, X. Y. (2012): The Microstructure and Mechanical Properties of Deposited-IN718 by Selective Laser Melting, Journal of Alloys and Compounds, 513:518–523.

Weckenmann, A., Jiang, X., Sommer, K. D., Neuschaefer-Rube, U., Seewig, J., Shaw, L., and Estler, T. (2009): Multisensor Data Fusion in Dimensional Metrology, CIRP Annals - Manufacturing Technology, 58(2):701–721, Available from: http://www.sciencedirect.com/science/article/pii/S0007850609001759.

Wiacker, H. (1991): Dimensionsanalyse mit der Computertomographie am Beispiel Turbinenschaufenvermessung, Vorträge des 2. Seminars Computertomografie, pages 56–93.

Wong, K. C. (2016): 3D-printed Patient-specific Applications in Orthopedics, Dovepress - Orthopedic Research and Reviews, 2016(8):57–66.

Wong, K. C., Kumta, S. M., Geel, N. V., and Demol, J. (2015): One-step Reconstruction With a 3D-printed, Biomechanically Evaluated Custom Implant After Complex Pelvic Tumor Resection, Computer Aided Surgery, 20(1):14–23, Available from: http://dx.doi.org/10.3109/10929088.2015.1076039.

Wu, G., Zhou, B., Bi, Y., and Zhao, Y. (2007): Selective Laser Sintering Technology for Customized Fabrication of Facial Prostheses, Journal of Prosthetic Dentistry, 100(1):56–60, Available from: http://dx.doi.org/10.1016/S0022-3913(08)60138-9.

X-ray WorX (2017): Web Page of Manufacturer, Accessed on 17.5.2017, Available from: http://www.x-ray-worx.com/x-ray-worx/index.php/mikrofokus-roentgenroehren-produktuebersicht/mikrofokus-technologie.

XYZprinting, Inc. (2017): Web Page of Manufacturer, Accessed on 19.5.2017, Available from: http://eu.xyzprinting.com/eu_de/Product/da-Vinci-1.0-Professional3in1.

Yaffe, M. J. and Rowlands, J. A. (1997): X-ray Detectors for Digital Radiography, Phys Med Biol., 42(1):1–39.

Yan, X., Chen, X., Sun, R., Deng, Y., Lin, L., and Nie, J. (2014): Investigation on Material's Fatigue Property Variation Among Different Regions of Directional Solidification Turbine Blades —- Part I: Fatigue Tests on Full Scale Blades, Journal of Engineering for Gas Turbines and Power, 136(10):102502–102502–8, Available from: http://dx.doi.org/10.1115/1.4027928.

Yan, X. and Gu, P. (1996): A Review of Rapid Prototyping Technologies and Systems, Computer-Aided Design, 28(4):307–318.

Yang, M., Virshup, G., Clayton, J., Zhu, X. R., Mohan, R., and Dong, L. (2011): Does kV-MV Dual-energy Computed Tomography Have an Advantage in Determining Proton Stopping Power Ratios in Patients?, Phys Med Biol, 56(14):4499–515, Available from: https://www.ncbi.nlm.nih.gov/pubmed/21719949.

Ávila, C., López, G., Marín, G., Salazar, L., Miranda, Z., González, J., and Brenes, B. (2016): Use of Emerging 3D Printing and Modeling Technologies in the Health Domain, pages 86–98, Springer International Publishing, Cham, Available from: http://dx.doi.org/10.1007/978-3-319-48746-5_10.

List of Figures

1.1. Schematic Structure of the Entire Master's Thesis 3

2.1. Typical Buildup of a Gas Turbine 5
2.2. Sketch of Tubine Blade With Nomenclature 6
2.3. Typical Workflow for a Cone Beam CT 8
2.4. Overview of the Electromagnetic Spectrum 9
2.5. Geometric Influence of the Focal Spot Size 10
(a). Projection with Large Focus 10
(b). Projection with Small Focus 10
(c). Geometric Influence of Large Focus 10
(d). Geometric Influence of Small Focus 10
2.6. Cross Section of an X-ray Tube 11
2.7. Typical X-ray Tube Emission Spectrum 12
2.8. Composition of the Linear Attenuation Coefficient for Iron 14
2.9. Schematic Attenuation of X-rays 16
2.10. Internal Structure of a Scintillation Detector 17
2.11. Object, Radon and Fourier Space and Related Connections 20
2.12. Complete Workflow for Filtered Backprojection 20
2.13. Beam Hardening and Cupping Artifacts 21
(a). Without Beam Hardening Correction 21
(b). With Beam Hardening Correction 21
2.14. Example for an Artifact Caused by Limited Penetration 23
(a). X-ray Pathways of Various Length 23
(b). Result in Reconstructed Volume 23
2.15. Iso-50 % Segmentation Graph 27
2.16. Error Propagation in the Reverse Engineering Workflow 30
2.17. Build-up of a SLM System 32

3.1. Examples for Preliminary Combined Use of RE and AM 35

4.1. The SLM-manufactured Turbine Blade for Our Investigations 39
4.2. Used Machine Setup for Computed Tomography 40

5.1. Location of All Four ROIs 44
(a). The Outer and Inner Geometry of the Foil 44
(b). The Outer and Inner Geometry of the Socket 44
(c). All four ROIs seen from the Side 44

(d). Overview seen from the Front 44
5.2. Surface Comparison of the Optical Scan to the CAD-Model 46
5.3. Geometric Distortion of the Blade due to Manufacturing 47
(a). Deviation Analysis by VGStudio 47
(b). Side Pocket of the Blade 47
5.4. Geometric Distortions at the Chamfers 47
5.5. Comparison of Different CT-Scans of the Foil 49
(a). 225 keV-Scan of the Foil 49
(b). 450 keV-Scan of the Foil 49
(c). Linac-Scan of the Foil 49
(d). CAD-Geometry of the Foil 49
5.6. Comparison of CT-Scans for the Socket Part 50
(a). 225 keV-Scan of the Socket 50
(b). 450 keV-Scan of the Socket 50
(c). Linac-Scan of the Socket 50
(d). CAD-Geometry of the Socket 50
5.7. Surface Comparisons of Different CTs to the Optical Scan 51
5.8. Inner Structure Comparison of Different CTs to the CAD Geometry 53
5.9. Visual Comparison of Concave and Convex Foil Sides 55
5.10. Comparison of Convex and Concave Foil Sides to the Optical Scan 56
5.11. Comparison of Inner Features in Different Scans 57
(a). Inner Structure in CAD 57
(b). Inner Structure in 225 keV-Scan 57
(c). Inner Structure in 450 keV-Scan 57
(d). Inner Structure in Linac-Scan 57
5.12. Comparison of Meshed to Original Geometry 58

6.1. Deviations of Optical Scans to the CAD Geometry 60
6.2. Deviations Between Both Optical Scans 61
6.3. Visual Comparison of Both Blades 62
6.4. Deviation of DECT Scans to Inner CAD Geometry 63
6.5. Comparison of the Inner Structure Between Both Blade by Use of DECT . . . 64

7.1. Workflow for Our DECT Approach 68
7.2. Comparison to the Outer Geometry of Various CT Approaches Including DECT 69
7.3. Comparison to the Inner Geometry of Various CT Approaches Including DECT 69
7.4. Workflow for our DECT Approach and Comparison to 225 keV-Scan 70
(a). Raw Scan Data From 225 keV-Scan 70

(b). Conventional Segmentation Approach 70
(c). Contour of the 450 keV-Scan With Indicated Search Distance 70
(d). Final Outcome After DECT Surface Extraction 70
7.5. Investigations for Robustness Concerning Geometry Shifts 72

8.1. Comparison of the Michelson Contrast in Different Areas of Interest 74
8.2. Typical Socket Slices of the Destructive Testing Approach 76
(a). Simulated Socket Slice 76
(b). Definition of ROIs for Investigation 76
(c). 45°-cutted Slice 76
(d). 315°-cutted Slice 76

9.1. Overview Of All Three Manufactured Blades. 78
9.2. Overview of the Entire Replication Chain 79
9.3. Comparison of CT and Optical Data of the Surfaces for Both Blades 81
9.4. Complete Error Chain for the Outside Socket Part 82
9.5. Complete Error Chain for the Outside Foil Part 83
9.6. Complete Error Chain for the Inner Socket Part 84
9.7. Complete Error Chain for the Inner Foil Part 84
9.8. Composition of the Standard Deviation of the Remeasured Blade 86
(a). Deviation Composition for the Outer Socket 86
(b). Deviation Composition for the Outer Foil 86
(c). Deviation Composition for the Inner Socket 86
(d). Deviation Composition for the Inner Foil 86

10.1. Test Pieces for Exemplary Reverse Engineering Process 89
10.2. Complete Error Chain for Flow Swirler 92
10.3. Workflow for the Burner Tip Replication Investigations 93
10.4. Burner Tip and Manufactured Replicas 93
10.5. Complete Error Chain for the Burner Tip 95
(a). Complete Error Chain for Burner Tip I 95
(b). Complete Error Chain for Burner Tip II 95

11.1. Comparison of Cone Beam and Fan Beam CT for a Turbine Blade 99
11.2. Views of a Test Piece with FPD and LDA 100
(a). Test Piece Captured via Flat Panel Detector (FPD) With Strong Scatter Artifacts 100
(b). Test Piece Captured via Line Detector Array (LDA) With Reduced Scatter Artifacts 100

List of Tables

2.1. Comparison of Metal-processing AM methods 33

3.1. Previous Usage of RE and AM for Custom-made Implants 36
3.2. Overview of 3D-Printers with Surface Scanning Ability 37

4.1. Used Parameters for Low Energy CT 41
4.2. Parameter Overview for all CT Scans of Blade I 42

5.1. Comparison of ROI Properties 45
5.2. Mean Values and Standard Deviation of Preivous Comparisons 54
5.3. Mean Values and Standard Deviation Values for Concave-Convex-Comparison 55

6.1. Mean Values and Standard Deviation Values for Comparisons of Optical Scan with CAD for Both Blades 61
6.2. Mean Values and Standard Deviation Values for Comparisons of DECT Scans with CAD for Both Blades 64

7.1. Mean Values and Standard Deviation Values for DECT Comparisons 68
7.2. Mean Values and Standard Deviation Values for Robustness Investigation . . . 72

8.1. Simulation Parameters for the Destructive Testing Approach. 73
8.2. Mean and Standard Deviation for Contrast Comparison 75

9.1. CT Parameters for Blade III Scan 77
9.2. Calculated Comparisons for Error Investigation of the Blade 80
9.3. Results of the Error Calculation for the Entire Replication Workflow 87

10.1. CT Parameters for Additional Test Pieces 90
10.2. Comparisons for the Error Investigation for the Flow Swirler 92
10.3. Error Propagation Overview for the Entire Flow Swirler RE and AM 92
10.4. Comparisons for the Error Investigation of the Burner Tip 94
10.5. Error Propagation Overview for the Entire Burniner Tip RE and AM 94

List of Symbols

A	Specified Nominal Value
A_{AM}	Mean Value Shift by Additive Manufacturing
A_M	Mean value Shift by Manufacturing
A_{new}	Mean Value at End of Replication Process
A_{old}	Original Mean Value
A_{RE}	Mean Value Shift by Reverse Engineering
E	Photon Energy (for Single Photon)
E_{max}	Maximal Photon Energy
E_p	Energy of a Monoenergetic Photon Ray with n Singular Photons
I	Signal Intensity, Amount of Photons
M	Magnification Factor
R_a	Average Roughness
U_a	Acceleration Voltage
Z	Atomic Number
e	Elementary Charge of an Electron
h	Planck's Constant
n	Number of Photons
p_γ	Projections under Angle γ in Radon space
u	Coordinate in Cartesian Coordinate System in Fourier space
v	Coordinate in Cartesian Coordinate System in Fourier space
ν_{max}	Maximal Frequency of Electrons in a Distribution
x	Workpiece-based Coordinate in Object Space
y	Workpiece-based Coordinate in Object Space
α	Linear Absorption Coefficient
γ	Angle Between Source-Detector and Object Coordinate Systems
δ	General Measurement Error, Dirac-Delta, Standard Deviation
δ_{AM}	Standard Deviation of Additive Manufacturing Process
δ_M	Standard Deviation of Manufacturing

δ_{RE}	Standard Deviation of Reverse Engineering Process
δ_T	Tolerance
η	Photon Pathway, Source-Detector-Based Coordinate in Object Space
η_h	Half-thickness
λ	Photon Wavelength
μ	Linear Attenuation Coefficient
μ_S	Linear Scatter Coefficient
ν	Photon Frequency
ξ	Source-detector-based Coordinate in Object Space
ρ	Density
ψ	Coordinate in Spheric Coordinate System in Fourier Space (Source Distance)
ω	Coordinate in Spheric Coordinate System in Fourier space (Angle)

List of Acronyms

3DP	3D-Printing
ABS	Acrylonitrile Butadiene Styrene
AM	Additive Manufacturing
aRTist	Analytical RT Inspection Simulation Tool
BAM	Bundesanstalt für Materialforschung und -Prüfung
CAD	Computer-aided Design
CCD	Charge-coupled Device
CMM	Coordinate Measuring Machine
CNC	Computerized Numerical Control
CNR	Contrast-to-noise Ratio
CT	Computed Tomography
DECT	Dual-Energy Computed Tomography
EBM	Electron Beam Melting
FBP	Filtered Back-Projection
FDK	Algorithm Developed by Feldkamp, Davis and Kress
FDM	Fused Deposition Modeling
FFF	Fused Filament Fabrication
FPD	Flat Panel Detector
GOS	Gadolinium Oxysulfide
LDA	Line Detector Array
Linac	Linear Accelerator
LMD	Laser Metal Deposition
NDT	Non-destructive Testing
ODD	Object-detector-distance

PEEK	Polyether Ether Ketone
PET	Positron Emission Tomography
PLA	Polylactic Acid
PMMA	Polymethylmethacrylate
RE	Reverse Engineering
ROI	Region of Interest
RP	Rapid Prototyping
SDD	Source-detector-distance
SLM	Selective Laser Melting
SNR	Signal-to-noise Ratio
SOD	Source-object-distance
STL	Stereolitography, Standard Triangulation/Tessellation Language
TFT	Thin-film Transistor

Appendix

A. Data Preparation and Correction

A.1. Correction for Systematic Errors of the Foil Section

Like mentioned in sec. 5, we had to clean our deviation measurement from local systematic errors. We encountered them since the air outlet (see fig. A.1) poses a link between inner and outer structure of the blade, while the optic scan is unable to resolve more than the first few micrometers of the inner part of the blade (the detail is depicted exemplarily for the low energy CT scan in fig. A.2). VGStudio cannot distinguish if the resolved geometry belongs to the inner or outer part of the foil and tries to compare the inner structure with a scan of the outer surface, which results in great deviations that do not reflect reality and distort our analysis. Figure A.3 shows the geometry deviations of the foil surface and its distribution. The systematic errors can be seen in the left in form of a second peak at ca. 0.68 mm. In order to adjust these data, we choose an interval of $\pm 110\,\mu m$ (corresponds to points between -0.57 mm and -0.79 mm) and set all values within to 0 %, which is way closer to reality than the uncorrected numbers. We performed this correction for both, the 225 keV-scan and the 450 keV-scan.

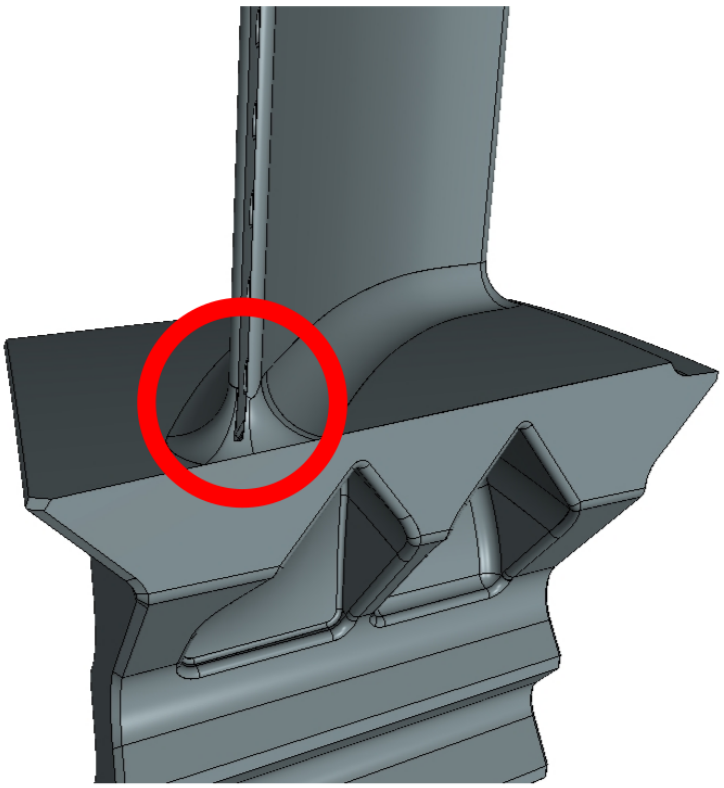

Figure A.1.: The air outlet of the blade introduced systematic errors into our measurement, since the air outlet is part of the inner structure as well. The detail indicated by the red circle is illustrated in fig. A.2.

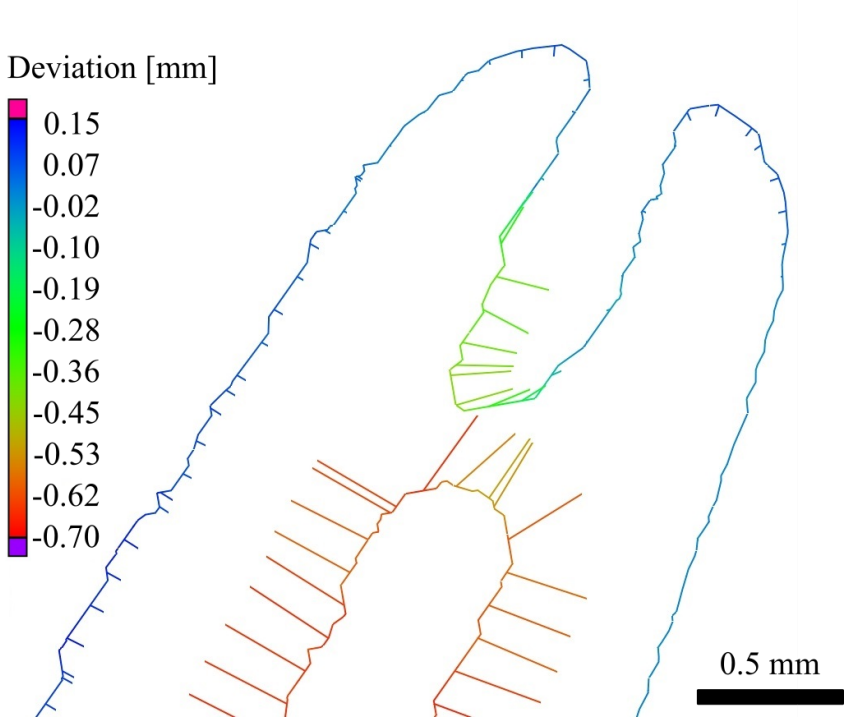

Figure A.2.: Detail view of the air outlet at the position of interest (see red circle in A.1). Colored lines indicate calculated deviations of low energy CT to the optic scan. We can see clearly that the algorithm tries to compare the inner structure with the outer surface of the foil, which results in an incorrect measurement and as second peak in the distribution shown in fig. A.3.

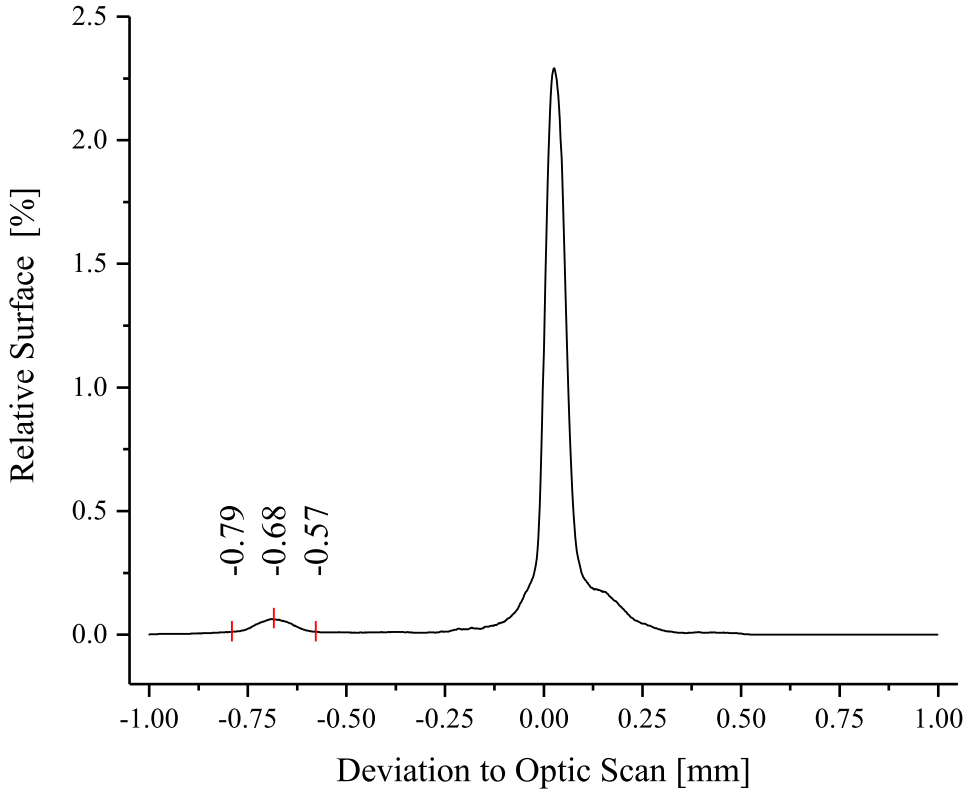

Figure A.3.: Measured error distribution of the low energy CT compared to the optic scan for the complete foil surface. We set deviations within the interval from −0.57 mm to −0.79 mm to 0 % to correct for these systematic errors. This scan is represented as the second boxplot in figure 5.7 in the main text.

A.2. Correction for Support Structure and Filling in FDM Test Pieces

Within this section we want to describe the error correction protocol for the test pieces produced via FDM in sec. 10.1. Exemplarily depicted is the comparison of the reverse-engineered mesh of the original swirler piece with the initially designed CAD geometry (i.e. comparison C_{20}) in fig. A.4. Due to computational limitations, only the greatest 87 % of the distribution are shown (i.e. distribution continues in negative direction). We assume that the second, spread-out peak, located at ca. −0.8 mm is caused by the support structure and filling of the printed compared to the original CAD model. In the CAD, all walls are made from massive material, which is replaced by a less densely filled wall structure and results in strong deviations from the CAD up to several mm. This is also directly visible if we take a look at the geometrical location of the errors like shown in fig. A.5. We correct these distributions (e.g. distributions C_{10} and C_{20}) by removing all values located left from the assumed end of the primary peak (−0.5 mm in this case). As a matter of fact, the error continues through the whole chain. But since the re-print via AM introduces a similar support structure and filling on its own that we use for comparison and usually less than 100 % of all distribution values are considered, we assume this error to be sufficiently small. The percentage of remaining values for comparison compared to all distortions of the piece (i.e. "broadness" of the considered distribution to "broadness" of entire distribution) is given as percentage value, like e.g. in tab. 10.2.

Nevertheless, this error is not ignorable for the final comparison of remeasured geometry with the original design, i.e. comparisons C_{30} and C_{40}. The distribution is depicted in fig. A.6 and we can see clearly that the separation of both overlaying graphs is not that easily possible anymore. The sharp peak at ca. −0.8 mm originates from a flawed registration approach at the upper part of the object. We assumed that both error graphs are approximately Gaussian-shaped, since – according to the Central Limit Theorem – the sum of a high number of independent variables converges towards a Gaussian; this behavior is valid even if the underlying distribution functions do not follow such a distribution [Buzug 2008, p. 71f]. Consequently, we performed a Gauss-fit on all values in the interval from −0.3 mm to 2 mm. The fitted graph is depicted in fig. A.6, the residuals are shown in fig. A.7. The equation of the fit follows the equation

$$y(x) = y_0 + \frac{A}{\omega \cdot \sqrt{\frac{\pi}{2}}} \cdot \exp\left(-2 \cdot \left(\frac{x - x_c}{\omega}\right)^2\right)$$

with $y_0 = 0.00715$, $x_c = 0.116{,}85\,\text{mm}$, $\omega = 0.844{,}11\,\text{mm}$ and $A = 0.217{,}18\,\text{mm}$. For comparison C_{30} these values are given by $y_0 = 0.00752$, $x_c = 0.132{,}64\,\text{mm}$, $\omega = 0.816{,}77\,\text{mm}$ and $A = 0.212{,}96\,\text{mm}$. We do not show the fitted curve and the difference graph here, since the distribution is almost identical to comparison C_{40} and grants no new insight. We assume that only the newly generated fit is sufficient for our comparison and determine the mean value and standard deviation of it for documentation. The given percentage value refers to the amount of

values that were used for the fit in comparison to the entire distribution. Percentages values are marked with a "*" in order to stress the different way of error correction.

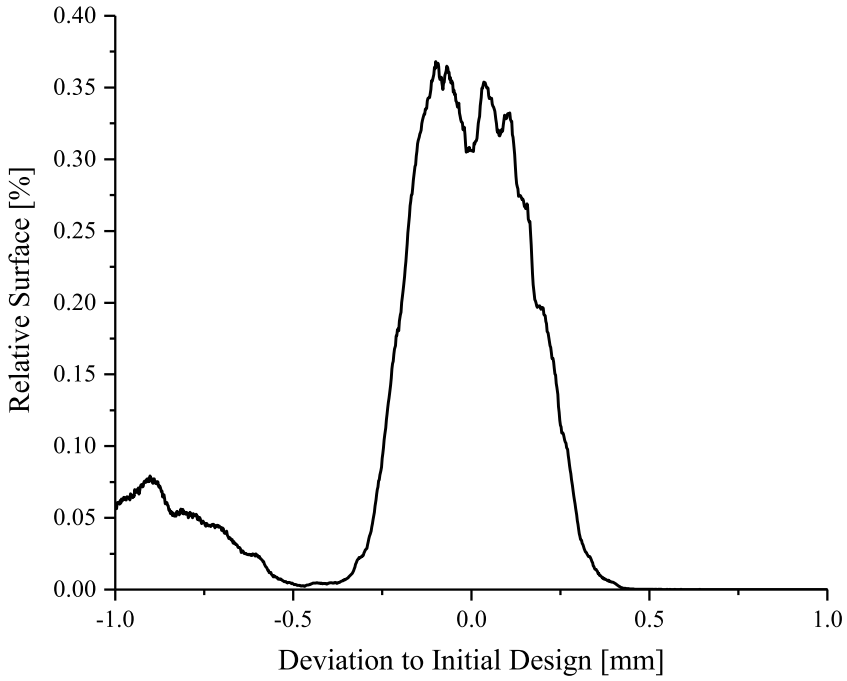

Figure A.4.: Deviation of the reverse engineered mesh of the original swirler workpiece to the initial design. This comparison is also termed comparison C_{20}. Mind also that the maximum values of the ordinate are way smaller than the ones given in e.g. fig. A.3. This is caused by the significantly broadened distribution.

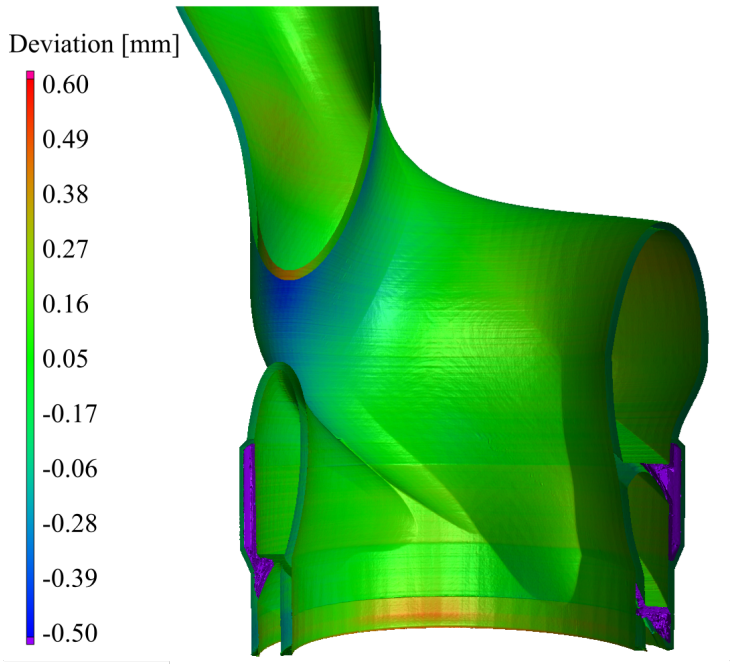

Figure A.5.: Half-cutted view of the final test piece and location of its filling structures. The deviations smaller than −0.5 mm in fig. A.6 are primarily caused by the support structure and filling. We can see clearly that the missing material in the walls (indicated in purple) is responsible for the second, spread out peak in the deviation graph.

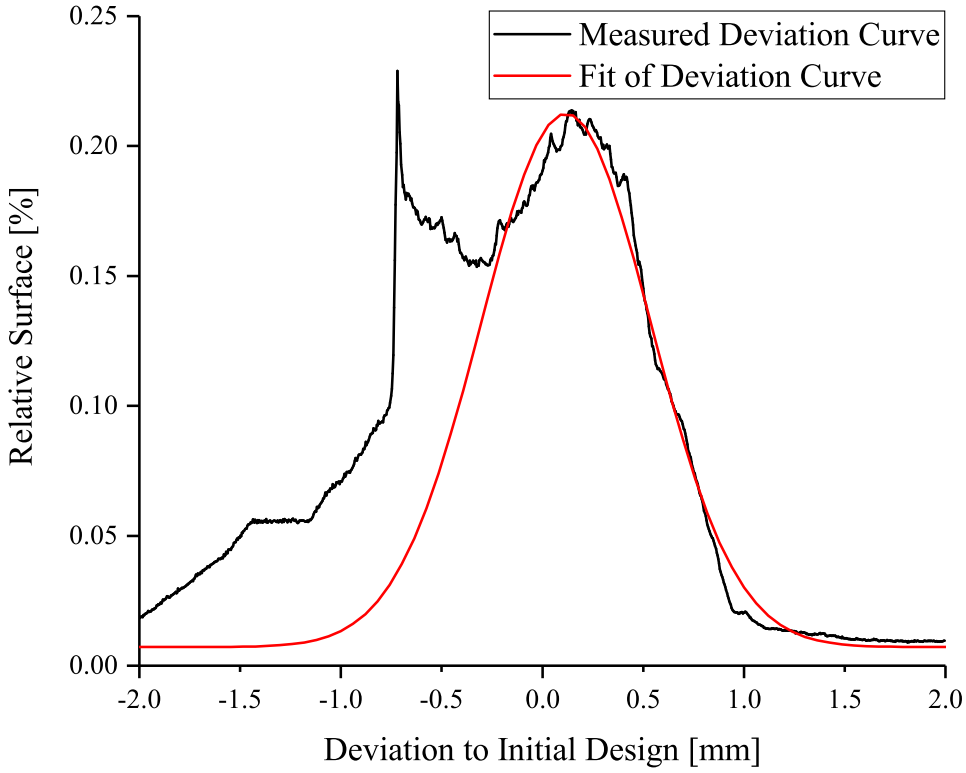

Figure A.6.: Comparison of remeasured mesh with inital CAD design (i.e. comparison C_{40}) and applied Gauss-fit in order to remove deviations caused by filling and support structure.

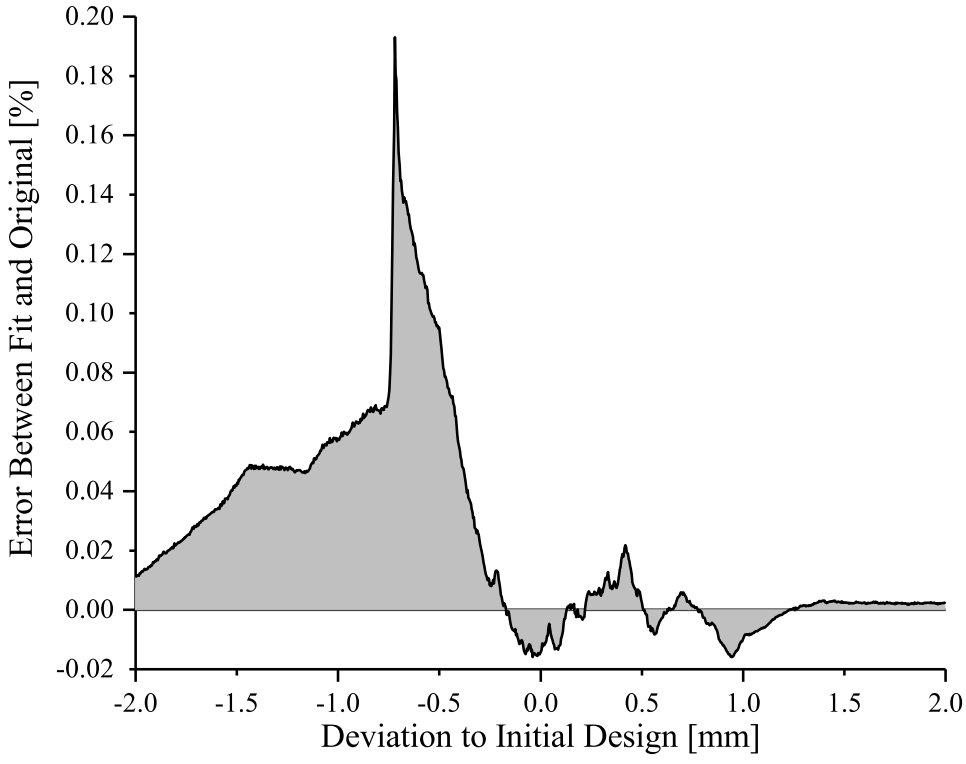

Figure A.7.: Difference between the measured deviation curve of fig. A.6 and the respective fit.

B. Material Information for EOS NickelAlloy HX

B.1. Material Attenuation Coefficients for EOS NickelAlloy HX

We simulated the attenuation coefficients by use of the software tool aRTist. Material composition was set to 48 % Nickel, 21 % Chromium, 17 % Iron, 8 % Molybdenum, 1.5 % Titan, 1 % Tungsten, 1 % Cobalt, 1 % Silicon, 1 % Manganese, 0.5 % Copper, 0.5 % Aluminum and the density to $\rho = 8.2\,\mathrm{g\,cm^{-3}}$. Results are provided in fig. B.1.

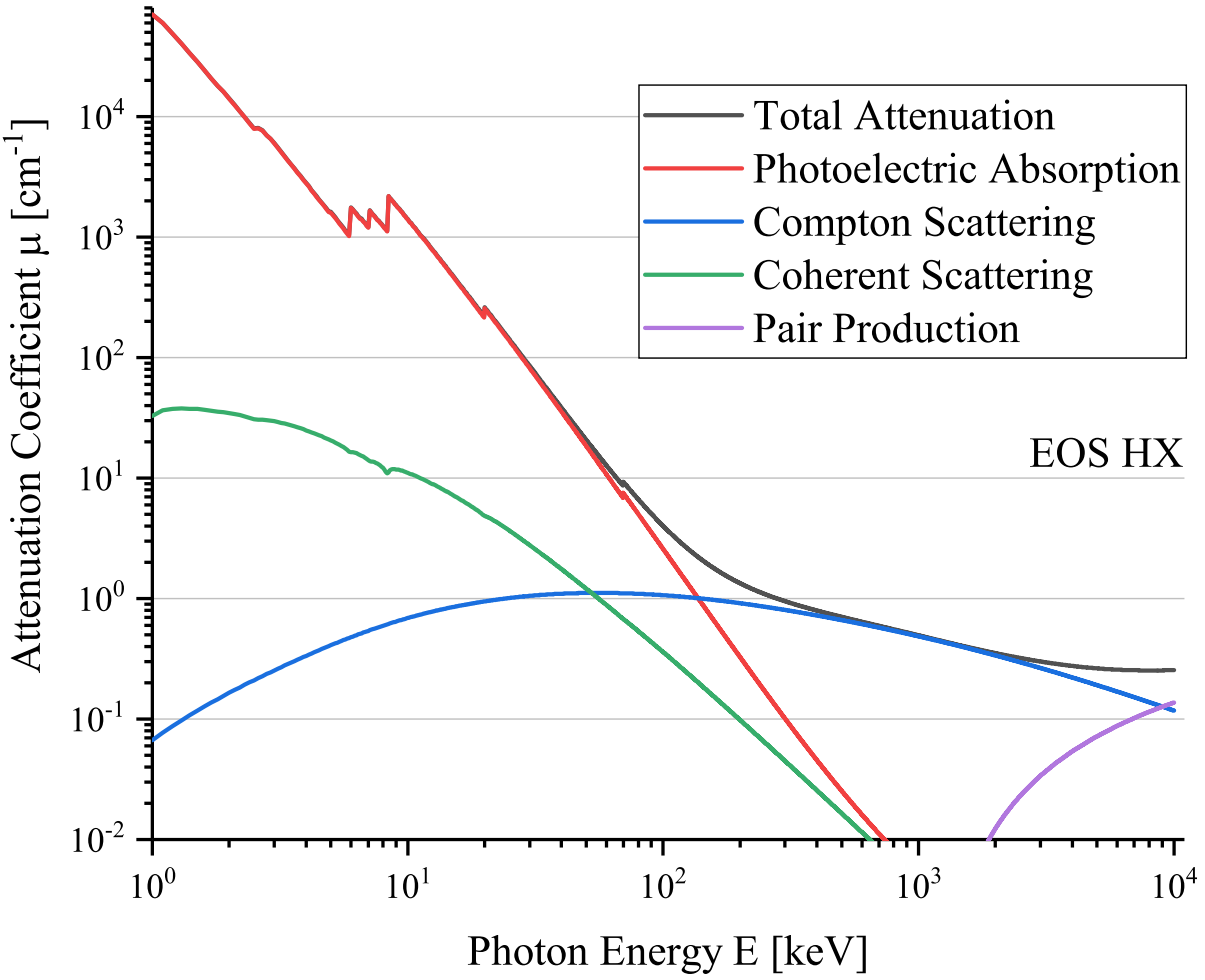

Figure B.1.: Approximated attenuation coefficients and their composition for the turbine material EOS HX. Data were computed and not derived experimentally.

B.2. Material Data Sheet for EOS NickelAlloy HX

Material data sheet

EOS NickelAlloy HX

EOS NickelAlloy HX is a heat and corrosion resistant metal alloy powder intended for processing on EOS M 290 systems.

This document provides information and data for parts built using EOS NickelAlloy HX powder (EOS art.-no. 9011-0023) on the following system specifications:

- EOS M 290 400W with EOSPRINT 1.x and EOS Parameter set HX_Performance 2.0

Description, application

EOS NickelAlloy HX raw material is a nickel-chromium-iron-molybdenum alloy in fine powder form. Its composition corresponds to UNS N06002. While the wrought and cast versions of the alloy generally are solution annealed, the laser melted material manufactured of this powder has a high strength and good elongation already in the as-built condition. Solution annealing of the laser sintered material will homogenize the microstructure, relax internal stresses and increase the elongation, while slightly decreasing the strength.

This type of alloy is characterized by having high strength and oxidation resistance also at elevated temperatures, and is often used up to 1200°C. Therefore its applications can be found in aerospace technology, gas turbine parts, etc.

Standard laser processing parameters results in full melting of the entire geometry, typically with 40 µm layer thickness. Parts built from EOS NickelAlloy HX can be heat treated and material properties can be varied within specified range. In both as-built and solution heat treated states the parts can be machined, spark-eroded, welded, micro shot-peened, polished, and coated if required. Unexposed powder can be reused.

EOS GmbH - Electro Optical Systems
Robert-Stirling-Ring 1
D-82152 Krailling / München
Telephone: +49 (0)89 / 893 36-0
Telefax: +49 (0)89 / 893 36-285
Internet: www.eos.info

EOS - Material data sheet

Technical data

General process data

	EOS NickelAlloy HX
Typical achievable part accuracy [1]	
- small parts	approx. ±50-80 µm (± 0.0020 – 0.0031 inch)
- large parts	approx. ± 0.2 %
Min. wall thickness [2]	typ. 0.4 - 0.5 mm (0.016 – 0.020 inch)
Layer thickness	40 µm
Surface roughness [3]	
- after shot-peening (horizontal / vertical)	R_a 3 – 6.5 µm, R_z 10 - 30 µm R_a 0.12 – 0.25 x 10^{-3} inch, R_z 0.39 – 1.18 x 10^{-3} inch
- after polishing	R_z up to < 0.5 µm R_z up to < 0.02 x 10^{-3} inch (can be very finely polished)
Volume rate [4]	4.2 mm³/s (15.2 cm³/h) 0.93 in³/h

[1] Based on users' experience of dimensional accuracy for typical geometries, e.g. ± 50 µm when parameters can be optimized for a certain class of parts or ± 80 µm when building a new kind of geometry for the first time. Part accuracy is subject to appropriate data preparation and postprocessing.

[2] Mechanical stability is dependent on geometry (wall height etc.) and application

[3] Due to the layerwise building, the surface structure depends strongly on the orientation of the surface, for example sloping and curved surfaces exhibit a stair-step effect. The values also depend on the measurement method used. The values quoted here given an indication of what can be expected for horizontal (up-facing) or vertical surfaces.

[4] Volume rate is a measure of build speed during laser exposure. The total build speed depends on the average volume rate, the recoating time (related to the number of layers) and other factors such as DMLS-Start settings.

EOS GmbH - Electro Optical Systems
Robert-Stirling-Ring 1
D-82152 Krailling / München

EOS - Material data sheet

Physical and chemical properties of parts

	EOS NickelAlloy HX		
Material composition	Element	Min	Max
	Ni	balance	
	Cr	20.5	23.0
	Fe	17.0	20.0
	Mo	8.0	10.0
	W	0.2	1.0
	Co	0.5	2.5
	C	--	0.1
	Si	--	1.0
	Mn	--	1.0
	S	--	0.03
	P	--	0.04
	B	--	0.01
	Se	--	0.0050
	Cu	--	0.5
	Al	--	0.5
	Ti	--	0.15
Relative density with standard parameters	approx. 100 %		
Density with standard parameters	min. 8.2 g/cm3 min. 0.296 lb/in³		

EOS GmbH - Electro Optical Systems
Robert-Stirling-Ring 1
D-82152 Krailling / München

EOS - Material data sheet

Mechanical properties of parts (at room temperature)

	As built
Ultimate tensile strength [5]	
- in horizontal direction (XY)	typ. 820 ± 50 MPa
- in vertical direction (Z)	typ. 675 ±50 MPa
Yield strength, Rp0.2% [5]	
- in horizontal direction (XY)	typ. 630 ±50 MPa
- in vertical direction (Z)	typ. 545 ±50 MPa
Young's modulus [5]	
- in horizontal direction (XY)	typ. 195 ±20 GPa
- in vertical direction (Z)	typ. 175±20 GPa
Elongation at break [5]	
- in horizontal direction (XY)	typ. 27 ±8 %
- in vertical direction (Z)	typ. 39 ±8 %

[5] Tensile testing according to ISO 6892-1:2009 (B) Annex D, proportional test pieces, diameter of the neck area 5 mm (0.2 inch), original gauge length 25 mm (1 inch).

Abbreviations

typ.	typical
min.	minimum
approx.	approximately
wt	weight

EOS GmbH - Electro Optical Systems
Robert-Stirling-Ring 1
D-82152 Krailling / München

EOS - Material data sheet

The quoted values refer to the use of these materials with EOS M 290 systems according to current specifications (including the latest released process software PSW and any hardware specified for the relevant material) and operating instructions. All values are approximate. Unless otherwise stated, the quoted mechanical and physical properties refer to standard building parameters and test samples built in vertical orientation. They depend on the building parameters and strategies used, which can be varied by the user according to the application.
The data are based on our latest knowledge and are subject to changes without notice. They are provided as an indication and not as a guarantee of suitability for any specific application.

EOS GmbH - Electro Optical Systems
Robert-Stirling-Ring 1
D-82152 Krailling / München

C. Calibration Protocol for Optic Scanner ATOS III Triple Scan

GOM mbH
Mittelweg 7-8
38106 Braunschweig
Germany

gom Gesellschaft für Optische Messtechnik

GOM Acceptance Test	120511_CP40-320-50507
	Certificate No.

Annahme/Überwachung in Anlehnung an VDI/VDE 2634, Blatt 3

Allgemeine Daten

System:	ATOS III Rev.02 400 MV320 SN:120231
Messvolumen:	MV320 (320x240x240) mm
Datum:	11.05.16
Prüfer:	J.Kristen
Messtemperatur:	25.4 °C

Prüfkörper

Allgemeines

Name:	PSA/400/Z0005_L7R7
Kalibrierdatum:	17.11.15
Kalibrierzeichen:	0084-D-K-15007-02-00-2011-11
Kalibriertemperatur:	20.0 °C
Ausdehnungskoeffizient für Kugelabstand:	4.00 10^{-6} K^{-1}
Ausdehnungskoeffizient für Durchmesser:	10.50 10^{-6} K^{-1}

Nennmaße

Kugelabstand:	160 mm
Durchmesser linke Kugel:	25 mm
Durchmesser rechte Kugel:	25 mm

Kalibrierte Soll-Maße

Kugelabstand:	159.9764 mm
Durchmesser linke Kugel:	25.0021 mm
Durchmesser rechte Kugel:	25.0029 mm

Certificate No. 120511_CP40-320-50507

Messparameter

Messeinstellungen

Anzahl der Belichtungszeiten:	1
Min. Streifenkontrast:	15 Grauwerte
Status: Punkte bei starken Helligkeitsunterschieden vermeiden?:	Ja
Status: Triple-Scan-Punkte vermeiden?:	Nein
Status: Triple-Scan-Punkte bei starken Helligkeitsunterschieden vermeiden?:	Ja
Max. Residuum:	0.20 Pixel
Tiefenbegrenzungsmodus:	Automatische Tiefenbegrenzung
Eckenmaskierungsgröße:	0
Messauflösung:	Volle Auflösung

Kontrolleinstellungen

Status: Kontrolle "Sensorbewegung"?:	Ein
Max. Sensorbewegung:	0.10 Pixel
Status: Kontrolle "Lichtänderung"?:	Ein

Sensorkalibrierung

Allgemeines

Kalibrierdatum:	Fri May 11 13:30:29 2016
Messtemperatur:	25.6 °C

Kalibrierobjekt

Kalibrierobjekttyp:	Platte (Triple Scan)
Name des Kalibrierobjekts:	CP40-320-50507
Prüfstrecken:	574.298 / 574.319 mm
Zertifizierungstemperatur:	20.0 °C
Ausdehnungskoeffizient:	22.67 10^{-6} K^{-1}

Kalibriereinstellungen

Brennweite (Kamera):	40.000 mm
Brennweite (Projektor):	50.000 mm
Lichtintensität:	100%
Aufnahmemodus:	Mehrfachaufnahme
Max. Ellipsenqualität:	0.40 Pixel

Kalibrierergebnis

Kalibrierabweichung:	0.027 Pixel (Qualitätsprüfung: Gut)
Kalibrierabweichung (optimiert):	0.012 Pixel
Projektorkalibrierabweichung:	0.118 Pixel (Qualitätsprüfung: Gut)
Projektorkalibrierabweichung (optimiert):	0.016 Pixel
Kamerawinkel:	27.13 deg
Höhenänderung:	243.867 mm
Messvolumen:	332 x 252 x 245 mm

Certificate No. 120511_CP40-320-50507

Annahme/Überwachungstest

Allgemeines

Anzahl Prüfpositionen (Messreihen): 3
Soll-Durchmesser linke Kugel mit Temperaturkorrektur: 25.0035 mm
Soll-Durchmesser rechte Kugel mit Temperaturkorrektur: 25.0043 mm
Soll-Kugelabstand mit Temperaturkorrektur: 159.9799 mm

Kenngröße Antastabweichung Form, linke Kugel

Pos[2]	M[3]	P[4]	Min. Abweichung	Max. Abweichung	Spanne der Abweichung	Antastabweichung Form (Sigma)
1	10	16454	-0.005 mm	0.005 mm	0.010 mm	0.002 mm
2	10	19021	-0.004 mm	0.004 mm	0.008 mm	0.001 mm
3	10	18940	-0.004 mm	0.005 mm	0.009 mm	0.001 mm

Kenngröße Antastabweichung Form, rechte Kugel

Pos[2]	M[3]	P[4]	Min. Abweichung	Max. Abweichung	Spanne der Abweichung	Antastabweichung Form (Sigma)
1	10	16595	-0.005 mm	0.005 mm	0.010 mm	0.002 mm
2	10	18699	-0.004 mm	0.004 mm	0.008 mm	0.001 mm
3	10	18761	-0.004 mm	0.004 mm	0.009 mm	0.001 mm

Kenngröße Antastabweichung Maß, linke Kugel

Pos[2]	M[3]	P[4]	Durchmesser (Ist)	Durchmesser (Soll)[1]	Antastabweichung (Maß)
1	10	16454	25.007 mm	25.004 mm	0.004 mm
2	10	19021	25.006 mm	25.004 mm	0.002 mm
3	10	18940	25.004 mm	25.004 mm	0.000 mm

Kenngröße Antastabweichung Maß, rechte Kugel

Pos[2]	M[3]	P[4]	Durchmesser (Ist)	Durchmesser (Soll)[1]	Antastabweichung (Maß)
1	10	16595	25.007 mm	25.004 mm	0.003 mm
2	10	18699	25.006 mm	25.004 mm	0.002 mm
3	10	18761	25.005 mm	25.004 mm	0.001 mm

Kenngröße Kugelabstandsabweichung

Pos[2]	M[3]	Kugelabstand (Ist)	Kugelabstand (Soll)[1]	Kugelabstandsabweichung
1	10	159.984 mm	159.980 mm	0.004 mm
2	10	159.981 mm	159.980 mm	0.001 mm
3	10	159.983 mm	159.980 mm	0.003 mm

GOM mbH 3./5 11.05.16 14:10

Certificate No. 120511_CP40-320-50507

Kenngröße Längenmessabweichung

Pos[2)]	M[3)]	Länge (Ist)	Länge (Soll)[1)]	Längenmessabweichung
1	10	184.988 mm	184.984 mm	0.004 mm
2	10	184.985 mm	184.984 mm	0.001 mm
3	10	184.985 mm	184.984 mm	0.001 mm

[1)] Mit Temperaturkorrektur
[2)] Prüfposition
[3)] Anzahl Messungen
[4)] Anzahl der Punkte

GOM mbH 4./5 11.05.16 14:10

Certificate No. 120511_CP40-320-50507

Zusammenfassung Annahme/Überwachungstest

Kenngröße	Maximale Abweichung	Grenzwert
Antastabweichung Form (Sigma)	0.002 mm	0.005 mm
Kugelabstandsabweichung	0.004 mm	0.016 mm

Einschränkungen der Betriebsart und Betriebsbedingungen

Betriebsart

- Der Sensor sowie dessen Bestandteile sind von Werk eingestellt und dürfen nicht verändert werden. Dies betrifft insbesondere die Kameras und die Objektive.
- Der Sensor muss gemäß der Hardware-Bedienungsanleitung kalibriert sein. Vordringlich sind die Aufwärmzeiten und die Grenzwerte der Kalibrierung einzuhalten.
- Die Messungen erfolgen mit der Qualitätseinstellung "Hoch".
- Die Dauer der Bildaufnahme muss so gewählt sein, dass die Messbilder gut ausgeleuchtet sind. Überbelichtungen dürfen nicht auftreten.
- Die zu einem Netz zusammengefügten Einzelmessungen werden mit der Polygonisierungseinstellung "Standard" nachverarbeitet.
- Die Bestimmung der Kugeln erfolgt nach der Methode der kleinsten Quadrate, wobei 0,3% der Messwerte als Ausreißer verworfen werden. Dieser Wert entspricht einer Einstellung von 3 Sigma.
  Für die Bestimmung der Kugeln werden nur Messdaten verwendet, die oberhalb einer definierten Ebene liegen. Diese Ebene ist parallel zur Prüfkörper-Trägerplatte und verläuft durch den Kleinkreis mit 10° südlicher Breite.
- Die Bestimmung der Kenngröße "Längenmessabweichung" erfolgt gemäß Verfahren C (siehe VDI/VDE 2634 Blatt 3 S. 18).

Betriebsbedingungen

- Der Prüfkörper umfasst zwei über eine Trägerplatte starr miteinander verbundene Kugeln mit den im Abschnitt "Prüfkörper" definierten Nenndurchmessern.
- Der Abstand der Kugeln entspricht genähert dem im Abschnitt "Prüfkörper" definierten Nennabstand.
- Die Kugeln bestehen aus Stahl und sind mit einer Titandioxidschicht überzogen, um ein diffuses Reflexionsverhalten sicherzustellen.
- Die Kugeldurchmesser und der Kugelabstand müssen durch eine DAkkS-Kalibrierung bestimmt werden, wobei die zugehörige Messunsicherheit im Vergleich zum zugehörigen Grenzwert klein sein muss.
- Die Umgebungsbedingungen gemäß der Hardware-Bedienungsanleitung müssen eingehalten werden. Insbesondere muss die Temperatur über den gesamten Messzeitraum konstant sein.
- Die Umgebungstemperatur und die Temperatur des Prüfkörpers müssen identisch sein.
- Die Messumgebung muss frei von mechanischen Schwingungseinflüssen sein.
- Das Umgebungslicht darf während der Messung nicht zu stark variieren.
- Strahlungsintensive Fremdlichtquellen sind zu vermeiden.

D. VGStudio Workflows and Macros

D.1. Segmentation and Mesh Generation from Raw Data

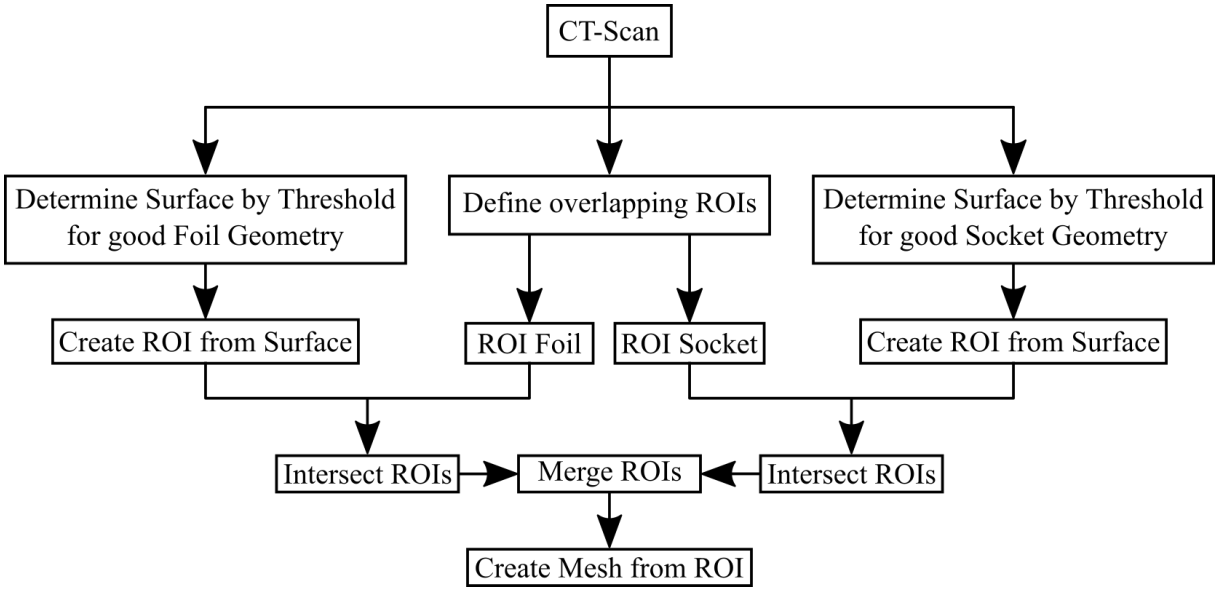

Figure D.1.: Flowchart for segmentation and mesh creation of CT raw data. Exemplarily shown are the two ROIs used for all final meshes. For the low energy scan the socket part was further subdivided as explained in section 5.2.

D.2. Segmentation and Mesh Generation via Dual Energy Approach

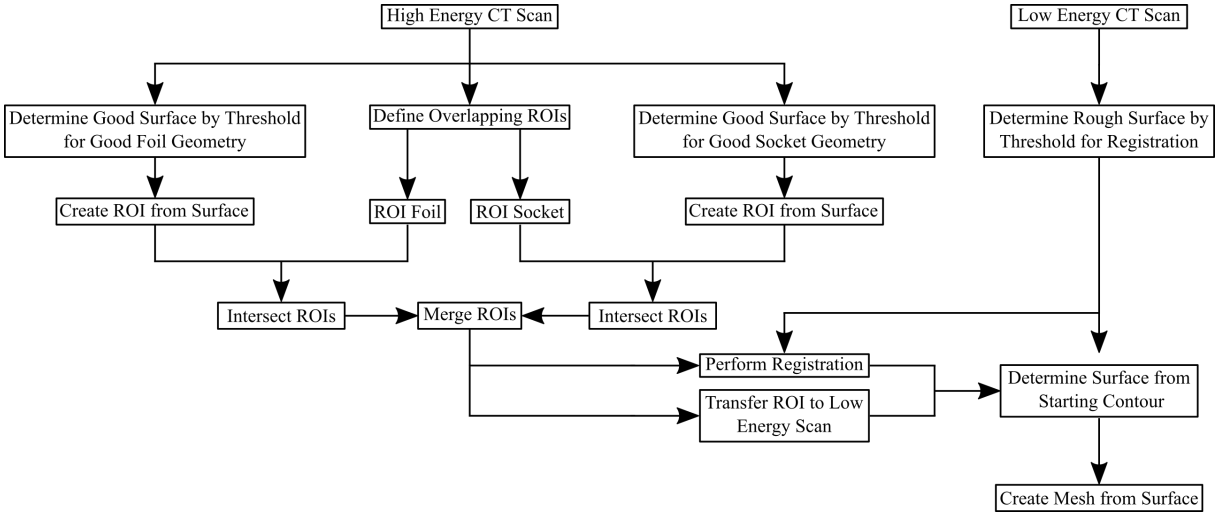

Figure D.2.: Flowchart for segmentation and mesh creation via DECT approach. A more detailled explanation can be found in sec. 7.2.